DEVELOPMENT OF VISCOELASTIC PARTICLE MIGRATION FOR MICROFLUIDIC FLOW CYTOMETRY APPLICATIONS

A DISSERTATION SUBMITTED TO
THE GRADUATE SCHOOL OF ENGINEERING AND SCIENCE
OF BILKENT UNIVERSITY
IN PARTIAL FULFILLMENT OF THE REQUIREMENTS FOR
THE DEGREE OF
DOCTOR OF PHILOSOPHY
IN
MATERIALS SCIENCE AND NANOTECHNOLOGY

By
Murat Serhatlıoğlu
April 2020

DEVELOPMENT OF VISCOELASTIC PARTICLE MIGRATION FOR MICROFLUIDIC FLOW CYTOMETRY APPLICATIONS

By Murat Serhatlıoğlu

April 2020

We certify that we have read this dissertation and that in our opinion it is fully adequate, in scope and in quality, as a dissertation for the degree of Doctor of Philosophy.

Çağlar Elbüken(Advisor)

Bülend Ortaç

Haluk Külah

Lokman Uzun

Aykut Erbaş

Approved for the Graduate School of Engineering and Science:

Ezhan Karaşan
Director of the Graduate School

ABSTRACT

DEVELOPMENT OF VISCOELASTIC PARTICLE MIGRATION FOR MICROFLUIDIC FLOW CYTOMETRY APPLICATIONS

Murat Serhatlıoğlu
Ph.D. in Materials Science and Nanotechnology
Advisor: Çağlar Elbüken
April 2020

Advances in cell biology, quantification, and identification procedures are essential to develop novel particle characterization tools on the diagnostics, biotechnology, pharmaceutical industry, and material science. Flow cytometry is a pivotal technology and meets the need for almost a century. Increase in today's demand for fast, precise, accurate, and low-cost point-of-care diagnostic tools and cell counting technologies necessitate further improvements for state-of-the-art flow cytometry platforms. These improvements are achievable using novel and precise particle focusing techniques, multiple detection methods, integrated fluidic, optical, and electronic units in the same workflow. Thanks to its indisputable advantages in such integrities, microfluidic flow cytometry platforms are attractive and promising tool for the future of next-generation flow cytometry technologies.

In this thesis, we developed viscoelastic focusing technique compatible with optical, impedimetric, and imaging-based microfluidic flow cytometry methods. Elastic nature of the viscoelastic fluids induces lateral migration for suspended particles into a single streamline and meets the requirement for central particle focusing on flow cytometry devices. Viscoelastic focusing is a passive particle manipulation technique and eliminates the need for sheath flow or any other active actuation mechanism. Firstly, we developed viscoelastic focusing technique for optical microfluidic flow cytometry in a palm-sized glass capillary device. Optical detection was performed by fiber-coupled laser source and photodetectors. We demonstrated the detection of polystyrene (PS) cytometry calibration beads suspended in three viscoelastic solutions: Polyethylene oxide (PEO), Hyaluronic acid (HA), and Polyvinylpyrrolidone (PVP). Secondly, we investigated the viscoelastic focusing efficiency of PEO-based viscoelastic solutions at varying ionic concentrations to demonstrate their use in impedance-based microfluidic flow cytometry. We performed cytometry measurements using PS beads and human red blood cells (RBCs). We showed that elasto-inertial focusing of PS beads is possible

with the combination of inertial and viscoelastic effects for high-throughput flow cytometry applications. Additionally, non-spherical shape RBCs were aligned along the channel centerline in parachute shape, which yielded to decrease the non-spherical shape-based signal variations in impedance cytometry devices consistent impedimetric signals. Our results showed that proposed flow cytometry devices give similar performance to state-of-the-art systems in terms of throughput and measurement accuracy.

Optical- and impedance-based flow cytometry applications were demonstrated using only pressure-driven flow. Under the simultaneous use of pressure-driven flow and DC electric field, particles inside microfluidic channels exhibit intricate migration behavior at different particle equilibrium positions. Available experimental and analytical studies fall short in giving a thorough explanation to particle equilibrium states. Also, the understanding is so far limited to the results based on Newtonian and neutral viscoelastic fluids.Thirdly in this thesis study, a holistic approach is taken to elaborate the interplay of governing electrophoretic and slip-induced/elastic/shear gradient lift forces. Experimental studies were carried on particle migration in Newtonian, neutral viscoelastic, and polyelectrolyte viscoelastic media to provide a comprehensive understanding of particle migration. Our experiments with the viscoelastic media led to contradictory results with the existing explanations. Then, we introduced the Electro-Viscoelastic Migration (EVM) theory to provide a unifying explanation for particle migration in Newtonian and viscoelastic solutions. Additionally, we performed confocal imaging experiments with fluorescent-labeled polymer solutions to explore the underlying migration behavior in the EVM technique. We observed the formation of cross-sectionally non-uniform viscoelastic solution would pave the way for undiscovered unique applications in the microfluidic community.

In summary, presented devices were demonstrated with straightforward fabrication techniques on a single straight microcapillary or microchannel. It is possible to couple fluidics, optical, and impedimetric detection units into the same workflow. Our approach in microfluidic flow cytometry applications proved that viscoelastic fluids are good candidates for the development of integrated, portable, and cost-efficient next-generation cytometry platforms and low resource settings. Additionally, the unifying EVM technique has a strong potential to precisely focusing and separating cells, polyelectrolytes, DNA fractions, and proteins according to their charge and size with a comparable resolution and measurement time as a replacement for gel electrophoresis or chromatography applications.

Keywords: Microfluidics, Flow cytometry, viscoelastic fluids, particle focusing.

ÖZET

MİKROAKIŞKAN AKIŞ SİTOMETRİSİ UYGULAMARINDA VİSKOELASTİK PARÇACIK HİZALAMA TEKNİĞİNİN GELİŞTİRİLMESİ

Murat Serhatlıoğlu
Malzeme Bilimi ve Nanoteknoloji Programı, Doktora
Tez Danışmanı: Dr. Öğr. Üyesi Çağlar Elbüken
Nisan 2020

Hücre biyolojisi, hücre sayımı ve hücre tespiti gibi alanlarda meydana gelen gelişmeler; hastalık teşhisi, biyoteknoloji, ilaç endüstrisi ve malzeme biliminde kullanılacak yeni parçacık karakterizasyon yöntem ve araçlarının geliştirilmesini gerekli kılmaktadır. Akış sitometri teknolojisi bu alandaki ihtiyacı neredeyse bir asırdır karşılayan öncü teknolojidir. Günümüzde hızlı, hassas, doğru ve düşük maliyetli hasta-başı teşhis cihazlarına ve hücre sayma teknolojilerine olan yoğun bir talep artışı söz konusudur. En gelişmiş ticari akış sitometri cihazları dahi teknolojik açıdan bu talebe cevap vermekte yetersiz kalabilmektedir. Bu talep, yenilikçi ve hassas parçacık hizalama teknikleri, çoklu algılama yöntemleri ve birbirine entegre akışkan, optik ve elektronik üniteler kullanılarak geliştirilen yenilikçi sitometri teknolojileri ile karşılanabilir. Bu tip özellikler konusunda tartışmasız derecede avantajlara sahip olan mikroakışkan akış sitometri platformları, yeni nesil akış sitometri teknolojilerinin geleceği adına ilgi çekici ve umut vericidir.

Bu tez çalışmasında, optik, empedans ve görüntü tabanlı mikroakışkan sitometri ölçüm yöntemleriyle uyumlu olan viskoelastik parçacık hizalama tekniği geliştirildi. Viskoelastik akışkanların elastik doğası, süspansiyon haldeki parçacıkların kanal akış eksenine dik düzlemde pozisyon değiştirerek, tek bir akış çizgisi boyunca hizalanmasını sağlar. Bu sayede akış sitometri cihazlarındaki ölçüm hassasiyetini artırmak için gerekli olan merkezi parçacık hizalanma sağlanmış olur. Viskoelastik parçacık hizalama tekniği pasif bir yöntemdir ve kılıf akışına veya herhangi bir aktif parçacık hizalama mekanizmasına olan ihtiyacı ortadan kaldırır. İlk olarak, avuç içi büyüklüğünde bir cam mikrokılcal cihazda optik mikroakışkan akış sitometrisi için viskoelastik odaklama tekniği geliştirildi. Optik ölçüm ve algılama işlemleri fiber kuplajlı lazer kaynağı ve fotodedektör yardımıyla yapıldı. Polietilen oksit (PEO), Hyalüronik asit (HA) ve Polivinilpirolidon (PVP) tabanlı üç farklı viskoelastik solüsyonda süspansiyon halindeki polistren sitometri

kalibrasyon parçacıklarının tespiti gösterildi. İkinci olarak, empedans tabanlı mikroakışkan akış sitometrilerinde kullanımlarını göstermek için PEO tabanlı viskoelastik solüsyonların farklı iyonik konsantrasyonlardaki viskoelastik parçacık hizalama etkinliği araştırıldı. Ardından, polistren ve kırmızı kan hücreleri kullanarak empedans sitometri ölçümleri gerçekleştirildi. Yüksek verimli akış sitometri uygulamaları için ataletsel ve viskoelastik etkilerin kombinasyonu kullanılarak küresel polistren parçacıklarının yüksek akış hızlarında merkezi hizalanmasının mümkün olduğu gösterildi. Buna ek olarak küresel olmayan kırmızı kan hücrelerinin tamamının kanal merkez çizgisi boyunca paraşüt şeklinde hizalanması ve bu sayede empedans sitometri cihazlarında gözlenen küresel olmayan parçacık kaynaklı ölçüm varyasyonlarının azaltılarak tutarlı empedans sinyalleri elde edilmesi sağlandı. Elde edilen sonuçlar, önerilen akış sitometri cihazlarının, verimlilik ve ölçüm hassasiyeti açısından en gelişmiş sitometri cihazlarıyla kıyaslanabilir performans değerleri elde ettiğini gösterdi.

Optik ve empedans tabanlı akış sitometri uygulamaları, yalnızca basınçlı hidrodinamik akış kullanılarak geliştirildi. Basınçlı hidrodinamik akış ve elektrik alan kaynaklı elektroforez eşzamanlı olarak uygulandığında, mikroakışkan kanalların içindeki süspanse parçacıklar karmaşık hizalanma davranışları ve birbirinden farklı nihai denge konumları sergilediği bilinmektedir. Mevcut deneysel ve analitik çalışmalar parçacıkların nihai denge konumlarının neden farklı olduğuna dair ayrıntılı bir açıklama sunmakta yetersiz kalmaktadır. Ayrıca, şimdiye kadar yapılan çalışmalar yalnızca Newtonsal ve yüksüz viskoelastik sıvılarla sınırlıdır. Bu tez çalışmasında üçüncü olarak, elektroforez, akış ve viskoelastik sıvı kaynaklı kaldırma kuvvetlerinin birbiri ile etkileşimini ayrıntılı olarak açıklamak için bütüncül bir yaklaşım benimsenmiştir. Parçacık hizalanmasının kapsamlı bir şekilde anlaşılmasını sağlamak için Newton, yüksüz viskoelastik ve polielektrolit viskoelastik ortamlarda sıvı akış yönüne dik parçacık hareketleri deneysel olarak incelendi. Viskoelastik ortam ile yapılan deneyler neticesinde, şimdiye kadar yapılmış olan mevcut çalışmalardan daha farklı sonuçlar elde edildi. Sonrasında hem Newton hem de yüklü ve yüksüz viskoelastik sıvılarda gözlemlenen farklı parçacık hizalanma davranışlarına bütüncül bir yaklaşım ile açıklık getiren Elektro-Viskoelastik Hizalanma (EVH) teorisi geliştirildi. Buna ek olarak, EVH tekniğinde gözlenen farklı parçacık hizalanma davranışlarının altında yatan sebepleri keşfetmek için floresan etiketli viskoelastik polimer çözeltileri hazırlanarak konfokal mikroskop altında floresan boyalı polimerlerin hareketi incelendi.

Oldukça şaşırtıcı olarak sıvı akışına dik kanal kesitinde homojen olmayan viskoelastik çözelti oluşumu gözlemlendi. EVH tekniği ile elde edilen bu bulguların mikroakışkan camiasında şimdiye kadar keşfedilmemiş homojen olmayan viskoelastik akış gibi eşsiz uygulamalara kapı açacağı düşünülmektedir.

Özet olarak, sunulan sistemler tek bir düz mikrokılcal ya da mikrokanal üzerinde basit fabrikasyon teknikleri kullanılarak geliştirilmiştir. Akışkan düzeneği, optik, ve empedans tabanlı algılama üniteleri aynı akış sistemi üzerinde birbirine kolayca entegre edilebilir ve viskoelastik hizalama tekniği kullanılarak başarılı sitometri uygulamaları gerçekleştirilebilir. Mikroakışkan akış sitometri uygulamalarındaki yenilikçi yaklaşımımız viskoelastik sıvıların, gelişmekte olan ülkeler ve düşük gelir kaynaklı ortamlar için entegre, taşınabilir ve düşük maliyetli yeni nesil sitometri platformlarının geliştirilebilmesi adına iyi bir aday olduğunu göstermektedir. Buna ek olarak, EVH tekniği, jel elektroforez veya kromatografi uygulamalarının yerine geçebilecek seviyede, polyelektrolitlerin DNA fraksiyonlarının ve proteinlerin elektriksel yüklerine ve boyutlarına göre bir mikrokanal boyunca hassas bir şekilde hizalanmasını ve ayrıştırılmasını sağlayabilecek güçlü bir potansiyele sahiptir.

Anahtar sözcükler: Mikroakışkanlar, akış sitometrisi, viskoelastik solüsyonlar, parçacık hizalama.

Acknowledgement

I would like to express my deepest gratitude to my supervisor Prof. Caglar Elbuken for his encouragement and support. Life is full of challenges and I have been challenged by countless difficulties during my journey to a doctorate. I am deeply grateful to him for believing my ability and sharing his wisdom and advice as a guidance when I need most. I am deeply indebted to him for being more than a supervisor... A life-tutor, a guide, and an inspiration.

I would like to sincerely thank my committee members, Prof. Bülend Ortaç, Prof. Haluk Kulah, Prof. Aykut Erbas, and Prof. Lokman Uzun. Your advice, guidance and insights were much appreciated and helpful towards the evolution of this work. Moreover, I am deeply appreciated to Prof. Mehmet E. Solmaz for accepting me as his student, confidently giving me the responsibility of laser machining project, and encouraging me for the first three years of my doctorate studies. I am grateful to Prof. Engin Durgun for sharing his valuable time to share his life experiences, and friendly advices. They are truly enlightened my way during this journey.

I am very lucky to collaborate with my group member Mohammad Asghari. He is one of the most humble person I have ever know and his prescience view led to inspiration motivation for my doctorate studies.

I would like to thank, Mehmet Ali Godekmerdan, (müdürüm), for his endless support from the age of nine till the end of my life. Moreover I would also like to thank my companion, Mehmet Ali for his invaluable support from the beginning of my master studies till the end of my life. Their support is invaluable.

I am very fortunate to have Dr. Talha M. Khan and Dr. Ziya Isiksacan as true friends during my doctorate journey. Their friendship made my life easier and fruitful. I would like to thank Dr. M. Tahsin Guler, Dr. Ismail Bilican and Resul Saritas for their support and friendship.

I am grateful to Prof. Aykutlu Dana and Prof. Serdar Onses, for allowing me to collaborate in their studies. I was not alone on this doctorate journey. I am grateful to Dr. Abdullah Bayram, Dr. Sencer Ayas, Dr. Hasan Guner, Dr Gokhan Bakan, Dr. Mehmet Yilmaz, and my group members; Abtin Saateh, Dr. Ali Kalantarifard, Dr. Elnaz Alizadeh Haghighi, Pelin K. Isgor, Tolga O.

Celik, Dr. Nuray Gunduz, and Dr. Pinar Beyazkilic. I have the same feelings for my friends and colleagues in my former group; Hamit Eren, Dr. Ali Haider, Dr. Petro Deminskyi, Dr. Eda Goldenberg, Sait Ergoktas, Seda Kizir, Turkan Bayrak, Amira Ahmad, in Durgun group; Prof. Semran Ipek, Latif Onen, and Muammer Kanli, and in Ortac group; Yakup Midilli, Bartu Simsek, Elif Simsek, Busra Oz, Ugur Tegin, and Fehmiye Keles. All of the names listed here were very polite, supportive, and friendly to me. I would like to thank staff at UNAM, Zeynep Erdogan, Gokce Celik, Esra Karaaslan, Abdullah Kafadenk, Semih Bozkurt, Fikret Piri, and Semih Yasar.

I would like to express a very heartfelt thank you to my dear family. My parents have always cared and guided me. This dissertation is as much theirs as it is mine. My father is a true inspiration and his endless support made it possible to reach this point in my life. My mother loved me with everything she had. I would not be the person I am if not for the two of them. My sisters Merve and Sevde, showed me compassionate support and kindness for my entire life. My sister's husband Suat Kamil was always kind and supportive. My little niece Amine Gulce always increased my mood whenever I see her smiling face on the phone screen. My mother-, father- and brother-in-law always supported and kept their pray for me. I am appreciated to my sister-in-law Nuray for taking care of Elif Sare and creating time for me to write my thesis.

For the last but the most sincere gratitude to my beautiful wife, Seda. She believed in me and supported me through my entire studies. Life is treasures with her love. Our daughter Elif Sare is more valuable than the most precious stones in the world. Thank both of you for shaping my life with your existence and heartfelt love.

There are more names, professors, colleagues, and friends that I cannot list in this short page; however, I am very indebted and grateful to each one of them for their support and love.

dedicated to my wife, mother, father, and daughter Elif Sare...

Contents

1 Introduction **1**

1.1 Flow cytometry concepts 2

1.2 Microfluidics 9

1.2.1 Overview 9

1.2.2 Miniaturization in flow cytometry 10

1.2.3 Microfluidic platforms 11

1.2.4 Physics of microfluidics 13

1.2.5 Flow behavior and viscoelasticity 16

1.3 Particle focusing in microfluidic flow cytometry applications . . . 24

1.4 Thesis Outline 29

2 Optical-based microfluidic flow cytometry using viscoelastic fluids **32**

2.1 Introduction 33

2.2 Materials and methods 35

2.2.1 Sample preparation 35

2.2.2 Device fabrication 36

2.2.3 Experimental setup 37

2.3 Results and discussion 39

2.3.1 Numerical results 39

2.3.2 Experimental results on cytometry performance 40

2.4 Concluding remarks 47

3 Impedance-based microfluidic flow cytometry using viscoelastic fluids **48**

3.1 Introduction 49
3.2 Materials and methods 50
3.2.1 Sample preparation 50
3.2.2 Device fabrication 50
3.2.3 Experimental setup and working principle 53
3.3 Results and discussion 55
3.3.1 Solution characterization 55
3.3.2 Flow focusing vs ionic buffer concentration for particles . . 57
3.3.3 Impedance-based cytometry measurements 62
3.4 Concluding remarks 67

4 A unifying study on electro-viscoelastic migration (EVM) under simultaneously applied pressure-driven flow and electric field 69
4.1 Introduction 70
4.2 Materials and methods 73
4.2.1 Sample preparation 73
4.2.2 Device fabrication 74
4.2.3 Experimental Setup 75
4.3 Results and discussion 76
4.3.1 Particle migration experiments 78
4.3.2 Principle of EVM using dominant lift forces 81
4.4 Experimental attempts to prove the EVM hypothesis 85
4.4.1 Measurement of polymeric concentration change via HA solution conductivity in the trifurcated channel 86
4.4.2 Confocal imaging experiments of the fluorescent dye-labeled polymer viscoelastic solutions 90
4.4.3 EVM for varying viscoelastic polymer concentrations . . . 92
4.4.4 Enhanced viscoelastic migration in Neu-EVM for central 3D particle focusing cytometry applications 93
4.5 Conclusion 97

5 Summary and Future outlook 100
5.1 Summary 100
5.2 Future outlook 102

A Publication List **125**

List of Figures

1.1 Examples on commercial flow cytometry. (a) An overview, (b) optical detection unit of BD Acurri C6, (c) flow cell in BD FACSCanto, and (d) fluidic units in BD FACSVerse 3
1.2 An illustration of optical flow cytometry. (a) detection units and (b) demonstration of the scattered lights from the particle of interest 4
1.3 Illustration of impedance flow cytometry. (a) Side view schematics of microfluidic based flow cytometry system, (b) coplanar electrode configuration and top-bottom electrode configuration. $Z_{AC} - Z_{BC}$ differential impedance signal is measured while particle passing over electrodes. Transit time is the time difference between two peak amplitudes. 7
1.4 The increasing trend of publications in three topics: Flow cytometry, Microfluidics, and Microfluidic Flow Cytometry obtained from Web of Science. 11
1.5 Examples of different type of microfluidic chips. (a) Glass microcapillary, (b) fused silica all-glass microfluidic chip, (c) glass/PDMS microfluidic chip with metal electrodes, (d) scanning electron microscope (SEM) image of glass/PDMS microchannel, and (e) Kapton tape sealed flexible PDMS serpentine microchannel. 12
1.6 Fabrication steps to prepare a PDMS microfluidic device. (a) Mold, (b) PDMS pouring, (c) curing on a hot plate, and (d) peeling PDMS layer form mold. 13
1.7 Navier-Stokes equation with captions for variables. 14
1.8 Poiseuille flow profile in two boundary system. 15

1.9 Illustration of (a) parallel plate system, (b) two parallel plates model represents shear and velocity change, and (c) Laminar flow distribution. 17
1.10 Illustration of models. (a) Ideally viscous behavior with dashpot model, (b) ideally elastic behavior with spring model, and (c) viscoelastic model with spring and dashpot Maxwell model. 18
1.11 Illustration of shear thinning profiles. (a) Viscosity change for dense polymeric solution, (b) dependence of polymer concentration, and (c) molecular weight on shear viscosity. 20
1.12 Flow profiles for different type of materials. (a) Time dependent shear rate ramping, (b) flow curves, and (c) viscosity functions of ideally viscous (1), shear thinning (2) and thickening (3) behavior. 21
1.13 Illustration of stress tensor and stress components in x, y, and z directions. 22
1.14 Particle migration in Newtonian and viscoelastic solution. (a) Poiseuille flow distribution, (b) Newtonian solution, and (c) viscoelastic solution 27
1.15 Illustration of dominant force gradient, force arrow-field, and equilibrium particle positions for both inertial and viscoelastic focusing in circular and square cross section channel profiles 28

2.1 Schematic illustration of examples in the literatures for optical microfluidic flow cytometry studies. (a) Reproduced from Ref. [1] with permission from the American Chemical Society, (b) reproduced from Ref. [2] with permission from the American Institute of Physics, (c) reproduced from Ref. [3] with permission from the Elsevier, (d) reproduced from Ref. [4] with permission from the Wiley Online Library, (e) reproduced from Ref. [5] with permission from IEEE, and (f) reproduced from Ref. [6] with permission from American Institute of Physics. 34

2.2 Schematic illustration of sheathless microfluidic flow cytometry setup. (a) Consisting of the assembled chip, a 635 nm laser diode, a laser driver, a pressure pump, an oscilloscope, and Si photodetectors. (b) Schematic illustration of assembled components (not to scale). 35
2.3 Preparation of capillary tube. (a) 160 µm O.D., 60 µm I.D. capillary tube with 10 µm polyamide coating. (b) Polyamide coating was removed in sulfuric acid. (c) Ball lens protection cap to isolate the inner channel. (d) Capillary tube after 20 minutes of HF etching. 36
2.4 Viscoelastic microfluidic cytometry setup. (a) Capillary channel and PMMA holders (holders 1, 2, and 3) to assemble the capillary tube and optical fibers. (b) Overview of the experimental setup; capillary device, laser driver, oscilloscope, pressure pump, and photodetectors. (c) Closer look-up of viscoelastic microfluidic cytometry. An image during the experiment (d) showing the optical interrogation region (laser-on) and (e) particles inside the capillary tube (laser-off). 38
2.5 Viscoelastic microfluidic cytometry results of FSC and SSC signals in HA-based viscoelastic solution for 6 µm diameter polystyrene beads (a) 200 ms and (b) 3 ms closer look-up. 42
2.6 HA-based viscoelastic flow cytometry results for 6 µm diameter polystyrene beads. (a) Scatter plot of FSC vs. SSC events and (b) Histograms of FSC and SSC signals. 43
2.7 PEO based viscoelastic flow cytometry results. (a) Scatter plot of FSC to SSC events and (b) Histograms of FSC and SSC signals. . 44
2.8 PVP based viscoelastic flow cytometry results (a) Scatter plot of FSC to SSC events and (b) Histograms of FSC and SSC signals without gating. 44

2.9 Comparison of the reported cytometers reported in the literature based on the particle focusing method. The CV values reported here are from either forward scatter (FSC), side scatter (SSC) or fluorescence (FL) measurements. If multiple values were reported in the same study, the lower CV value (i.e., best performance) was reflected in the chart. For some studies, experiments were performed with the different sizes of particles, which is also reflected in the chart. The HA-based sheathless microfluidic cytometry yields a CV value of 5.8% for FSC measurement. 46

3.1 Illustration of the fabrication steps for impedance cytometry device. 51

3.2 Microscope images of the fabricated device. (a) 10 µm electrodes on glass, (b) PDMS channel and glass substrate aligned on top of each other, (c) cross section, and (d) top view of PDMS channel. . 52

3.3 Illustration of the impedance-based viscoelastic flow cytometer. . 54

3.4 A photography of experimental setup and fabricated viscoelastic impedance cytometry device. Pogo pins are used to make connections between electrodes and lock-in amplifier units via SMA connectors on the FR2 circuit board. 54

3.5 Shear rate dependence of viscosity of PEO solutions: (a) four different M_w PEO solutions at 0.1% w/v concentration, the error bars represent 2 S.D. of five multiple measurements, (b) five concentrations of PEO_{5MDa} solution (the error bars are smaller than the measurement markers), and (c) 0.1% w/v PEO5MDa solution at three ionic concentrations and DI Water 56

3.6 Shear rate and ionic concentration dependence of viscosity of HA solutions for different polymer concentrations: (a) 0.1% w/v and (b) 0.5% w/v. 57

3.7 Image stacks of focusing of 6 µm diameter PS beads (a) PS beads suspended in 500 ppm, PEO_{5MDa} dissolved in 1X PBS solution and (b) PS beads suspended in 500 ppm, PEO_{5MDa} dissolved in 3X and 10X PBS solutions. 59

3.8 Image-stacking images of the focusing RBCs. RBCs suspended in 500 ppm, PEO_{5MDa} dissolved in 1X PBS solution. 61

3.9 Impedance cytometry results for (a) PS beads and (b) RBCs at 50 mbar inlet pressure (left). Close-up images of single-particle events showing the characteristic differential impedance signal profile (middle). Histogram plots of transit time and peak amplitudes corresponding to all events (right). 62

3.10 Viscoelastic impedance cytometry results for 6 µm diameter PS beads at 50 mbar inlet pressure. 10 s time window data using 500 ppm PEO_{5MDa} viscoelastic solutions with varying PBS concentrations: (a) 1X PBS, (b) 3X PBS, (c) 10X PBS, and (d) histogram plots and statistical results of peak amplitudes for 1 min. 63

3.11 Optical microscope images for RBC suspension in (a) DI Water, (b) PEO_{5MDa}, (c-d) 1X-PBS/PEO, (e) 1X-PBS, (f) 3X-PBS, and (g) 10X-PBS. 64

3.12 Bar chart representation of transit time, peak amplitude, and % CV of (a) PS beads and (b) RBCs detected at varying inlet pressures. For each bar graph, the square represents the mean value, the box represents the standard deviation, and the whisker lines represent the 99% and 1% population of the counted events. . . . 66

3.13 Scatter plots of transit times vs peak amplitudes at four inlet pressures for RBC impedance measurements. 67

4.1 Schematic illustration of the reported studies in the literature for migration under simultaneously applied pressure-driven flow and electric field configuration. (a) Studies are categorized according to the medium (outer ring) and the particles of interest (the inner circle) as a pie chart. (b) Schematic of the particle equilibrium states at the outlet cross sections in a microfluidic channel according to the electric field direction, medium, and suspended particles. The first four groups (I-IV) are cited from the literature, and the fifth group (V) represents our study of particle migration in polyelectrolyte viscoelastic solution. F_{EP}: electrophoretic force, PDF: Pressure-driven flow. 71

4.2 Illustration of the microfluidic test setup and summary of particle equilibrium states at the microchannel outlet cross sections. (a) Photo of the fabricated microfluidic chip. (b) Schematic representation of the experimental system. (c) Illustration of the electric field, electrophoretic force, and Poiseuille flow distribution in the microchannel. (d) Illustration of particle equilibrium positions at the outlet cross section. 72
4.3 Shear viscosity measurement as a function of shear rate. 74
4.4 Top-view image stacked photos for viscoelastic focusing experiments with PEO- and HA-based viscoelastic solutions for varying inlet pressures. The single stream of particles in the middle of the channel indicates migration to the channel center. 79
4.5 Top-view image-stacked photos of high-speed camera recordings for particle migration under pressure-driven flow and simultaneously applied pressure-driven flow and DC electric field. 81
4.6 Illustrative explanation of particle migration in Newtonian and neutral viscoelastic solutions. Particle migration in Newtonian solution for (a) pressure-only, (b) concurrent, (c) countercurrent cases, in neutral viscoelastic solution for (d) pressure-only, (e) concurrent, and (f) countercurrent cases. Green spring, blue, and red arrows represent the PEO polymer stretching, shear gradient lift force, and elastic lift force, respectively. The color-chart on the left-hand side of the channel represents the shear gradient profile. 83
4.7 Development of particle migration in HA-based viscoelastic solutions at the outlet cross section of the channel under simultaneously applied pressure-driven flow and electric field. The blue color gradient bar represents the concentration gradient at the channel cross section. The color chart on the right represents the polymer concentration gradient. 85

4.8 Concentration vs conductance measurements to validate polymer migration in HA viscoelastic solution with EVM theory. (a) a photo, and (b) illustrative drawing of sample collection trifurcated chip, (c) a photo, and (d) illustrative drawing of the measurement setup. 87
4.9 Illustrative drawing explaining the polymer migration experiments. (a) Trifurcated chip, (b) Characterization of conductance-based concentration measurement system for varying concentration of PEO samples, (c) An illustrative drawing as a reminder of how polymer migration occurs at the channel cross section for each test modes, and (d) Average of 4 different concentration vs conductance measurement results for HA viscoelastic solutions at only pressure-driven-flow, concurrent, and countercurrent test modes. 88
4.10 Confocal imaging results for uniform and non-uniform concentration distribution of fluorescently tagged viscoelastic solutions at the channel cross section near the outlet. Polymers are observed in three different modes: pressure-only, concurrent, and countercurrent. The applied electric field is 200 V/cm for the concurrent and countercurrent modes. (a) Schematic drawing of the channel and scanning volume. Confocal scanning region is 60 x 120 x 120 μm^3.(b) Scanning electron microscope (SEM) of the channel cross section (c-d) Coumarin 343 tagged-PEO, and (e-f) DAPI tagged-HA. 89
4.11 2D maximum intensity projection images for (a) HA, (b) PEO and intensity plots for (c) HA, and (d) PEO. 91
4.12 Top-view image-stacked photos of high-speed camera recordings to show the effect of polymeric concentration on particle equilibrium positions at the channel outlet for Neu-EVM and Ply-EVM in pressure-only, concurrent and countercurrent tests. The electric field is applied at 200 V/cm. c^*_{PEO} =473 ppm and c^*_{HA}=988 ppm. 94
4.13 Particle stream width versus electric field at different particle travel distances in the concurrent case of Neu-EVM mode. 96

4.14 Particle distribution at the channel cross section versus electric field at different particle travel distances in concurrent case of Neu-EVM mode. For each bar graph, the square represents the mean value, the box represents the standard deviation (S.D.), and the whisker lines represent the 99% to 1% population of the counted events. 97

A.1 Electrophoresis front cover [7] 126

List of Tables

2.1 Rheological parameters for viscoelastic solutions. 41
2.2 Calculation of dimensionless numbers and experimental parameters for flow cytometry experiments. 41
2.3 Flow cytometry results: mean value, standard deviation, and coefficient of variation (%CV). 45
2.4 Comparison of HA-based sheathless microfluidic cytometry (HA-MFC) and commercial BD Accuri D6 flow cytometry for 6 µm particles. 45

3.1 Dimensionless numbers and experimental parameters for the bead experiment. 58
3.2 Dimensionless numbers and experimental parameters for the RBC experiment. 58

4.1 Rheological properties for PEO_{5MDa} at different concentrations. . 78
4.2 Rheological properties for $HA_{1.5MDa}$ at different concentrations. . 78
4.3 Dimensionless numbers of 500 ppm PEO_{5MDa} 80
4.4 Dimensionless numbers of 1000 ppm $HA_{1.5MDa}$ 80
4.5 Dimensionless numbers of varying concentration PEO_{5MDa} 93
4.6 Dimensionless numbers of varying concentration $HA_{1.5MDa}$ 93

Chapter 1

Introduction

In this chapter, general background and overview of the contents, and the motivation of the thesis are provided. Introduction to flow cytometry is given. Flow cytometry methods are briefly explained with their historical background. The increasing demand for flow cytometry on the market and boosted scientific interest in microfluidic flow cytometry devices is pointed. Microfluidics and microfluidic platforms are discussed very briefly. Fundamentals and theoretical background of microfluidics are provided. Fluid viscoelasticity and particle migration in a microfluidic flow cytometry device are reported. Finally, the outline of the rest of the thesis is given.

(Part of this study was published as; M. Serhatlioglu, C. Elbuken, B. Ortaç, M. E. Solmaz, Femtosecond laser fabrication of fiber based optofluidic platform for flow cytometry applications, Proc. SPIE 10058, Optical Fibers and Sensors for Medical Diagnostics and Treatment Applications XVII, pp. 100580I, 2017. Reproduced (or 'Reproduced in part') from Ref. [8] with permission from SPIE. https://doi.org/10.1117/12.2252092)

1.1 Flow cytometry concepts

Cytometry is a combination of two Greek words: Cyto; *Kytos*-hollow container, and metry; *Metria*-measuring process. Flow Cytometry performs automated measurement in a single cell level to acquire the multiple physical/chemical properties of cells and phenotype individual cells in a population to understand the heterogeneity of the entire system under the fluid stream.

History of flow cytometry and automated particle counting starts in parallel with the improvements in the field of microscopy in 19th century. Pioneering developments such as UV microscopy (1904), phase contrast imaging to observe transparent cells (1932), and antibody labeling with a fluorescent dye (1941) lead the way through flow cytometry [9]. The first attempt for automated cell-counting was performed by Moldovan 1934, yet Gucker demonstrated the first successful flow cytometry in 1947 with the development of early photomultiplier tubes [9]. Blood count was successfully demonstrated in 1953 by Crossland-Taylor, thanks to the development of hydrodynamic cell focusing. The same year impedance-based cell counters were discovered by Wallace H. Coulter. This discovery had great importance since the coulter counter mechanism later used to demonstrate the cell sorting system by Fulwyler (1965). 1CP 11, Pertec Company, was the first initiative to a successful commercial fluorescence-based flow cytometry (1969). Fluorescence-activated cell sorter (FACS) system was discovered by Leonard and commercialized under the Becton Dickinson Company (1974). Early cytometry systems were aimed on extracting a single parameter. The very first demonstration of multi-parametric two-color flow cytometry developed by Leonard Herzenberh (1977). Later, the demonstration of three-color flow cytometry measurement provided burst attention in the field (1984).

Simultaneous multiple parameter measurements enabled the variety of applications in the clinical trials. Today's high-end multi-color flow cytometry technologies are capable of having 3 excitation lasers, with up to 21 fluorescence channels and 23 independent detectors (Agilent NovoCyte Avanteon). An example of a commercially available optical flow cytometry by BD Biosciences is given in Figure 1.1 [10]. The history of the state-of-the-art flow cytometers, their

development time-frames, and future perspectives on cell cytometry discussed in given references [9, 11–13].

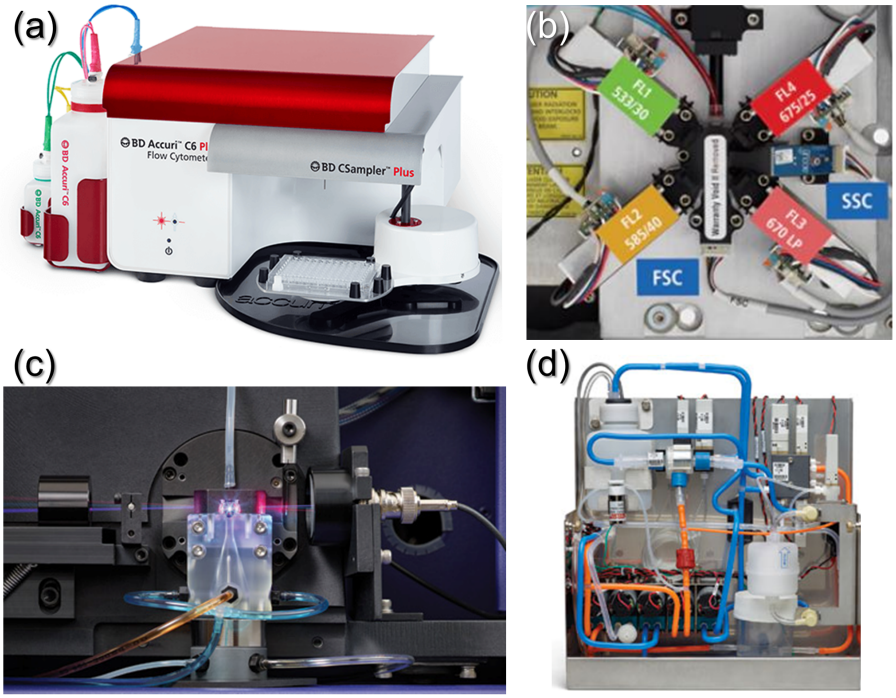


Figure 1.1: Examples on commercial flow cytometry. (a) An overview, (b) optical detection unit of BD Acurri C6, (c) flow cell in BD FACSCanto, and (d) fluidic units in BD FACSVerse

Flow cytometry is a well-established technique for automated multiparameter analysis of suspended cells and particles for biomedical applications and clinical research. The ability to identify and count the number of biological particles in-vitro based on their size have crucial importance for diagnosing and monitoring various diseases such as CD4 T-lymphocyte counting in HIV [14] and malignant epithelial cell immunophenotyping [15]. Today commercially available benchtop flow cytometers mainly use three measurement methods: optical, impedance, and imaging. The optical measurement is a widely available method, using optical detection technique that requires the interaction of a laser beam with the sequentially aligned particles of interest in a flow cell. A generic optical flow cytometer consists of four units, as shown in Figure 1.2. Flow unit; guides sheath and sample fluid to the light interaction region and assists sheath-supported 3D hydrodynamic focusing for the particles of interest before the light interaction

region. Light interaction unit is responsible for particle detection and consists of laser/lasers at a specific wavelength, free optics, lenses, filters, photodetectors (PD), photomultiplier tubes (PMT). Signal processing unit provides real-time data processing from the measurement with data acquisition board, amplifier circuits, and an optional sorting unit, for particle sorting as regard to the desired specificity.

Optical flow cytometry data is processed mainly from three types of optical signals which are scattered/collected from the particles during their passage from the light interaction region. Light interaction with cell exterior and subcellular contents like vesicles scatter the light in different directions. Forward scattering light (FSC) is collected at the direct opposite side of the laser source with a small angle rotation (0-15°) and gives the information about particle size and particle surface area. Side scattering light (SSC) provides information about particle granularity and has wider angle placement (30-180°). Fluorescent emitted light (FL) is collected as side scattered light using selectively arranged band-pass filters according to specific fluorescent labeling of individual particles. The use of laser excitation is the most significant advantage of optical flow cytometry.

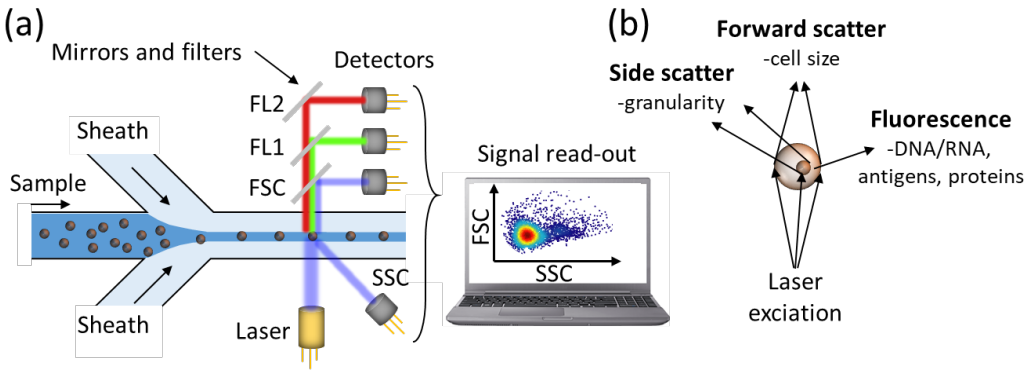


Figure 1.2: An illustration of optical flow cytometry. (a) detection units and (b) demonstration of the scattered lights from the particle of interest

The impedance measurement is the second widely available flow cytometry method measures cellular biophysical properties with electrical impedance change [16]. The early Impedance flow cytometers used Coulter principle, which is developed by Wallace H. Coulter in 1953 and rapidly commercialized in 3 years.

Following the demonstration of electrical single-cell detection, Coulter counters have become one of the most commonly used research tools for particle detection and enumeration studies [17].

Implementation of the technique using microfabricated structures was first demonstrated for the detection of latex nanoparticles [18]. Coulter counter uses direct current (DC) to measure the resistance change during the displacement of particles through a narrow orifice. The orifice is the sensing region and has a relatively similar size in comparison to the particles suspended in ionic buffers (e.g., PBS) or electrolyte solutions. Polymeric particles or cell membrane behaves as an insulation layer under DC electric field; thus, the resistance of the orifice changes due to the replacement of the conductive liquid. The variation in DC resistance is in accordance with the particle size and geometry. Counted events are recorded while the particles are passing through the orifice. The number of counted events gives information about the particle population, and the amplitude of the signal corresponds to the particle volume. It is possible to differentiate the individual type of cells in heterogeneous media by defining threshold over a signal amplitude [19]. Early Coulter counter measurements were blood cell analysis, microorganism, and nanometer-size particles like viruses and vesicles [20, 21].

Coulter counters used direct current on the sensing region; later, low-frequency signal was integrated into the system to require more information on cell nature [22]. Various designs have been recommended to increase the performance of microfluidic Coulter counters [23–26]. Impedance flow cytometry was introduced as an improved version of Coulter counter that employs AC electric field instead of a DC signal. Frequency of AC signal gives characteristic information about the particles of interest. While conventional Coulter counters only classify cells based on their size, impedance flow cytometers provide a detailed analysis of single cells [27–29] at multiple frequencies. Impedance flow cytometry is used in some commercial clinical analysis devices for full blood count, white blood cell differentiation, nucleated red blood cell count, and reticulocyte count [30]. Further improvements were possible for impedance cytometers using microfabrication technologies in microfluidic applications. Instead of using a small orifice to intensify the electric field in a small region, microfluidic impedance cytometers use

metal electrodes integrated into the microchannel. The electric field applied from the integrated electrodes which defines the electrical sensing region for particles to be detected.

Impedance flow cytometers consist of three units: Flow unit, electric field interaction region, and signal processing unit. Flow unit where particles are flushed through the channel, as a similar principle to the optical flow cytometers. Electric field interaction region consists of metal electrodes configured either coplanar or top-bottom configuration. Signal processing and amplification unit which provides real-time data processing from the measurement using data acquisition board, lock-in amplifier circuits analog-digital converters, and custom electronics. Microfluidic impedance cytometers mostly use coplanar electrodes, causing measurement variations due to non-homogeneous electric field. The impedance measurement signal is position-dependent for coplanar electrode configuration since each particle has a different trajectory and interacts with different intensity of the electric field. Therefore, particle focusing techniques (discussed in section 1.3) are mostly required to reach a single train of particles and improve the measurement accuracy.

The first single-cell detection in microfluidic impedance cytometry was carried out by Ayliffe and his colleagues [31]. Gawad and Renaud are pioneers in the field, and they demonstrated early microfluidic impedance cytometry applications by differentiating micron-sized polystyrene beads [28] and blood cells [32]. They demonstrated measurement in both coplanar and top-bottom electrode configurations integrated with the microfluidic channel (illustrated in Figure 1.3).

The impedance measurements are based on sensing differential change $Z_{AC} - Z_{BC}$ on the electrical signal when particles are passing over the electrodes and interacting with the electric field. Two electrode segments (sensing and reference segments) are used to measure the cell properties directly against the surrounding media to prevent errors by any uneven change in the electrode properties [28]. The particle transition time (t_{tr}) is defined by the time difference between the signal maximum and minimum points and gives information about the speed of the particle. The information on voltage signal amplitude depends on the

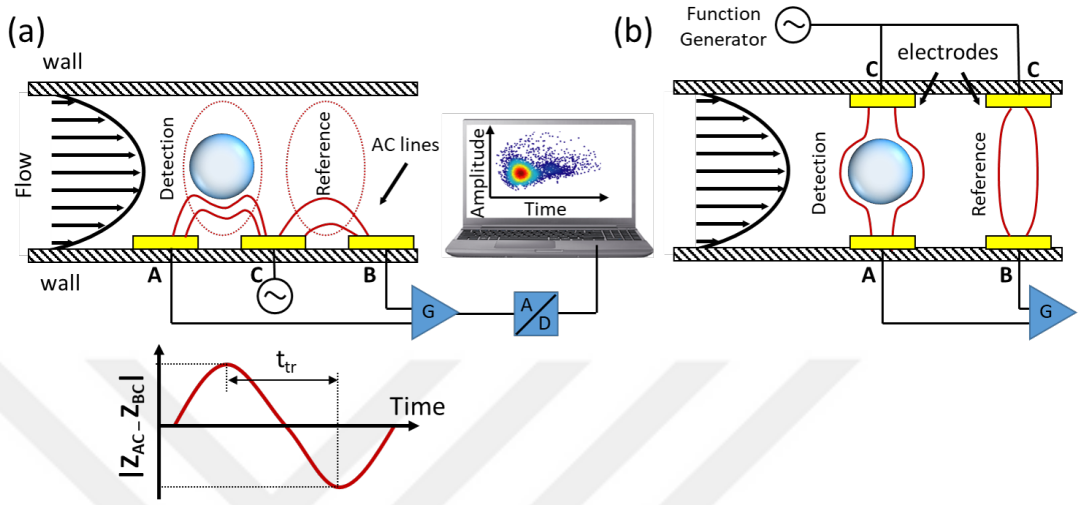


Figure 1.3: Illustration of impedance flow cytometry. (a) Side view schematics of microfluidic based flow cytometry system, (b) coplanar electrode configuration and top-bottom electrode configuration. $Z_{AC} - Z_{BC}$ differential impedance signal is measured while particle passing over electrodes. Transit time is the time difference between two peak amplitudes.

excitation frequency. At low frequencies, cell membrane behaves like an insulator and stands as a barrier. Current flows through outer region of the cell. Thus the measured amplitude is corresponds to the cell size. It is the reason why in Coulter counters, cells with the same size but different interiors can not be differentiated. Mid-range frequencies give information about the cell membrane properties. At high frequencies cell membrane does not stand as a barrier and current goes through cell interior. Thus the amplitude of the signal gives information about dielectric properties of the cell cytoplasm.

Opacity is the ratio of high frequency to low frequency impedance magnitude and provides normalized data for cell size and position [32]. This also helps to identify cells with the same geometrical size but different interior content [22]. Opacity measurement can provide cellular biomarkers to classify different cell types such as tumor, stem, and blood cells [13].

Impedance cytometry is advantageous for label-free applications and mainly

suitable for enumeration and morphology measurements. The significant advantage of impedance cytometers is making measurements with optics-free configuration. Thus the systems are free of high-end optical laser sources/detectors and laser alignment procedures. Today's commercial benchtop impedance analyzers (Coulter counters and flow cytometers) are mostly targeted for multiple particle enumeration and whole blood analysis. Tandem use with optical flow cytometry units is also a common application for impedance analyzers to improve the accuracy and capability of the system.

Imaging flow cytometry is the third cytometry method and has become popular for the last decade due to improvements in digital imaging systems and real-time image analysis algorithms. The auto focusing technique provides fast image tracking for flowing cells in real-time, and it is combined with machine learning algorithms to acquire clinically accurate and intelligent data [33]. Imaging flow cytometry systems are advantageous compared to optical and impedance-based alternatives since the measurement data can be provided from high-resolution images with an affordable price camera without the need of fluorescent labeling, high-end optical detectors, and microelectrode fabrication. An imaging flow cytometry is capable of cell counting and enumeration. It is used to narrate morphological changes even for challenging samples for optical or impedimetric systems.

Optical flow cytometers do not process and store the real image of the particle of interest. The cytometry data is mostly provided from interpreted data (voltage response of scattered optical light on photodetector). In imaging-based systems, the real image of the particle of interest is stored and processed. Thus, it provides a clear advantage to detect very similar morphological changes. It is also possible to equip the image-based cytometers with fluorescence or confocal microscopy configuration to generate information from fluorescent data on single events of a heterogeneous population. One of the major challenges in optical and impedance flow cytometers is the requirement of flow focusing unit and sample dilution to guarantee only one particle is passing through the sensing region. However, image flow cytometry systems can handle multiple particles (hundreds of thousands) with a single frame image at single-cell resolution using less diluted

samples. Besides, it is possible to make multiple sample flow channels to increase the throughput of the system [34]. Modern image flow cytometers are equipped with optical cytometry units in a tandem configuration to use the mutual benefits of each method. Imaging flow cytometers are not less capable than optical or impedance-based systems for single-cell detection applications; however, high computation load, fast image processing in real-time, and large raw data size are the challenges in the market.

1.2 Microfluidics

1.2.1 Overview

Microfluidics is a multidisciplinary field. Microfluidic platforms are a meet up of four main subjects: physics, mechanics, medicine, and chemistry. Microfluidics processes small fraction of sample from nL to fL volumes, in the micron to nanometer size fluidic channels to acquire physical information from a sample of interest using a detection method. Technological developments in microfabrication techniques and microchip technologies lead the way to high capable microfluidic systems [35,36]. First microfluidic application appeared in 1992 [37,38] in capillary format for the efforts of miniaturization of chromatography tubes; then, they took great attention in the industrial and scientific community. A widely used term in microfluidics, Micro Total Analysis Sytems (µTAS), was introduced during the same period [39]. The primary motivation in µTAS is mostly fueled by one or more of the following features: fast, accurate and precise measurement, low sample requirement, small and light-weight dimensions, and low power consumption. Microfluidics is considered to be the root of today's lab-on-a-chip (LOC) and point-of-care (POC) devices. The global market share of Microfluidic devices is evaluated as $13.5 billion at the end of 2019 [40]. The driving engine of the market is currently POC devices. Increasing demand in high throughput, fast and accurate measurements with minimal errors, low sample requirement, and in-vitro diagnosis tools are shaping the future direction of Microfluidics industry. One of the market leader company, Abbott, has recently announced a breakthrough achievement that they developed a POC device that

detects the novel coronavirus, COVID-19, (globally spread coronavirus pandemic in 2019-2020) positive results in only five minutes [41].

1.2.2 Miniaturization in flow cytometry

The last century was dominated by the trend of miniaturization in manufacturing smaller size optics, electronics, and mechanics. Miniaturization is also essential for the future-generation flow cytometry platforms. State of the art flow cytometry systems use bulk optics that have alignment issues, require large sample volumes, are expensive to buy and maintain, and require a qualified user for utilization and maintenance. The demand for the use of flow cytometry is increasing globally. The global market share of flow cytometry systems is estimated to reach $6.5 billion by the end of 2025 [42].

In the last two decades, there has been considerable interest in microfluidic lab-on-a-chip systems towards fast bio-analysis and examination feaures while using a vastly smaller sample volume. Microfluidic based flow cytometers have attracted a great deal of interest since they are advantageous for miniaturization aspects, low-cost fabrication and production, a small amount of sample requirement, high throughput and measurement precision and operating without a need for a qualified operator. It also enables the integration capability of optical elements or impedance detection units into a single chip. The majority of the miniaturization efforts are made in the microfabrication of fluidic parts in flow cytometers. Additionally, the optical excitation/detection region, and impedance measurement parts (microelectrodes) are integrated into microfluidic chips [43, 44].

Microfluidic integration made it possible to produce portable and low-cost flow cytometers [16], widely available for emerging countries and hard environmental settings. For instance, NASA tested Microflow Flow Cytometry in International Space Station (ISS) in 2014 [45]. Microflow accurately responded to the measurements in a microgravity environment and measured a wide variety of specimens. It was also successfully used to track the physical blood properties of astronauts in ISS on daily basis.

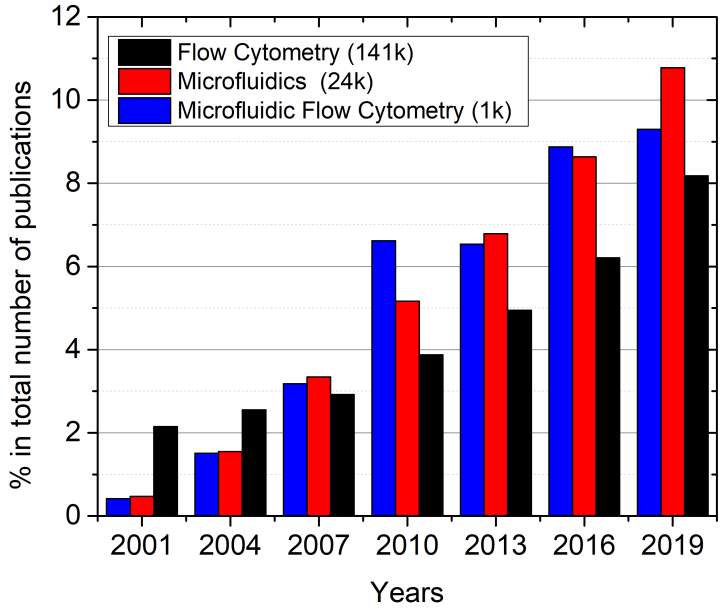


Figure 1.4: The increasing trend of publications in three topics: Flow cytometry, Microfluidics, and Microfluidic Flow Cytometry obtained from Web of Science.

The interest in the microfluidic flow cytometry studies is increasing in the academic community as well as industry. Figure 1.4 shows the increase in the number of scientific publications published for the last 20 years in Web of Science database by the keywords of "Flow Cytometry", "Microfluidics", and "Microfluidic Flow Cytometry". The x-axis of the graph shows the number of publications by year, and the y-axis shows the percentage of the publications in total (141k for Flow Cytometry, 24k for microfluidics, and 1k for Microfluidic Flow Cytometry). The continuously increasing trend line is a clear evidence of the demand for microfluidic flow cytometry studies.

1.2.3 Microfluidic platforms

Microfluidic devices are fabricated using four types of materials: paper, polymers, silicon, and glass. Paper has a complex environment and lack of accuracy

for longer test duration; however, one of the most successful and globally available test kit, pregnancy test, is based on paper microfluidics. Polymers are cost-effective and easy to fabricate. They suffer from chemical stability for a long duration or multiple-use applications; however, they are good candidates for single-use applications. Polymer microfluidics is compatible with mass-production for industrial applications using hot embossing and injection molding. Silicon and glass show better chemical and mechanical stability. Silicon is the milestone for the microfabrication industry. However, the material is opaque to visible light. Thus it does not give the desired performance for visualization and hence not preferred for optical or imaging flow cytometry applications in visible range. Glass surfaces are chemically inert, mechanically stable, and optically transparent to a broad spectrum of light. Glass-based microfluidic fabrication with well-known microfabrication techniques are generally considered costly and time consuming compared to paper or polymer-based chip fabrication. Laser fabrication techniques open the doors of cost and time reduced fabrication for complex structures with glass-based transparent microfluidic devices [46–51]. Examples of different microfluidic platforms are given in Figure 1.5.

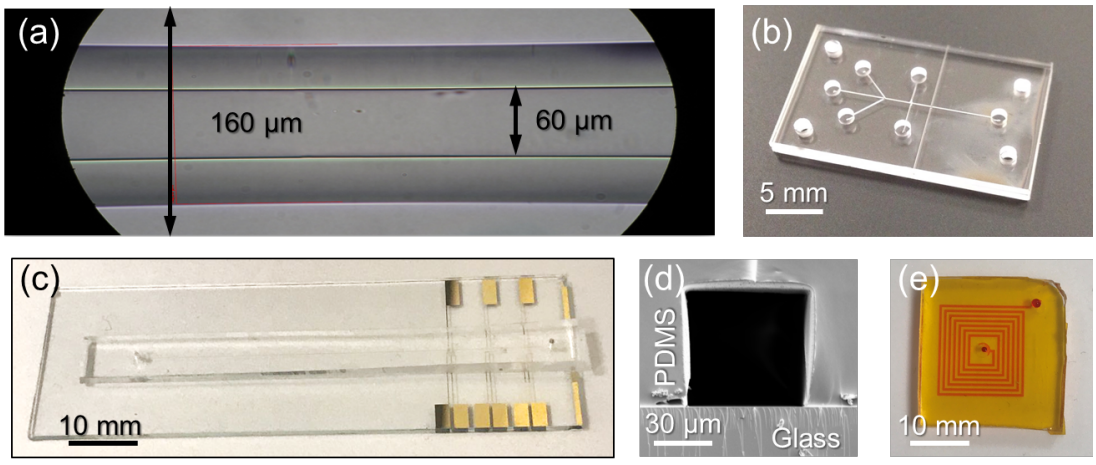


Figure 1.5: Examples of different type of microfluidic chips. (a) Glass microcapillary, (b) fused silica all-glass microfluidic chip, (c) glass/PDMS microfluidic chip with metal electrodes, (d) scanning electron microscope (SEM) image of glass/PDMS microchannel, and (e) Kapton tape sealed flexible PDMS serpentine microchannel.

PDMS devices are widely used in microfluidic studies. Fabrication steps for

a generic PDMS microfluidic device is illustrated in Figure 1.6 (more details are available in the following chapters). Initially, a master mold is prepared to replicate the structures (Figure 1.6.a). Then, PDMS and curing agent are mixed at 10:1 ratio (the most common recipe), degassed in a vacuum chamber and poured onto the mold (Figure 1.6.b). Later PDMS layer is cured on a hot plate (Figure 1.6.c). Finally, cured PDMS is peeled off from the mold (Figure 1.6.d).

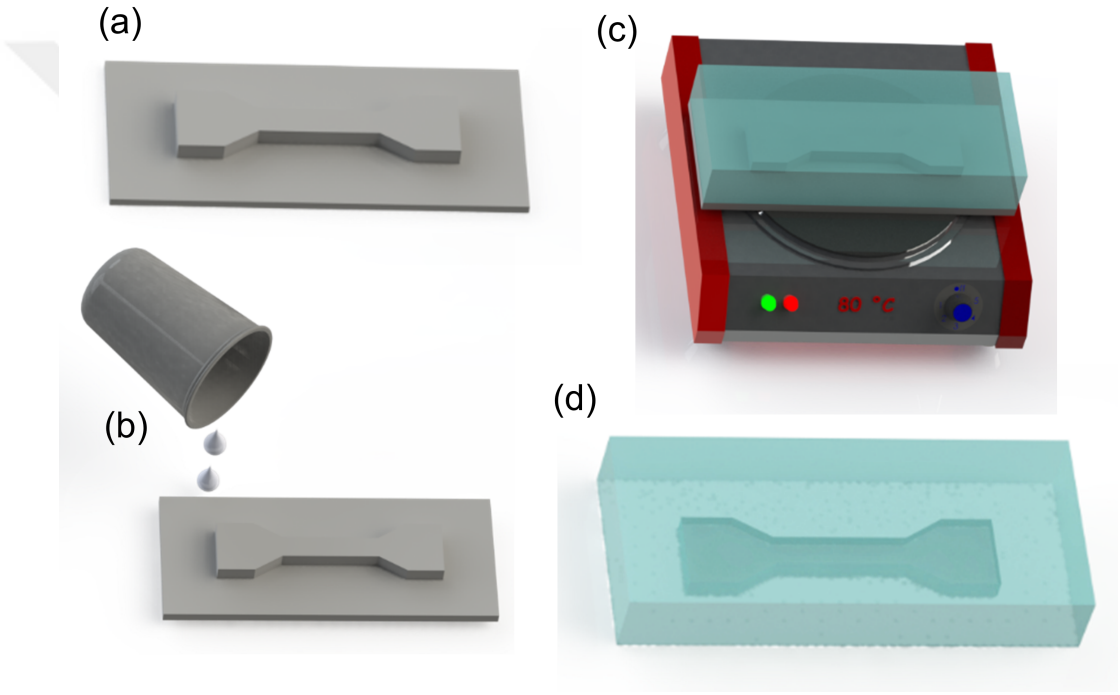


Figure 1.6: Fabrication steps to prepare a PDMS microfluidic device. (a) Mold, (b) PDMS pouring, (c) curing on a hot plate, and (d) peeling PDMS layer form mold.

1.2.4 Physics of microfluidics

The Navier-Stokes equation, one of the unsolved millennium prize problems, describes the motion of fluids (Fig. 1.7). The equation, in general, is nothing but Newton's second law, force equals to mass by acceleration, and the conservation of mass. Yet, the full-theoretical solution of the equation is incomplete.

The left-hand side of the equation explains how the velocity of the fluid is changing over time. The first and second terms on the right-hand side are internal forces: the first term is the pressure gradient, and the second term is the stress

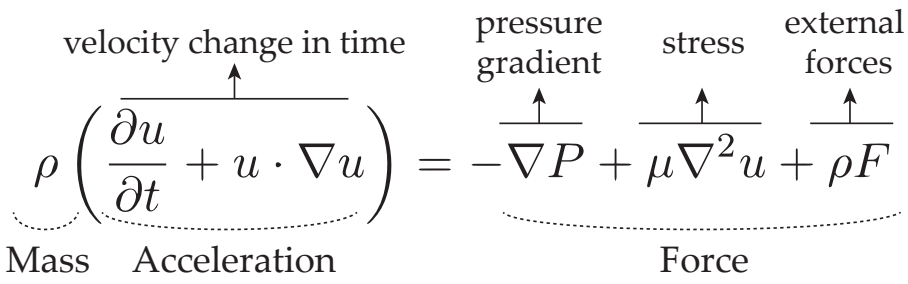


Figure 1.7: Navier-Stokes equation with captions for variables.

within the fluid. The third component on the right is the external forces applied to the system, such as gravitational forces, electrostatic forces, electromagnetic force, and any other. The variables in the equation ρ, t, u, P, μ, and F are the density of the fluid, time, velocity, pressure in the system, viscosity, and force, respectively. According to Navier-Stokes equation momentum is conserved, mass is conserved, and fluid is effected by three forces, pressure gradient, viscous forces, and gravity [35].

Ideally for the solution of Navier-Stokes, we consider the steady-state conditions; thus, the left-hand side of the equation, acceleration by time, is equal to zero. If there is no pressure gradient and no external force applied, the equation simplifies to equation 1.1, which gives the fluid behavior in cuvette flow.

$$0 = \mu\nabla^2 u \tag{1.1}$$

In most of the microfluidic systems, a pressure source is available to generate the fluid flow. If a pressure gradient is generated in a Poiseuille flow, then the pressure is not equal to zero. Flow is steady-state and unidirectional. Therefore, the Navier-Stokes equation simplifies to equation 1.2 for tubular or rectangular cross-section fluidic channels.

$$\nabla P = \mu\nabla^2 u \tag{1.2}$$

Integrating both sides of the equation and solving with boundary conditions in

Figure 1.8 (maximum velocity at $y = 0$ and zero velocity at $y = +h$ and $y = -h$), we find the mean velocity equation 1.3 dependent on viscosity, position in the y-axis, and pressure change in the x-axis.

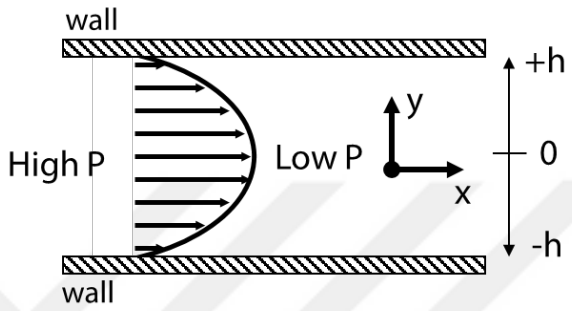


Figure 1.8: Poiseuille flow profile in two boundary system.

$$U_{mean} = \frac{1}{3\eta}\frac{\mathrm{d}P}{\mathrm{d}x}(-h^2) \tag{1.3}$$

The volumetric flow rate (Q) is equal to the velocity by cross-section. Thus, if we iterate the equation 1.3 to mean velocity into for cylindrical duct $A = \pi r^2$, we find one of the fundamental physical laws of fluids, Hagen-Poiseuille law, which gives the pressure drop for the streaming fluid in a laminar flow across a cylindrical duct.

$$\Delta P = Q\frac{8\eta L}{\pi r^4} \tag{1.4}$$

$$R_h = \frac{8\eta L}{\pi r^4} \tag{1.5}$$

In Equation 1.5 hydrodynamic resistance R_h, is defined for the cylindrical duct. hydrodynamic resistance is the proportionality factor and varies with the microchannel geometry. It is a necessary constant to calculate before designing and characterizing different microchannel geometries.

The rectangular cross section is the most common geometry in microchannels,

and hydrodynamic resistance for rectangular cross section channels is calculated with an asymptotic approximation as the following [52];

$$R_h = \frac{12\eta L}{wh^3}\left[1 - \frac{h}{w}\left(\frac{192}{\pi^5}\sum_{n=1}^{\infty}\frac{1}{(2n-1)^5}\tanh\left(\frac{2n-1}{2h}\pi w\right)\right)\right]^{-1} \tag{1.6}$$

$$R_h = \frac{12\eta L}{wh^3}\frac{1}{1-0.63(h/w)} \tag{1.7}$$

The Equation 1.6 simplifies to equation 1.7. When $w >> h$ we reach the minimum error rate which is around 1-2%.

Hagen-Poiseuille law $\Delta P = Q \times R_h$ represents the hydrodynamic analogy to electronic circuits with Ohm's law $\Delta V = I \times R$. The analogy allows us to model complex microfluidic channel geometries with electrical resistors, pressure pump as a voltage source, and a syringe pump as a current source.

Various physical phenomena cooperate within the microfluidic system. Dimensionless numbers give the ratio of these competing phenomena and provide a sense of simple comparison for different systems. We will discuss about flow behavior and dimensionless numbers in the following section.

1.2.5 Flow behavior and viscoelasticity

Rheology studies the flow behavior of viscous and solid samples under applied shear. In our study, experiments performed with ideally viscous DI water and viscoelastic fluids like dilute polymer solutions. Therefore it is essential to understand the physical background of the flow behavior of fluids. Rheometers measure the rheological properties of the materials. Rheometers are equipped with different measurement systems such as concentric cylinder, parallel plate, cone-and-plate, Money/Ewart and some special measuring devices [53].

In rheological measurement using two parallel plates system is illustrated in Figure 1.9.a. Sample fluid moves in between two, rotary top and stationary

bottom, plates 1.9.b. Top plate applies the shear while its surface area A is in contact with the sample. Then applied shear generates a set of motion by force (F) and results with velocity (V) difference varying from the maximum at the boundary of rotating plate and minimum (v=0) at the boundary of bottom plate. Shear is observed as shear stress $\tau = F/A$. We define a gap between two plates as shear gap, h. Shear rate,$\dot{\gamma} = v/h$, is the consequences of shear stress due to the viscosity of the sample. Flow is generated under laminar flow conditions. Laminar flow can be understood as a flow of planar fluid layers (Figure 1.9.c). For an ideally viscous flow behavior in laminar flow, velocity change in between two plates is linear; thus, the shear rate is constant.

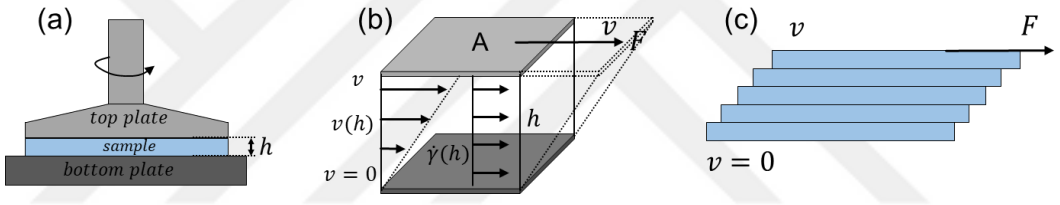


Figure 1.9: Illustration of (a) parallel plate system, (b) two parallel plates model represents shear and velocity change, and (c) Laminar flow distribution.

Viscosity is defined as the resistance of flow to the applied shear and it is a distinct property for the materials. The ratio of shear stress to the shear rate gives the shear viscosity ($\eta = \tau/\dot{\gamma}$). Ideally viscous flow is modeled with a dashpot model (Figure 1.10.a). Sample continuously deforms under a constant force. If the applied force is removed, deformation is permanent and shape does not recover to the initial state.

Ideally elastic behavior is explained using spring model (Figure 1.10.b). When stress or load applied to an ideal spring, it deforms temporarily to an extent. Immediately after releasing the force, spring recovers back to its original shape. This kind of deformation is called elastic deformation. The deformation energy is stored as elastic deformation. When stress released material returns back to initial shape (if the deformation is in the elastic range), energy recovered without any loss. If applied force causes deformation exceeding the elastic range, permanent deformation is observed with brittle fracture [53]. In the case of ideal viscous behavior, deformation is not recovered even after releasing the stress due to energy

loss. Viscoelastic materials show both elastic and viscous behavior at the same time. A good example of solid viscoelastic behavior is bouncy putty. When it is exposed to immediate stress, it bounces from the flat surfaces like an elastic ball; however, if putty rest on a flat surface while exposed to prolonged and time-dependent stress like gravity, it starts to show viscous behavior and turn into a flat uniform disc.

According to the Maxwell model, viscoelastic behavior is modeled using a dashpot connected to a spring (Figure 1.10.c). Viscoelastic materials show time-dependent response when stress applied or released. When loading the force as applied stress to the viscoelastic material, we observe immediate elastic deformation from the spring while the dashpot deforms in time. As a result, we observe time-dependent response on the deformation when stress applied. When stress released spring recoils to initial state completely with no delay; however, deformation in dashpot is unchanged.

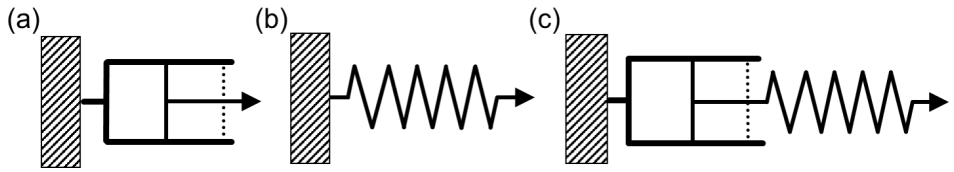


Figure 1.10: Illustration of models. (a) Ideally viscous behavior with dashpot model, (b) ideally elastic behavior with spring model, and (c) viscoelastic model with spring and dashpot Maxwell model.

Viscoelastic fluids are prepared by dissolving biological or synthetic polymeric substances in Newtonian solvents. Viscoelastic fluids show different non-Newtonian effects in practice. Die swelling effect, Weissenberg effect, and tack and stringiness. When viscoelastic solution extruded from the opening of an extruder it swells out from the exit. Such behavior is not observed in Newtonian solutions. It is due to the stress difference between inside and outside of the extruder. Viscoelastic polymers in solution align along the stress in extruder; however, the stress is lower at the exit of extruder. Therefore viscoelastic solution turns to initial conditions and swells. Weissenberg effect is also called rod-climbing effect. If viscoelastic solution stirred, solution starts to accumulate

on the stirring rod. This effect is observed mostly in highly concentrated polymeric solutions. Tack and stinginess is observed during coating processes, as the formation of long filaments under applied shear.

Polymeric solutions show a shear-thinning behavior and their viscosity decreases by increasing shear rate (increasing load) due to polymeric rearrangements. Imagine, polymers dissolved in solution similar size to high aspect ratio human hairs. One hair has a thickness of 100 µm and length of 200 mm, and a roll of hairs can easily entangle with each other at the state of rest (zero shear). They form a spherical shape coil structure so called entangled. It would be impossible to disentangle the hairs without a hair comb. Under an applied shear, molecules (hairs in our example) are oriented along the shear and disentangle to an extent (fully for dilute solutions). Such alignment reduces the coil structure to a more planar shape and decreases the resistance, means viscosity. Shear viscosity of shear-thinning solutions shows three regions: zero-shear viscosity (η_0), shear-rate dependent viscosity ($\eta = f(\dot{\gamma})$) and infinite-shear viscosity (η_∞) as given in Figure 1.11.a. Zero- and infinite-shear viscosity regions show plateau formations. Such formations are dependent on the dissolved polymer concentration c in solution (Figure 1.11.b). To see entanglement behaviour c should be higher than overlapping (in some terminology critical concentration) concentration (c^*). c/c^* defines the dilute to semi-dilute crossover regime of polymer solutions. In dilute solutions, c is substantially lower than c^*, ($c/c^* < 1$) and the solution shows no effective entanglement with ideal viscous flow behavior. The viscoelastic solution is considered to be semi-dilute if $c^* \geq c^*$, where polymer coils start to overlap, and entanglement behavior occurs [53, 54]. If $c/c^* > 1$, high entanglement behavior; thus zero shear viscosity appears in low shear rate. Very similar to concentration dependence, entanglement and shear-thinning behavior is also dependent on average molecular weight (M) of polymers (Figure 1.11.c). High molecular weight means large molecules are apparent in the solutions and entanglement may occur due to high molecular weight. Low molecular weight solutions show almost ideal viscous behavior.

Shear-thickening is another form of shear dependent viscosity change observed in polymeric solutions. Viscosity of shear thickening material increases in parallel

with the increasing shear rate. Shear thickening is dependent on the volume of free space between molecules. When shear stress applied to highly condensed suspensions, particles may come to closer contact each others which results with increased flow resistance. It is important to note that flow induced instabilities due to turbulent flow at high shear rates may generate false shear thickening flow behavior and mislead the shear viscosity measurement. This should be taken into consideration for low viscous solutions.

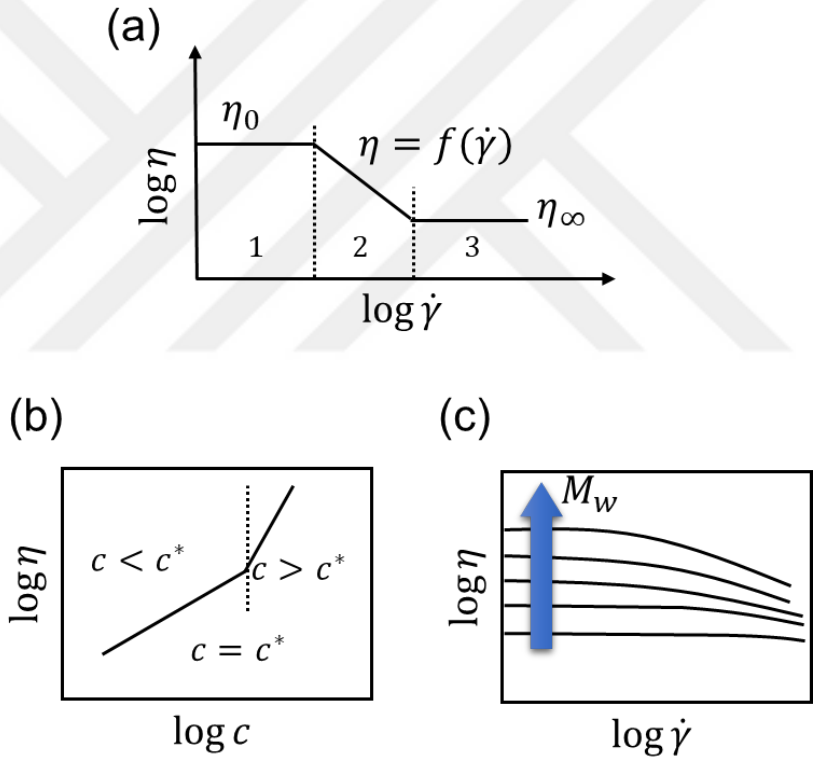


Figure 1.11: Illustration of shear thinning profiles. (a) Viscosity change for dense polymeric solution, (b) dependence of polymer concentration, and (c) molecular weight on shear viscosity.

Rheometers are used to study fluid behavior with measuring rheological data of the sample. Rheological properties are measured either on rotational or oscillatory measurement. Rotational rheometers use a rotary head, which is equiped with optical encoder to detect the torque, rotational speed, and deflection angle. Sample to be measured placed in between rotary up and fixed bottom plates. Then continuous shear is applied to the sample with a fixed or variable torque

and speed. Immediately after rotary plate starts to rotate, sample applies resistance to the shear due to its viscosity. Then the deflection angle is detected by the encoder which is an indication of rheological parameters. Rheometers work on two modes to detect different rheological parameters: Controlled shear stress (CSS) and controlled shear rate (CSR). As the name indicates, on CSR mode shear rate is preset by the rheometer and shear stress is measured. For the CSS mode, shear stress, and torque are predefined and shear rate is measured. Rotational tests are not useful for the gel-like samples since measurements have to be performed without permanent material change. In this case oscillatory measurements are preferred. In oscillatory test, rotary head applies a sinusoidal oscillation to the sample and measurement performed.

Time-dependent shear rate ramp response of ideally viscous, shear thinning, and shear thickening fluids is illustrated in Figure 1.12.

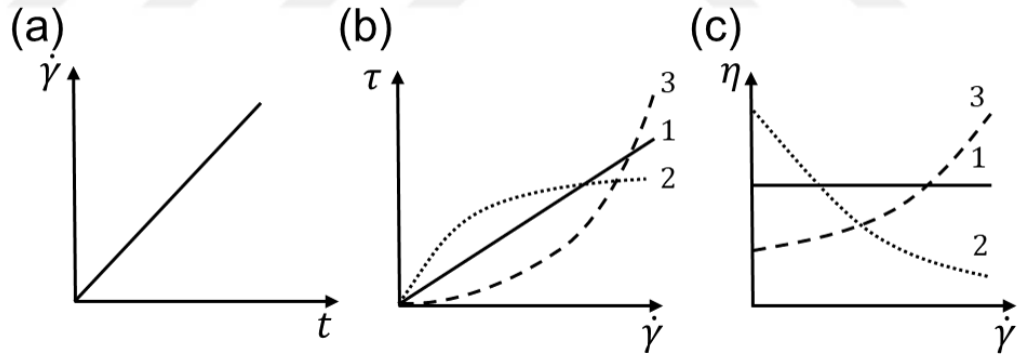


Figure 1.12: Flow profiles for different type of materials. (a) Time dependent shear rate ramping, (b) flow curves, and (c) viscosity functions of ideally viscous (1), shear thinning (2) and thickening (3) behavior.

1.2.5.1 Normal stresses

Normal stresses is clearly one of the most important phenomena in viscoelastic solutions and it is the main driving physics in viscoelastic particle migration concept. Normal stress is applied normal to the surface area. For non-Newtonian solutions the stresses on moving fluid are not isotropic. In Newtonian solutions deformation is the consequence of one dimensional stresses. In fact, deformation is always three dimensional with a 3x3 stress tensor for x direction (shear direction),

y direction (shear gradient direction) and z direction (neutral direction) (Figure 1.13) [53].

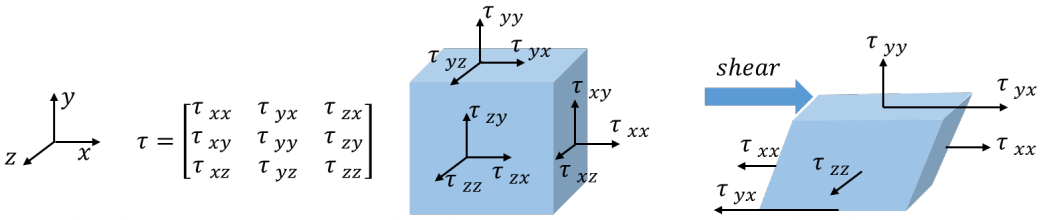


Figure 1.13: Illustration of stress tensor and stress components in x, y, and z directions.

Diagonal components in stress tensor are normal stresses which represent the direction of the stress and the deformation are perpendicular to the stress-applied surface. If stress is applied in x-axis direction, (τ_{xx}) it is the highest normal stress tensor due to related deformation in that direction. Off-diagonal components are shear stresses and reduces to one (τ_{yx}) for a flow in x direction. It is expected to observe deformation with the stresses perpendicular to the shear plane. In this case two normal stress difference is defined as,

$$N_1 = \tau_{xx} - \tau_{yy} \tag{1.8}$$

$$N_2 = \tau_{yy} - \tau_{zz} \tag{1.9}$$

Since (τ_{xx}) is greater compared to two other normal stresses N_1 gives higher result compared to N_2. N_3 is also considered for some studies and it is defined as $\tau_{xx} - \tau_{zz}$. For ideal viscous Newtonian solutions normal stress differences are zero. However, viscoelastic solutions show elastic behavior induced from microscopic polymeric interaction which is the primary reason for normal stress differences. Normal stress differences attributed to molecular conformal changes observed under moderate shear settings [55].

1.2.5.2 Dimensionless numbers

Various physical phenomena cooperate within the microfluidic system. Dimensionless numbers give the ratio of these competing phenomena and provide simpler comparison for different systems. Here we note the dimensionless numbers only related to this thesis. Reynolds number (Re), characterizes the flow condition and is defined as the ratio of inertial to viscous force in flow:

$$Re = \frac{\rho v D_h}{\eta} \tag{1.10}$$

where ρ is the fluid density, v is the fluid velocity, and D_h is the hydraulic diameter, $D_h = (2wh)/(h+w)$ where h and w are the height and width of the channel, respectively.

The polymeric suspension in viscoelastic solutions, introduces an elastic behavior to the viscoelastic fluid. Dimensionless Weissenberg number (Wi) describes the relation of elastic and viscous forces:

$$Wi = \lambda\dot{\gamma} = \frac{2\lambda Q}{hw^2} \tag{1.11}$$

where, λ is the relaxation time of the fluid, $\dot{\gamma}$ is the characteristic shear rate, and Q is the volumetric flow rate. The fluid elasticity is characterized by the competition between Re and Wi. The elasticity number, El, is defined as,

$$El = \frac{Re}{Wi} \tag{1.12}$$

To calculate flow parameters in microfluidic channels together with the dimensionless numbers hydrodynamic resistance R_h (equation 1.7), shear viscosity η should be known or calculated. Then volumetric flow rate is calculated using Hagen-Poiseuille equation. Estimation of the shear rate is possible using the wall shear rate relation;

$$\dot{\gamma}_w = \frac{6Q}{wh^2} \tag{1.13}$$

Average flow and particle velocity are calculated with $U_P = Q/(wh)$ equation after finding the volumetric flow rate.

1.3 Particle focusing in microfluidic flow cytometry applications

Precise particle focusing is critical for a variety of biological and chemical microfluidic applications. In the field of flow cytometry, suspended particles aligned along the centerline of a conduit is necessary to achieve high signal repeatability and low coefficient of variation (CV).

Sheath flow supported hydrodynamic particle focusing [6, 47, 56–58], is the most common method due to the ability to focus the particles at wide size variation. Sheath flow is injected together with the sample flow to the channel. Sheath flow is injected with a slightly higher pressure than the sample flow. Thus, the particles in the sample solution are hydrodynamically aligned to a single file. The drawback of such systems is the use of high volume of sheath fluid, two or more ports for fluid injections (one for sample the other for sheath fluid), size limitations (minimum detectable particle size >500 nm), and precise fabrication steps to enable perfect symmetric center alignment. Some methods perform particle focusing by an external force (-phoresis). Dielectrophoresis [59, 60], is based on the electrophoretic force with an applied electric field (AC or DC) using microfabricated electrodes. Magnetophoresis [61] technique based on an interaction of particles with the magnetic field. In the acoustophoresis technique, standing acoustic waves are generated using piezotransducers (PZTs). When particles interact with standing acoustic waves, they intend to move nodal points and focus to a single file [62–64]. The use and implementation of external force into flow cytometers increase the complexity of fabrication and operation.

Inertial and viscoelastic focusing techniques are sheathless and passive methods

with a single inlet/outlet chip. They generate flow-induced lift forces to provide passive manipulation of particles with less effort and are advantageous by far over externally applied forces in terms of cost and simplicity. Therefore as one the motivation in this thesis to support particle migration using a passive particle focusing technique.

Initially when we explain Navier-Stokes equation, we ignore the inertia of the fluid thus we considered $Re = 0$ in Stokes flow regime with Laminar flow. However, when we increase Re to the values enough to support Laminar flow but contributes significant inertia ($1 < Re < 100$), we observe nonlinear and time-irreversible motions for fluid and suspended particles [65]. In a microchannel a Poiseuille flow distribution generates a quadratic velocity profile. Suspended particle is under the influence of this velocity profile in laminar flow conditions Figure 1.14. However, at significant flow velocities we start to observe deterministic lateral migration perpendicular to the main flow produced by the lift forces.

In 1962, Segre and Silberbeg observed lateral migration of millimeter size spherical beads in a flow introduced to centimeter sized pipe. It is understood that, particles are under influence of two or more opposing lift forces since the particle equilibrium positions were stable somewhere in the mid of the cross section, 0.6 times the radius of 1cm diameter pipe. More studies show that, there are two dominating and opposing forces shear gradient lift and wall lift forces. These forces gave rise to a new field, inertial microfluidics. If a neutrally buoyant arbitrarily positioned particle is considered to be stationary relative to the fluid velocity, it experiences different velocity magnitudes due to the shear gradient in the channel (Figure 1.14). The velocity difference around the particle generates shear gradient lift force, which pushes the particle to low velocity, high shear rate regions (channel walls). The interaction between the particle and adjacent walls gives rise the another dominant force, wall lift force which pushes the particles away from walls when particles get proximity to the channel walls. Inertial lift scales with equation 1.14 and has a strong dependence of particle size.

$$F_L \sim \frac{\rho U^2 a^4}{H^2} \tag{1.14}$$

where F_L, ρ, U, a, and H is the dimensionless lift coefficient, fluid density, flow velocity, particle diameter and channel dimensions, respectively. Net inertial lift force is found to be equation 1.15 near the channel center and equation 1.15 near the channel wall

$$F_L \sim \frac{\rho U^2 a^3}{H} \tag{1.15}$$

$$F_L \sim \frac{\rho U^2 a^6}{H^4} \tag{1.16}$$

holds for particle size ratio $0.05 < a/H < 0.2$ and $20 < Re < 80$ [65].

In addition to dominant lift forces, weak lift forces are available in Poiseuille flow as well. In 1965 Saffman described slip-shear lift (Saffman lift) as a consequence of velocity change at the existence of bounded flow. If the particle velocity magnitude is different than the fluid velocity, either faster or slower than the fluid, particle tends to migrate towards the channel center or walls [66]. Saffman lift is a weak inertial effect; however, if an extra force is introduced to the flow (electrical, gravitational or magnetic), it can become dominating lift force effecting the equilibrium position of the particles [65]. Slip-spin is another form of weak inertial lift force explains induced lift force to a rotating sphere in an unbounded flow [67, 68]. Slip-shear lift requires velocity difference and slip-spin requires rotation differences between spherical particle and flow. In Poiseuille rotation-slip lift directs the particle towards the channel center.

Inertial focusing is achieved in various shaped geometry channels (rectangular [69–71], square [72], circular [73], and 3D spiral [74, 75]. However, single train of particles is only possible with additional forces either by dean-drag force in curved channels [76, 77] and sheath flow or externally applied forces. Inertial focusing systems require high flow rates and complex microchannel geometries

[78] to obtain a single train of particles, which is considered as a bottleneck for cytometry implementations due to faster signal processing requirements and fabrication difficulties [79].

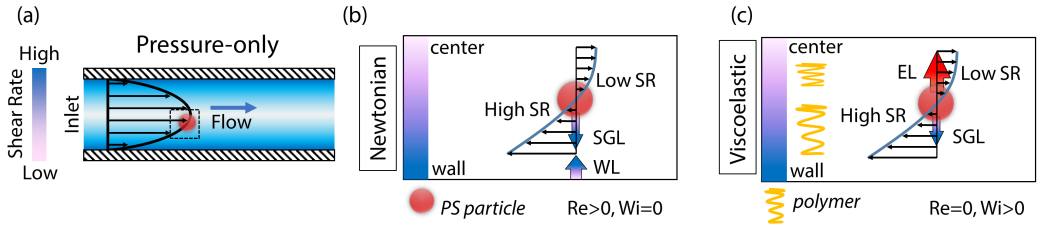


Figure 1.14: Particle migration in Newtonian and viscoelastic solution. (a) Poiseuille flow distribution, (b) Newtonian solution, and (c) viscoelastic solution

Viscoelastic focusing method uses rheological properties of the sample solutions. Thus, the particle focusing is more dependent on fluid properties rather than the flow conditions and channel geometries. Some recent review articles cover the viscoelastic focusing theory, device implementations, application fields, and future aspects [80,81]. In viscoelastic solutions, elastic lift force is exerted on the suspended particles due to non-uniform normal stress differences [68] (τ_{xx}, τ_{yy}, and τ_{zz} are different from each others) the elastic behavior of dissolved synthetic or biological polymers in Newtonian solutions. In a Poiseuille flow, dissolved viscoelastic polymers are stretched along with the applied shear. The shear gradient in the channel causes a non-uniform stretching of polymers, which increases at a high shear rate (Figure 1.14). Non-uniform polymer stretching due to non-uniform normal stress differences (N_1 and N_2) generates an elastic lift force on the suspended particles directing from high shear rate to low shear rate regions, from the channel walls to the center [82]. At low Re, shear gradient lift force is negligible compared to elastic lift force. Thus, the particle is attracted to the channel center under the pressure-only condition (Figure 1.14). For dilute polymeric solutions N_2 is mostly neglected (τ_{yy} almost equal to τ_{zz}) and elastic lift force F_E shows direct dependence on N_1 in equation 1.17.

$$F_E \sim a^3 \nabla N_1 = a^3(\nabla \tau_{xx} - \nabla \tau_{yy}) \tag{1.17}$$

Particles equilibrium positions depend on rheological properties of the fluid (dilute or highly shear thinning/thickening), Reynolds number, Elasticity number, and particle to channel size ration (a/H). By tuning the rheological properties of the non-Newtonian fluids and flow conditions, it is possible to reach a single train of particles [83–87] at the channel center. Unlike inertial microfluidics, viscoelastic fluids can manipulate particles even at low flow rates (on the order of µl/h). When elastic lift force is accompanied by inertial lift force, referred to elasto-inertial or inertio-elastic focusing [88], it supports focusing at high flow rates up to ml/s [71, 74, 79, 89–91].

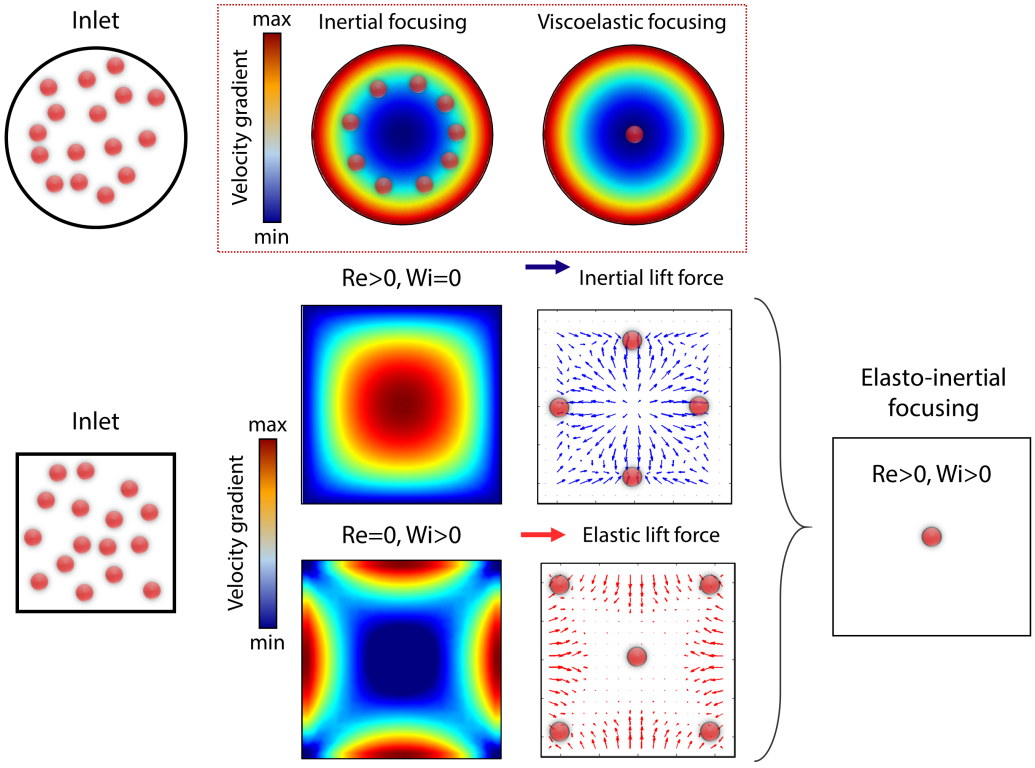


Figure 1.15: Illustration of dominant force gradient, force arrow-field, and equilibrium particle positions for both inertial and viscoelastic focusing in circular and square cross section channel profiles

Viscoelastic and elasto-inertial focusing have been investigated for different synthetic and biological particles such as polystyrene beads (PS), blood cells [88, 92–96], MCF-7 cells [97], sperm cells [98], Jurkat cells [99], and bacteria [79,97,100,101]. Equilibrium positions of particles in different channel geometries

given in Figure 1.15 for inertial focusing, viscoelastic focusing and elasto-inertial focusing.

1.4 Thesis Outline

The motivation of this thesis can be grouped into two sections.

- Development of a viscoelastic focusing technique for microfluidic flow cytometry applications to provide integrated, portable, and cost-efficient flow cytometry systems available for low resource settings.

The aim is to integrate a recently trending viscoelastic particle migration technique to microfluidic flow cytometry systems. The significance of this study is using the benefits of microfluidics and viscoelastic focusing in terms of passive particle migration and 3D flow focusing by only controlling the flow conditions and rheological properties of the biocompatible carrier fluid to provide integrated flow cytometry systems. The innovation in this study is that there is, to date, no study that fully demonstrates a characterized viscoelastic solutions with the optimized flow conditions to be able to work with optical-, impedance- and imaging-based flow cytometry applications.

- Develop a unifying explanation for viscoelastic particle migration under pressure-driven flow and electric field for Newtonian and non-Newtonian solutions.

The aim is to create a fundamental understanding of how and why the suspended particles migrate in Newtonian, neutral viscoelastic, and polyelectrolyte fluids under the influence of both pressure-driven-flow and DC electric field in a microchannel. We developed a unifying theory, Electro-Viscoelastic Migration (EVM), which addresses the studies in microfluidic particle focusing and electrophoresis communities to understand the reason of anomalous particle migration behavior in viscoelastic solutions under various flow conditions. The significance of this study shows that EVM theory is highly capable of creating different particle equilibrium states and non-uniform concentration gradient in

charged viscoelastic solutions by only tuning the rheological properties and electrical charge of the particles or fluids. Our main hypothesis is that mutual application of pressure-driven flow and DC electric filed generates non-uniform polymer concentration at the microchannel cross section for polyelectrolytes due to polymer charge; however, polymer concentration stays uniform for neutral polymers. The innovation in this study is multifold. There is no study, to date, reporting non-uniform concentration gradient in viscoelastic solutions at the lateral cross section of the microchannel. It is possible to control the particle equilibrium positions by changing the direction of the electric field. EVM opens the way to a new phenomenon, 3D electrophoresis, such as fractionate and align the polymers at the channel center or walls based on their electrical charge and size. EVM provides better 3D viscoelastic focusing at a shorter distance in comparison to use of only pressure-driven-flow for flow cytometry applications using viscoelastic carrier fluids.

The organization of the rest of the chapters is given as the following:

In Chapter 2, we developed a fiber-based optical microflow cytometry system. We introduced viscoelastic flow focusing as a 3D particle focusing method in a flow cytometry application. We presented a novel fabrication method for flow cytometry with a glass capillary microchannel, and optical fibers are fixed on a palm-sized holder without any complex microfabrication necessity. We compared the particle focusing performance of the three most common viscoelastic solutions and demonstrated flow cytometry measurements with polystyrene calibration beads.

In Chapter 3, we developed an impedance-based three-electrode flow cytometry system on a PDMS microchannel on a glass substrate. We tuned the rheological and ionic properties of viscoelastic solutions to achieve elasto-inertial particle focusing for polystyrene beads and human red blood cells. We presented a reusable technique by replacing the PDMS layer for each measurement and protecting the glass electrode substrate to allow multiple uses. We showed that by tuning the flow conditions, it is possible to align non-spherical red blood cells to a single orientation, parachute shape, at the channel center to improve the cytometry

measurement performance.

In Chapter 4, we introduced a unification theory on electro-viscoelastic particle migration (EVM) in Newtonian, neutral and polyelectrolyte viscoelastic solutions under simultaneously used pressure-driven-flow and DC electric field in a microchannel. We observed bi-directional particle equilibrium states depending on the charge of the particle, rheological and electrical properties of the fluid, and magnitude and the direction of the electric field. We present that it is possible to generate non-uniform concentration gradient radially varying from center to the walls at the channel cross section using polyelectrolyte viscoelastic solutions. We also showed that simultaneous use pressure-driven-flow and DC electric field improves the performance of viscoelastic particle focusing at a shorter distance compared to the use of only pressure-driven-flow.

In Chapter 5, Concluding remarks about the thesis and discussion for the future directions are given.

Chapter 2

Optical-based microfluidic flow cytometry using viscoelastic fluids

(Part of this study was published as "Sheathless Microflow Cytometry Using Viscoelastic Fluids" Mohammad Asghari, Murat Serhatlioglu, Bülend Ortaç, Mehmet E Solmaz, and Caglar Elbuken, *Scientific Reports*, September 27, 2017, Reproduced (or 'Reproduced in part') from Ref. [102] with permission from Nature Publishing Group. https://doi.org/10.1038/s41598-017-12558-2)

2.1 Introduction

Optical flow cytometers have been around since the 1960s [103], and yet traditional flow cytometers are bulky, expensive, and require technical labor for maintenance and operation. Fortunately, microfluidics has addressed these challenges. Microfluidic optic flow cytometers mostly focus on miniaturization and advancements in flow cell design by integrating the optical components, thus lowering the required sample volume and cost while achieving portability.

Various strategies have been used for flow cytometers to achieve better optical interaction of the laser beam with the particles of interest. Aligned optical fibers [1,6,8,104–106], inscribed optical waveguides [47,107,108], and microfabricated customized lenses [109–113], were used in the optical interrogation region to obtain better light interaction with focused particles without using any free-space optics. Inscribing waveguides is a complicated fabrication process and brings further challenges such as alignment issues during the coupling of fiber optics, laser and detector sources. Instead, direct assembly of already coupled optical fibers provides mechanical stability, ease of alignment, and efficient light interaction with individual particles on an integrated chip. There are several examples of microfluidic optical flow cytometry, some of which are reprinted in Figure 2.1.

In this study we combine a fiber-based microfluidic cytometer device with a viscoelastic particle focusing technique to achieve a new sheathless microflow cytometer as schematically shown in Figure 2.2. To best of our knowledge, this is the first study presenting viscoelastic focusing in a microfluidic cytometry environment. We numerically compared the efficiency of particle focusing of three most commonly used viscoelastic solutions: Polyvinylpyrrolidone (PVP), Polyethylene Oxide (PEO), and hyaluronic acid (HA) and compared our results. Then, the optical detection system was developed by assembling a 15 cm-long capillary as the flow channel and three optical fibers to incorporate the laser light and to collect forward scatter (FSC), and side scatter (SSC) signals. Capillary and optical fibers are assembled and fixed on a palm-sized holder without any complex microfabrication necessity. Our results provide a comparison between three viscoelastic solutions on cytometry measurements of 6 µm diameter polystyrene calibration

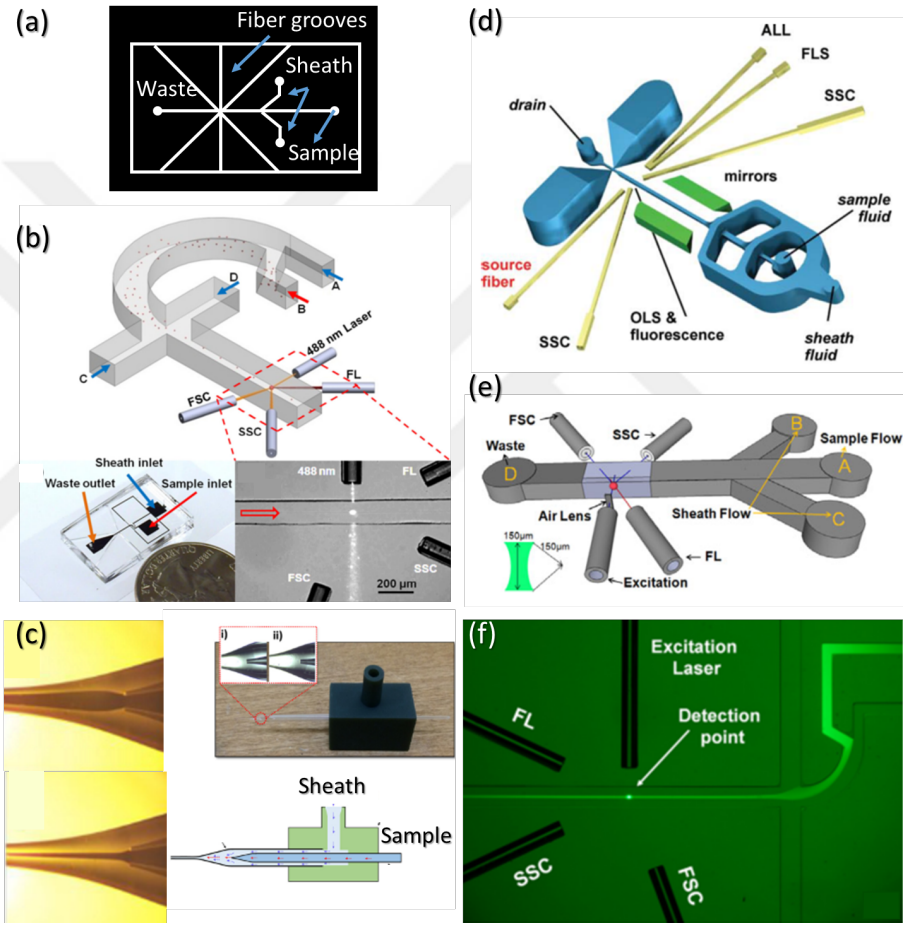


Figure 2.1: Schematic illustration of examples in the literatures for optical microfluidic flow cytometry studies. (a) Reproduced from Ref. [1] with permission from the American Chemical Society, (b) reproduced from Ref. [2] with permission from the American Institute of Physics, (c) reproduced from Ref. [3] with permission from the Elsevier, (d) reproduced from Ref. [4] with permission from the Wiley Online Library, (e) reproduced from Ref. [5] with permission from IEEE, and (f) reproduced from Ref. [6] with permission from American Institute of Physics.

beads. Our HA- and PEO-based cytometers are good candidates for using in optical cytometers with throughput yield over 750 events/s and 5.8% CV value.

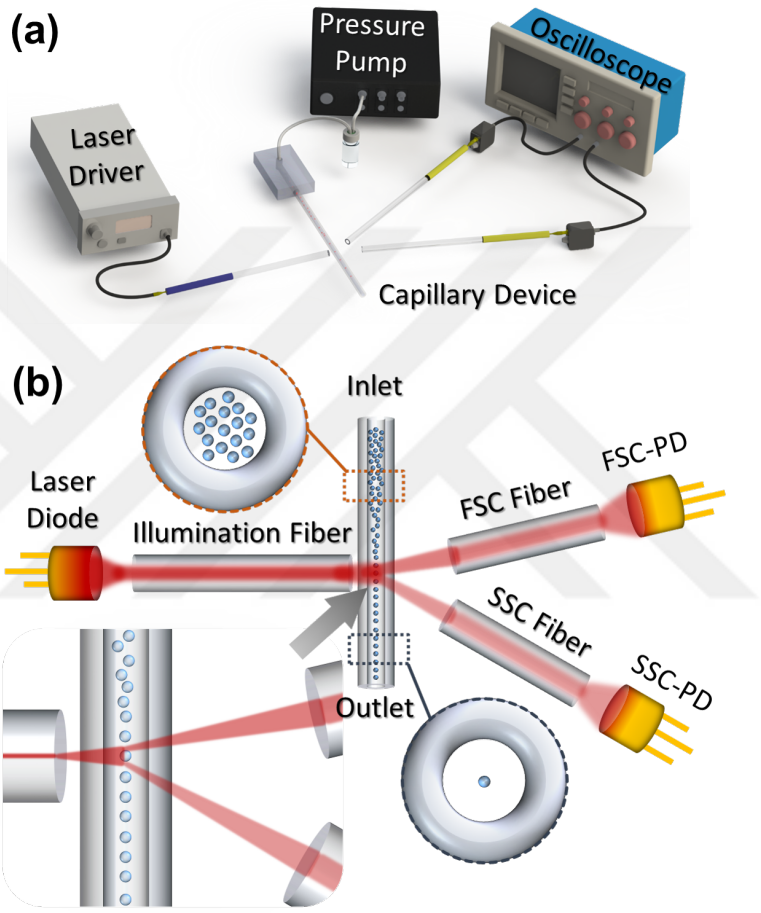


Figure 2.2: Schematic illustration of sheathless microfluidic flow cytometry setup. (a) Consisting of the assembled chip, a 635 nm laser diode, a laser driver, a pressure pump, an oscilloscope, and Si photodetectors. (b) Schematic illustration of assembled components (not to scale).

2.2 Materials and methods

2.2.1 Sample preparation

0.05% (w/v) PEO_{5MDa}, 8% (w/v) PVP_{40kDa}, and 0.5% (w/v) $HA_{1.06MDa}$ viscoelastic solutions were prepared in DI Water, and their shear viscosity was measured in rheometer (Anton Paar, MCR 301). 6 µm polystyrene (PS) beads

suspended in viscoelastic solutions at the concentration of 4 x 10^6 particles/ml.

2.2.2 Device fabrication

The microfluidic cytometry device consists of three parts: (I) Preparation of 15 cm long glass capillary tube, (II) a laser-cut polymethyl methacrylate (PMMA) holder, and (III) upright alignment and fixation of optical fibers to the capillary tube on PMMA holder.

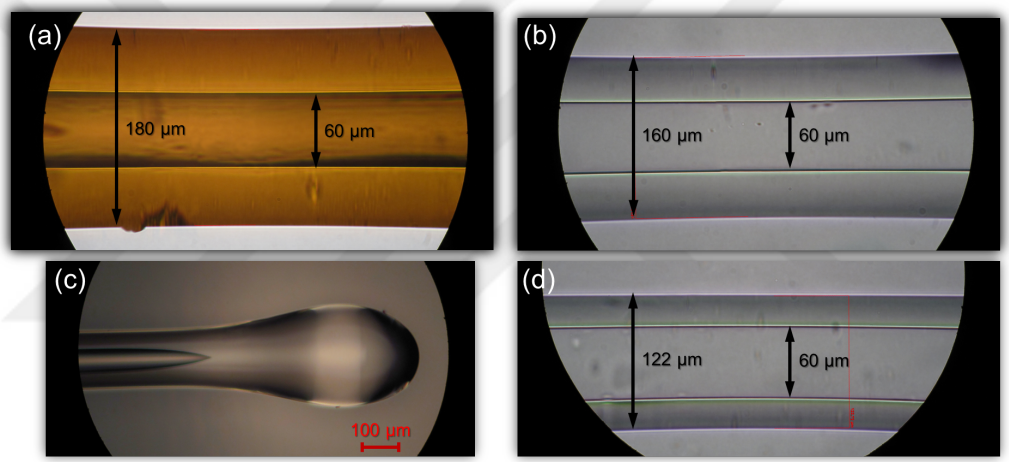


Figure 2.3: Preparation of capillary tube. (a) 160 µm O.D., 60 µm I.D. capillary tube with 10 µm polyamide coating. (b) Polyamide coating was removed in sulfuric acid. (c) Ball lens protection cap to isolate the inner channel. (d) Capillary tube after 20 minutes of HF etching.

(I) Figure 2.3 shows the fabrication steps capillary diameter adjustment. We used a capillary glass tube (Polymicro Technologies) with 180 µm (10 µm polyamide coating) outer diameter (O.D.), 60 µm inner diameter (I.D.) (Figure 2.3.a) and optical fibers with 125 µm of O.D. in flow cytometry setup. The diameter of the capillary tube was reduced to 122 µm in hydrofluoric acid solution (HF) to match the diameter of the optical fibers since 122 µm O.D. was unavailable. Initially, 10 µm polyamide coating of the capillary tube was stripped out in a 95% sulfuric acid solution at 90 °C for 2 min (Figure 2.3.b). Then, both ends of the capillary tube were melted to form a ball lens shape in a fusion splicer (Fujikura, FSM-100P) to protect the inside of the capillary during HF etching (Figure 2.3.c). 15 cm long capillary tube was placed in a 40% HF solution for

20 min, and O.D. was reduced to 122 µm (Figure 2.3.d). Later on, the ball lens ends of the capillary tube were clipped away. Finally, capillary tube ends were connected to Tygon tubing and sealed with PDMS.

(II) We carved guided grooves on a flat PMMA slab using CO_2 laser (Epilog Zing, 30W) for upright alignment and fixation the optical fibers and capillary microchannel (Figure 2.4.a).

(III) The cytometry device was finalized by assembling the capillary tube and the fibers and fixing them onto the PMMA holder using adhesive tape (Figure 2.4.b-d). The input fiber was placed perpendicularly at one side of the capillary tube to guide the light through the capillary tube. On the opposite side, two detection fibers were placed at an angle of 13° and 30° to the incident light to collect the FSC and SSC signals, respectively. FSC fiber was oriented at a small angle to avoid direct beam coupling from the light source [110].

2.2.3 Experimental setup

Illustrative drawing and the working principle of the experimental setup are given in Figure 2.2. We used a 635 nm laser source (Thorlabs, S1FC635) coupled to a single-mode optical fiber (core diameter 4.3 µm, cladding diameter 125 µm, Thorlabs, S405-XP). FSC and SSC collecting multi-mode optical fibers (core diameter 62.5 µm, cladding diameter 125 µm, Thorlabs, M42L01) were connected to two high-speed fiber-coupled photodetectors (Thorlabs, DET02AFC). Voltage signals from photodetectors were measured using an oscilloscope (Tektronix, MDO3104) at 500 kHz sampling rate. The signal was post-processed with MATLAB to acquire peak values and apply gating if necessary. Gating designates a homogeneous population with common specific properties and is a standard process in commercial flow cytometers.

Elveflow pressure pump was used to pump the particle suspensions through the capillary microchannel. We observed suspension flow under an inverted microscope (Omano, OMFL600) with a high-speed camera (Phantom Miro M310) to observe whether the particles are aligned to the capillary center (Figure 2.4.e).

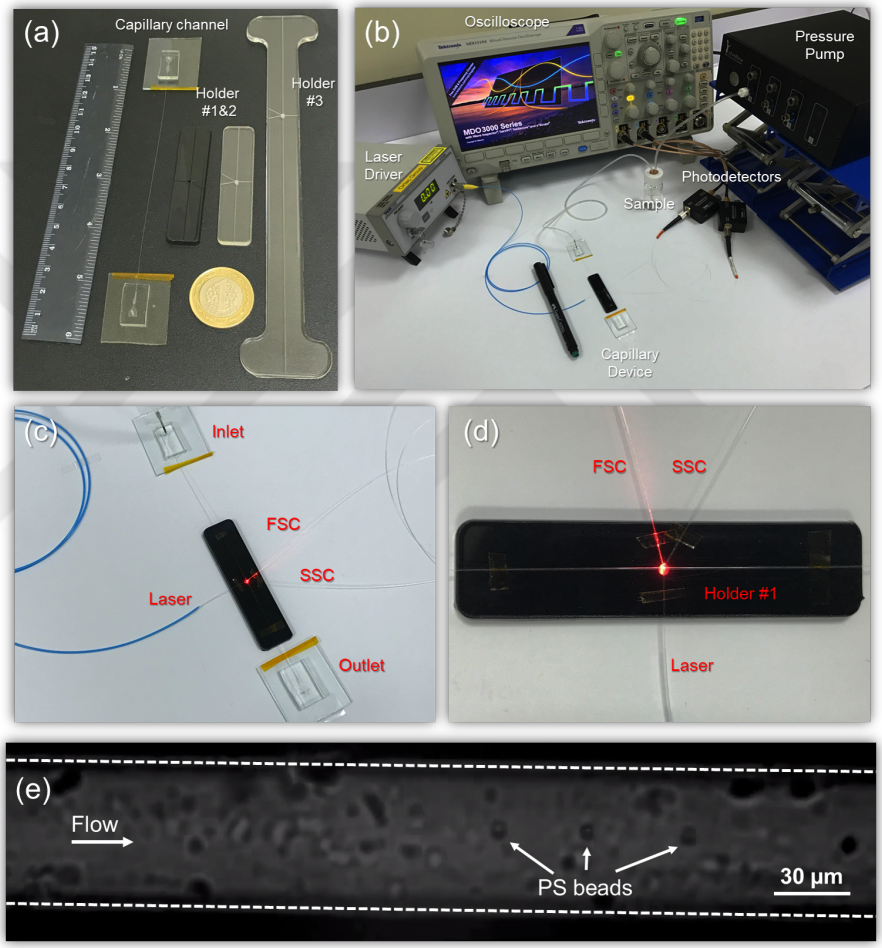


Figure 2.4: Viscoelastic microfluidic cytometry setup. (a) Capillary channel and PMMA holders (holders 1, 2, and 3) to assemble the capillary tube and optical fibers. (b) Overview of the experimental setup; capillary device, laser driver, oscilloscope, pressure pump, and photodetectors. (c) Closer look-up of viscoelastic microfluidic cytometry. An image during the experiment (d) showing the optical interrogation region (laser-on) and (e) particles inside the capillary tube (laser-off).

2.3 Results and discussion

2.3.1 Numerical results

Non-Newtonian viscoelastic solutions generate 3D particle focusing due to the elastic properties of the solutions. We explained the details of visoelastic focusing in Chapter 1. Here we briefly summarized for circular cross section microchannel. Under the Poiseuille flow, viscoelastic solutions generate normal stress difference N_1 and N_2. For dilute solutions (Boger fluids), N_2 is negligible. Thus the elastic lift force is dependent on particle radius and the gradient of first normal stress difference (equation 1.17). Pressure flow in the capillary generates shear gradient varying from the capillary walls to the center. Polymers are highly stretched near the capillary walls due to higher shear stress compared to the center. This stores higher elastic stress and generates elastic lift force varying from the capillary walls (high) to the center (low). Thus, due to the perfect symmetry of circular geometry, the suspended particles are formed a single train along the capillary center to reduce the elastic stress.

Rheological properties are crucially important for viscoelastic focusing. We analytically calculated the rheological parameters of the viscoelastic solutions. We defined a rheological term (Reo), empirically shows which solution can generate more efficient viscoelastic focusing. The rheological term (equation 2.1) relates the radial migration velocity of the suspended particles with the channel geometry and rheological properties of the solution [114, 115]. The summary of the calculations and rheological parameters are given in 2.1.

The rheological term is given in equation 2.1.

$$Reo = \frac{0.77\frac{c}{c^*}}{1+0.77\frac{c}{c^*}}\lambda \tag{2.1}$$

where c is the polymeric concentration, c^* is the overlapping polymer concentration, and λ is the relaxation time. Relaxation time is predicted using the Zimm relaxation theory for dilute solutions (equation 2.2).

$$\lambda_{zimm} = \frac{4\,\pi\,\eta_s\,R_g^3}{k_B\,T} \tag{2.2}$$

where η_s, R_g, k_B, T is the solvent viscosity (8.90×10^{-4} mPa.s), radius of gyration, Boltzmann constant, and temperature (298 °K). Here the radius of gyration for each polymer is found from the literature [116–118] as given in Table 2.1.

Overlapping polymer concentrations are calculated using Graessley's modified equation [119] (equation 2.3). The intrinsic viscosity of each solution is calculated using the references in the literature [117, 120, 121]. (equation 2.4-2.6).

$$c^* = \frac{0.77}{[\eta]} \tag{2.3}$$

$$[\eta]_{PVP} = 0.039\,M_w^{0.59} \tag{2.4}$$

$$[\eta]_{PEO} = 0.072\,M_w^{0.65} \tag{2.5}$$

$$[\eta]_{HA} = 0.032\,M_w^{0.78} \tag{2.6}$$

According to the calculated *Reo* parameters, it is expected to observe efficient device performance for PEO and HA-based viscoelastic solutions, while poor efficiency for PVP based viscoelastic solution. To validate our results, we performed experiments in the following section for microfluidic cytometry device.

2.3.2 Experimental results on cytometry performance

Our numerical results show that PEO- and HA-based viscoelastic solutions can support efficient viscoelastic focusing. We performed optical cytometry measurements with our palm-sized optical cytometry device. We measure forward and

Table 2.1: Rheological parameters for viscoelastic solutions.

Sample (MDa)	$[\eta]$ (ml/g)	c (mg/ml)	c^* (mg/ml)	R_g (nm)	λ_{eff} (ms)	Reo (ms)
$PVP_{0.04MDa}$	20	80	38	14.4	0.009	0.0056
$PEO_{5.0MDa}$	1628	0.5	0.47	155	11.38	5.11
$HA_{1.06MDa}$	1676	5	0.46	126	6.08	5.43

Table 2.2: Calculation of dimensionless numbers and experimental parameters for flow cytometry experiments.

Sample	P (mbar)	Q (µl/h)	Re	Wi	El
PVP	300	115	0.24	0.0034	0.014
PEO	500	205	0.45	7.63	16.9
HA	1000	127	0.11	2.5	23.2

side scattered light (FSC and SSC) signals and studied our results for three viscoelastic solutions in terms of %CV values.

We calculated the dimensionless numbers to define the experimental conditions for each viscoelastic solution, as provided in Table 2.2. Experiments performed at $Re < 1$ thus inertial effects are negligible. Particles are only under the effect of the elastic lift force.

Within the cytometry device, the distance between the illumination fiber and the capillary tube (30 µm) were adjusted to achieve 6 µm beam diameter to match the size of the focused particles at the capillary center. FSC and SSC collecting fibers were 405 µm and 330 µm away from the capillary tube. The distance from the capillary inlet to the optical interrogation point was set as 6 cm, which is obtained after observing the best particle focusing development distance under the microscope. The collected light was converted into a voltage signal using two Si photodetectors. FSC signal collects some portion of the incident light, which leads to a non-zero base value for each sample.

Figure 2.5 shows the collected data for 200 ms measurement duration together with the close-up views of 3 particle events in a 3 ms measurement window for

HA viscoelastic solution. The acquired signal for both FSC and SSC, corresponding to 750 events/s of throughput (throughput values are given in Table 2.3). In closer look-up to an arbitrary 3 ms region, we observe that the particles are well separated and have 1 ms of periodicity. The FSC and SSC signals are accumulated at a specific voltage level. Only nine events in the entire 200 ms time duration had signal values greater than the voltage level of highly focused particles. These events include aggregates, doublets, or triplets, yielding an increase in the measured signal. Similar data views also acquired for PEO and PVP results (long duration data is not represented here).

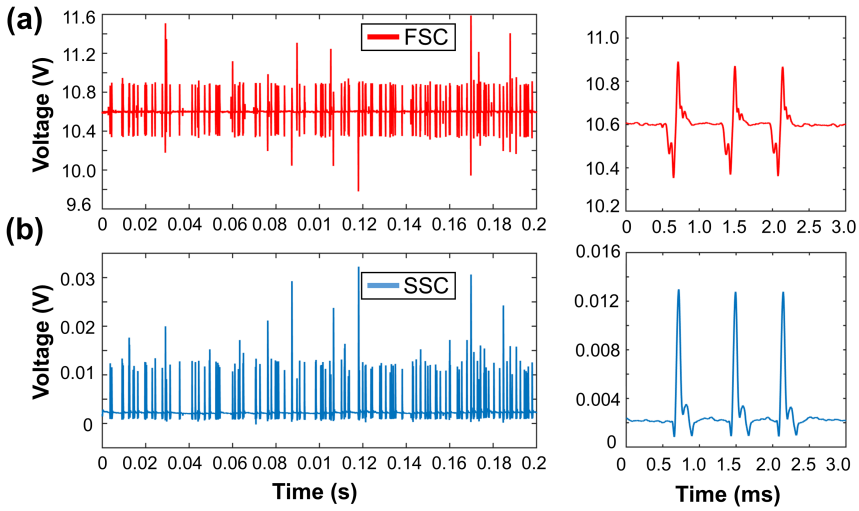


Figure 2.5: Viscoelastic microfluidic cytometry results of FSC and SSC signals in HA-based viscoelastic solution for 6 µm diameter polystyrene beads (a) 200 ms and (b) 3 ms closer look-up.

Figure 2.6, 2.7, and 2.8 represent 1 s FSC and SSC signals obtained from HA-, PEO-, and PVP-based viscoelastic cytometry measurements. Scatter plots of FSC vs SSC are given in Figure 2.6.a, 2.7.a, and 2.8.a using FSC signal baseline reduction. Histograms, together with the CV values, are plotted in Figure 2.6.b and 2.7.b with rectangular gating, and Figure 2.8.b without gating for HA, PEO, and PVP samples, respectively. The results of the signal mean, standard deviation (S.D.), and %CV are summarized in Table 2.3 for cytometry measurements.

Figure 2.6.a depicts the scatter plot of events collected for 1 s time duration

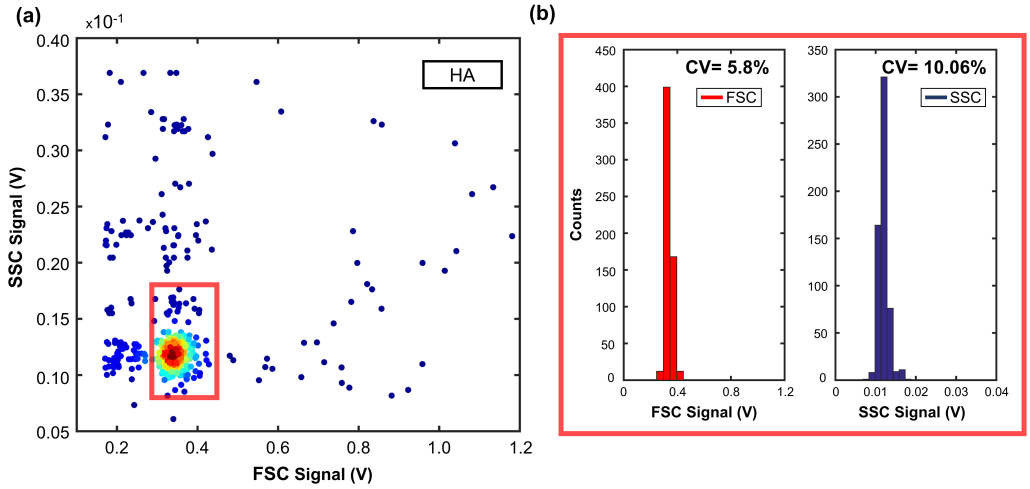


Figure 2.6: HA-based viscoelastic flow cytometry results for 6 µm diameter polystyrene beads. (a) Scatter plot of FSC vs. SSC events and (b) Histograms of FSC and SSC signals.

for the HA experiment. Most of these counts are populated into a small region. A rectangular gating window removes the statistical outliers and includes more than 80% of the events, was used to isolate doublets, triplets, and clumps. Figure 2.6.b shows the histogram plots of the signal peaks within the gating region, and the CV values were calculated as 5.8% and 10.06% for FSC and SSC signals, respectively.

Figure 2.7.a represents the signals obtained using the PEO solution. The peaks are accumulated at 4.8 V for FSC and 0.016 V for SSC. Most of these counted events are populated into a small region; however, clumps are widely spread compared to the HA solution, as seen in Figure 2.7.b. The standard deviation, mean, and CV values of 6.33% and 10.17% intensity events were obtained for FSC and SSC, respectively. The throughput was obtained as 780 events/s.

For PVP solution, throughput was obtained as 200 events/s since we used a lower flow rate compared to other measurements. In Figure 2.8.a, FSC vs SSC plot has mainly three accumulated regions. Weak 3D focusing performance of PVP causes fleeing particles, passing through the focused region without or

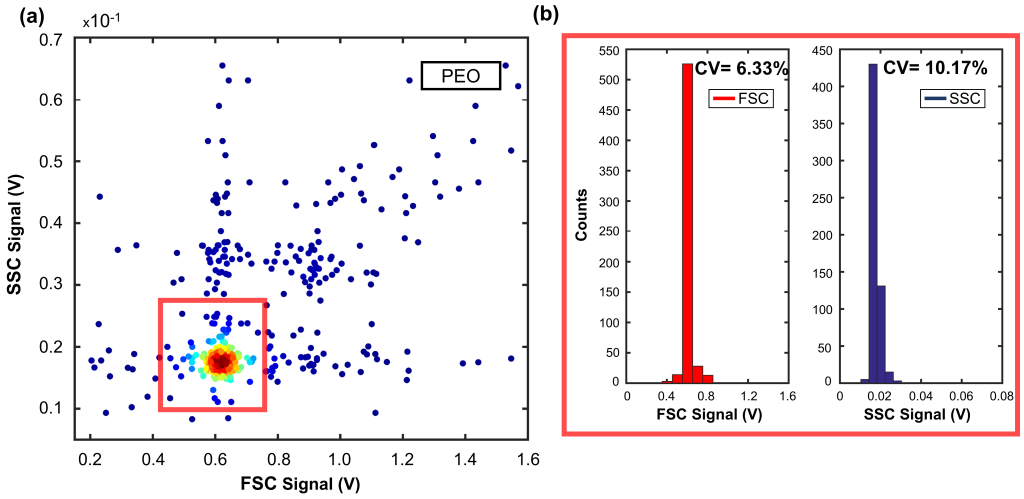


Figure 2.7: PEO based viscoelastic flow cytometry results. (a) Scatter plot of FSC to SSC events and (b) Histograms of FSC and SSC signals.

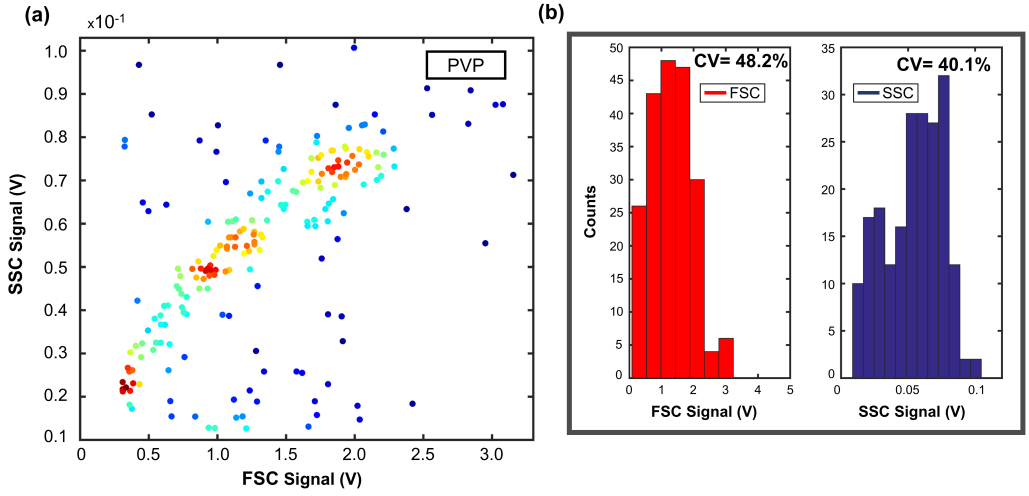


Figure 2.8: PVP based viscoelastic flow cytometry results (a) Scatter plot of FSC to SSC events and (b) Histograms of FSC and SSC signals without gating.

Table 2.3: Flow cytometry results: mean value, standard deviation, and coefficient of variation (%CV).

	Mean (V)		S.D. (V)		%CV	
Sample	FSC	SSC	FSC	SSC	FSC	SSC
HA	0.340	0.012	0.020	0.001	5.80	10.06
PEO	0.620	0.017	0.039	0.002	6.33	10.17
PVP	1.322	0.054	0.638	0.021	48.24	40.10

Table 2.4: Comparison of HA-based sheathless microfluidic cytometry (HA-MFC) and commercial BD Accuri D6 flow cytometry for 6 µm particles.

Definitions	BD Accuri D6	HA-MFC
Throughput	240 (events/s)	780 (events/s)
Gating	88%	80%
%CV FSC	3.5%	5.8%
%CV SSC	13%	10%

weakly encountering with the illumination laser light. Detected beads show significant signal variation and disrupted periodicity. There is no distinct boundary on counts for the PVP sample. The low FSC signal region is due to fleeing particles and corresponds to most of the events. The rest of the events are widely spread in the scatter plot. Compared to the results obtained using PEO and HA solutions that are densely populated in the region of 0.3-0.7V FSC and 0.01-0.02V SSC, PVP events are very scarce in this region. Therefore, we conclude that the focusing of the particles is unsuccessful using the PVP solution due to low rheological properties. This argument coincides with our numerical results.

In the comparison of flow cytometry device performances, HA- and PEO-based flow cytometry devices were successful by far compared to PVP-based flow cytometry. Compared to PEO, we measured slightly lower %CV values for HA-based flow cytometry.

We compared our HA microfluidic cytometry results with commercial flow cytometry, BD Accuri C6. The manufacturer data for 6 µm polystyrene calibration beads are given as 2% CV. BD Accuri C6 was calibrated before the experiment and gave a result of 3.5% CV for the FSC signal and 13% CV for the SSC signal

with similar gating using 6 µm polystyrene particles suspended in DI water. Our HA-based flow cytometry gives 5.8% CV for FSC signal and 10.06% CV for SSC signal for the same particles. A detailed comparison between the two systems is given in Table 2.4. It can be seen that similar results are obtained from the two systems. A figure of merit for comparison of flow cytometers is the CV values, which are mostly obtained using PS calibration particles. Despite the variation in the size of test particles, or the measurement modes (forward scatter, side scatter or fluorescent detection), CV values provide a common ground for a comparison of different measurement systems. For the evaluation of our viscoelastic cytometry device (HA-MFC), a comparison of the CV values reported for previously demonstrated microfluidic cytometers is given in Figure 2.9.

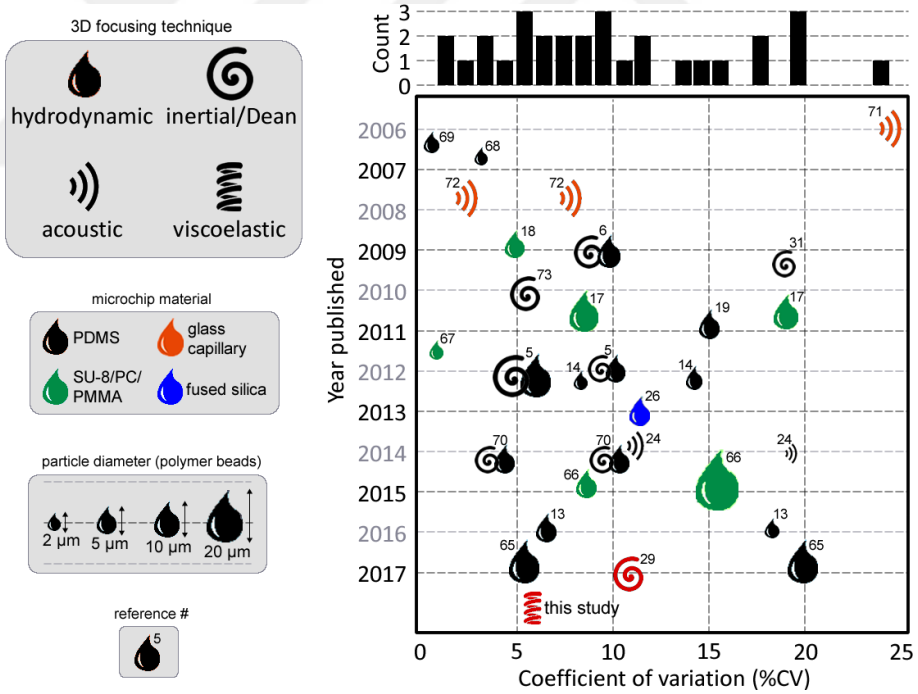


Figure 2.9: Comparison of the reported cytometers reported in the literature based on the particle focusing method. The CV values reported here are from either forward scatter (FSC), side scatter (SSC) or fluorescence (FL) measurements. If multiple values were reported in the same study, the lower CV value (i.e., best performance) was reflected in the chart. For some studies, experiments were performed with the different sizes of particles, which is also reflected in the chart. The HA-based sheathless microfluidic cytometry yields a CV value of 5.8% for FSC measurement.

The three most common methods for particle focusing in flow cytometry applications are sheath flow supported hydrodynamic focusing [4, 8, 56–58, 110, 111, 122–126], acoustic [64, 127, 128] wave assisted focusing, and passive inertial focusing [69, 76, 77, 128]. Few studies have used more than one method to support particle focusing in two lateral dimensions [2, 6, 105]. For the studies listed in Figure 2.9, we used the results obtained from polymeric test particles. We have plotted the best-reported CV value if multiple results are given in the study. As seen, there is a dispersion of CV values obtained using different focusing techniques. Most studies were able to obtain values below 10%. It is important to note that we have not credited the monodispersity of the test beads since it was not reported in most of the cases. Therefore, Figure 2.9 only gives an overview of the landscape for microfluidic cytometers rather than a strict comparison based on the CV values.

Our HA-MFC is the first reported study, to the best of our knowledge, integrating the viscoelastic particle focusing technique with optical flow cytometry in a microfluidic environment. The 5.8% CV level with our HA-MFC device is a promising result to use for the future of next-generation flow cytometry devices.

2.4 Concluding remarks

We demonstrated viscoelastic based optical microfluidic flow cytometry. We performed both in numerical and experimental studies and showed that 3D particle focusing is highly dependent on the rheological properties of viscoelastic solutions. Among the three most popular viscoelastic solutions (based on the reported studies in the microfluidic community), PEO- and HA-based MFCs give excellent performance in terms of %CV values.

Commercial flow cytometers require periodic maintenance, which involves optical alignment and routine calibration by a technician. Our system eliminates the need for tedious alignment by convinient assembly. With more improvements in the signal detection unit, the presented HA-MFC device can reach higher throughput and be used as a benchtop cytometer in clinics and research facilities.

Chapter 3

Impedance-based microfluidic flow cytometry using viscoelastic fluids

(Part of this study was published as "Impedance-based Viscoelastic Flow Cytometry" Murat Serhatlioglu, Mohammad Asghari, Mustafa Tahsin Guler, and Caglar Elbuken, *Electrophoresis*, December 19, 2018, Reproduced (or 'Reproduced in part') from Ref. [7] with permission from WILEY-VCH. https://doi.org/10.1002/elps.201800365)

3.1 Introduction

In impedance-based cytometry, particles are dispensed in ionic buffers (e.g., PBS) or electrolyte solutions. Then, impedance signals are acquired at the electrical detection region from individual particles/cells aligned in a single stream. Thus, the ionic concentration of the solution is critical and has to be adjusted to generate a contrast between the impedance of the particles and the suspending medium to ensure selectivity and high signal to noise ratio [129, 130]. Viscoelastic focusing used in optical cytometry applications in a straightforward manner [79, 102, 131].

Viscoelastic fluids have been prepared by dissolving polymeric (polyethylene oxide [79, 93, 95, 101], polyacrylamide [115], and polyvinylpyrrolidone [92, 94, 132] or biological (hyaluronic acid [74,88,99] and λ-DNA [115] substances in Newtonian fluids. Viscoelastic solutions are mostly biocompatible but may require further attention to ensure cell viability. Typically, 1X PBS is added to the viscoelastic solution to increase cell viability. However, the addition of a salt buffer solution may cause undesired changes in the rheological properties of viscoelastic solutions. For example, Giudice et al. reported that the addition of PBS to hyaluronic acid (HA) solution results in polymer shrinkage and impedes the shear-thinning properties of the viscoelastic solution [99].

Therefore, the implementation of viscoelastic solutions in impedance-based systems requires the analysis of the ionic buffer concentration and its effect on viscoelastic focusing due to the potential coupling of rheological and electrical properties of the carrier solution. In this study, we presented an impedance-based microfluidic flow cytometry device using polyethylene oxide (PEO) viscoelastic solutions. First, the dynamic viscosity of different molecular weight (M_w) and concentration of PEO polymer solutions were characterized to obtain constant viscosity over a wide range of shear rates to support stable particle focusing. Then, the effect of varying ionic concentrations of PBS (1X, 3X, 10X) on the rheological properties of PEO solutions was assessed. Later, particle focusing efficiency was observed in different ionic concentration viscoelastic solutions inside square cross section microchannels. Focusing of 6 µm diameter PS beads was observed in a range of Reynolds (Re) and Weissenberg (Wi) numbers ($0.04 <$

$Re < 32$) and ($3.9 < Wi < 2968$), respectively. Next, human RBCs were used in 1X-PBS/PEO solution to observe the focusing and orientation of cells in the 0.002<Re<0.44 range. Finally, impedance flow cytometry measurements were demonstrated for PS beads and RBCs suspended in 1X-PBS/PEO viscoelastic solutions, and the device performance was analyzed.

3.2 Materials and methods

3.2.1 Sample preparation

Three sets of viscoelastic solutions were prepared for the characterization of rheological properties (Anton Paar, MCR 301): i) Four different molecular weights of PEO polymer (M_w = 0.1, 0.6, 0.9, and 5 MDa, Sigma-Aldrich) were dissolved in DI water to a concentration of 1000 ppm. ii) PEO_{5MDa} was dissolved in DI water at five different concentrations (500, 1000, 2500, 5000, and 10000 ppm). iii) PEO_{5MDa} was dissolved in three PBS solutions (1X, 3X, and 10X) to a concentration of 1000 ppm. Spherical polystyrene particles of 6.0 µm diameter (Polysciences, Inc.) were suspended in viscoelastic solutions of 1X-PBS/PEO, 3X-PBS/PEO, and 10X-PBS/PEO at a concentration of 10^3 particles/ml. During the experiments, particles at the inlet were continuously mixed with a magnetic stirrer to keep the particle concentration uniform. 50 µl whole blood was finger pricked from a volunteer and immediately mixed with 10 µl EDTA (1.5 mg/ml) in an anticoagulant tube. Later, blood samples were added to a 1 mL 1X-PBS solution and centrifuged at 5000 rpm for 3 min. Finally, 5 µl of precipitated RBCs were dispensed in 5 mL 1X-PBS/PEO viscoelastic solution to a dilution of 1:1000 ratio.

3.2.2 Device fabrication

Fabrication steps are illustrated in Fig. 3.1.The fabricated microfluidic device consists of three parts: (I) 6 cm long 30 x 30 m^2 square cross-sectional PDMS microchannel, (II) three Cr/Au (10 µm wide, and 10 µm gap) coplanar microelectrodes on 25 x 75 mm^2 glass slide, and (III) a laser-cut PMMA clamp.

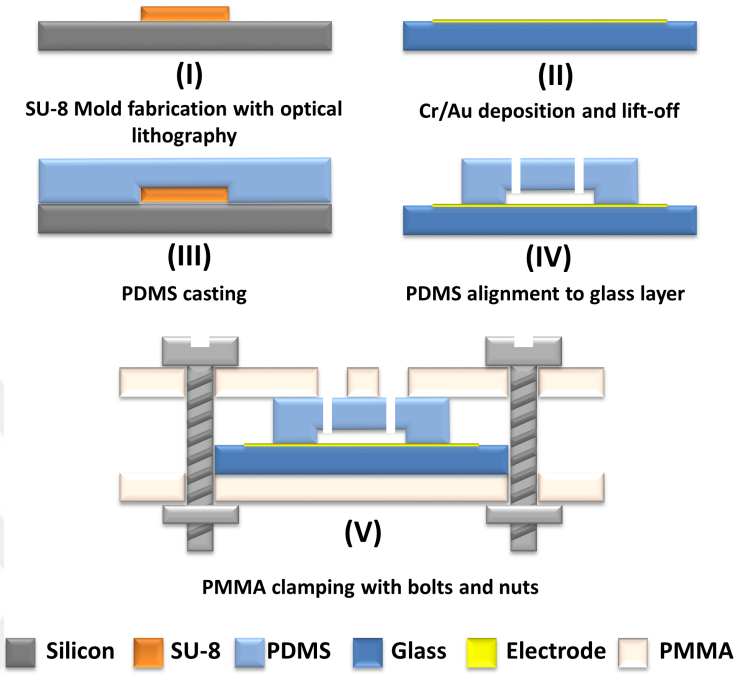


Figure 3.1: Illustration of the fabrication steps for impedance cytometry device.

(I) First, we prepared our optical lithography mask design and laser-printed on a 5 inch Cr/fused silica transparency photo-mask. Then, SU-8 2050 photoresist (PR) was spin-coated (acceleration: 500 rpm/s, speed: 500 rpm/s, time: 40 s) on a 4 inch diameter silicon wafer and prebaked (1 min, 65 °C / 3 min, 95 °C / 1 min, 65 °C). Next, PR was exposed to UV light under a mask aligner (EVG 620) at 60 mJ/cm^2 intensity and post-baked (1 min, 65 °C / 3 min, 95 °C / 1 min, 65 °C). The mold fabrication was finalized after developing the unexposed PR in the developer. For casting, a mixture of PDMS to curing agent at 15:1 was prepared and poured onto the mold, and cured on a hot plate (5 h, 80 °C). Finally, the cured PDMS was peeled off from the mold and inlet/outlet holes (1 mm diameter) were punched using a biopsy punch.

(II) Electrodes were fabricated using a lift-off procedure. First, a transparent glass slide 25x75 mm^2 was cleaned in a sonicator (5 min) with acetone and isopropyl alcohol (IPA). Then, it was rinsed in DI water and dried. The glass substrate was dehydrated in an oven (20 min, 110 °C). For the optical lithography process, AZ5214 positive PR was spin-coated (acceleration: 4000 rpm/s, speed:

2000 rpm/s, time: 45 s) onto the glass substrate and prebaked (1 min, 110 °C). Then, the spin-coated glass substrate was exposed to UV light (at 50 mJ/cm^2) under the transparency mask for electrode design in a mask aligner. Unexposed PR was developed in the mixture of AZ400K:DI water (1:4) developer solution for 1 min. Then, the substrate was treated by oxygen plasma (50 s, O_2: 30 sccm, N_2: 5 sccm) to clean the PR residues from the developed surface for an efficient lift-off process. Then, Cr/Au layers (10 nm/50 nm thick) were deposited in a thermal evaporator (VAKSIS). Finally, the substrate was dipped into acetone flask for 3 h and sonicated for 1 min for lift-off.

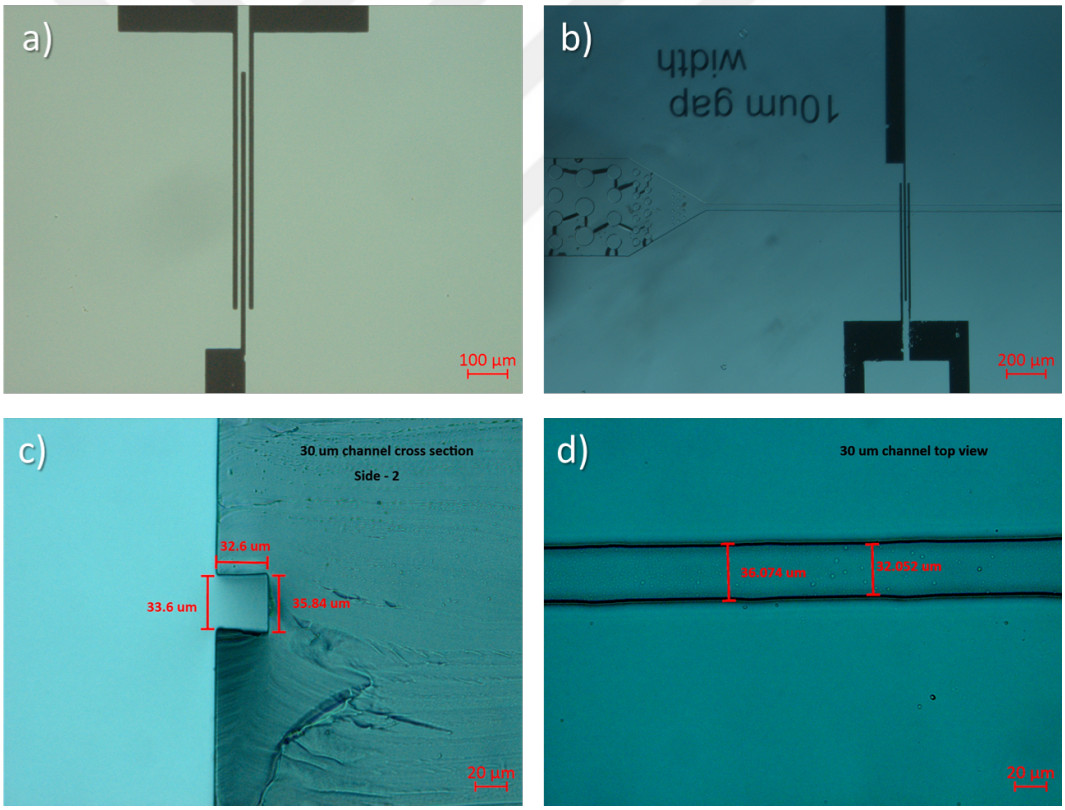


Figure 3.2: Microscope images of the fabricated device. (a) 10 µm electrodes on glass, (b) PDMS channel and glass substrate aligned on top of each other, (c) cross section, and (d) top view of PDMS channel.

(III) To complete the device fabrication, we used two different methods. For the initial particle focusing experiments, the PDMS channel layer was irreversibly plasma bonded to a clean glass slide (25x75 mm^2). We followed another approach for the impedance cytometry device to be able to reuse the electrode-deposited

glass substrate. We aligned the PDMS channel layer to the glass substrate and brought both in contact without any plasma treatment. Then, we sandwiched them in between two PMMA plates, which are prepared using a CO_2 laser cutter (Epilog CO_2 laser, in vector mode at 1000 DPI, 10 W laser power, 5 kHz frequency, and 5 mm/s translation speed). Thus, if the PDMS channel clogs, it is possible to open the sandwich by loosening the screws, clean the glass substrate, and replace the PDMS layer. Microscopy images of the complete device are given in Fig. 3.2.

3.2.3 Experimental setup and working principle

The schematic of the impedance-based cytometry device is shown in Fig. 3.3. Photography of experimental setup and microfluidic impedance cytometry device are shown in Fig. 3.4. It consists of a single inlet/outlet PDMS channel and three coplanar electrodes. Particles suspended in viscoelastic solutions are sent through the inlet and collected at the outlet. At specific flow conditions, due to the elastic lift or combination of both elastic and inertial lift forces, particles migrate to the center of the channel, and a single train of particles is reached upstream of the impedance sensing region. Electrodes are used in a differential configuration for electrical impedance measurements. The center electrode is stimulated with 1 $V_{p\text{-}p}$ bias voltage at 2.5 MHz AC signal, which is generated using the internal signal generator of the HF2LI Lock-in Amplifier (Zurich Instruments). Currents are collected from two side electrodes and converted to voltage using the HF2TA transimpedance amplifier (Zurich Instruments). The voltage signal is fed back to the input of the lock-in amplifier and demodulated. Fourth-order 1 kHz bandwidth, low-pass filter is selected for demodulation at 100 kSa/s sampling rate. To inspect the performance of the device, PS beads and RBCs are pumped through the inlet of the channel at varying pressures from 50 to 200 mbar for PS beads and 50 to 400 mbar for RBCs. Resulting signals are exported to a PC and post-processed with a Matlab script to acquire peak amplitude (peak-to-peak-voltage/2) and transition time of particles. Finally, the CV values for each inlet pressure value are examined.

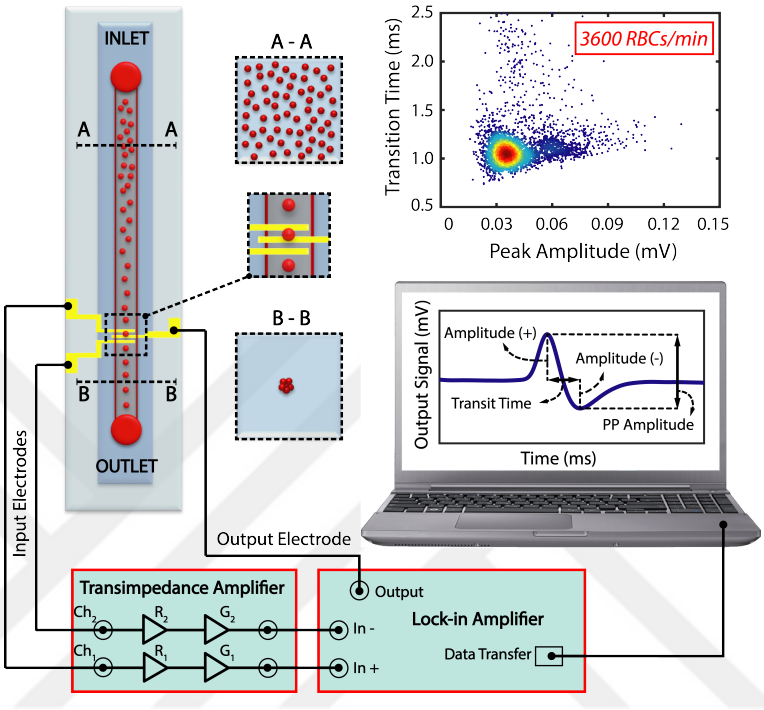


Figure 3.3: Illustration of the impedance-based viscoelastic flow cytometer.

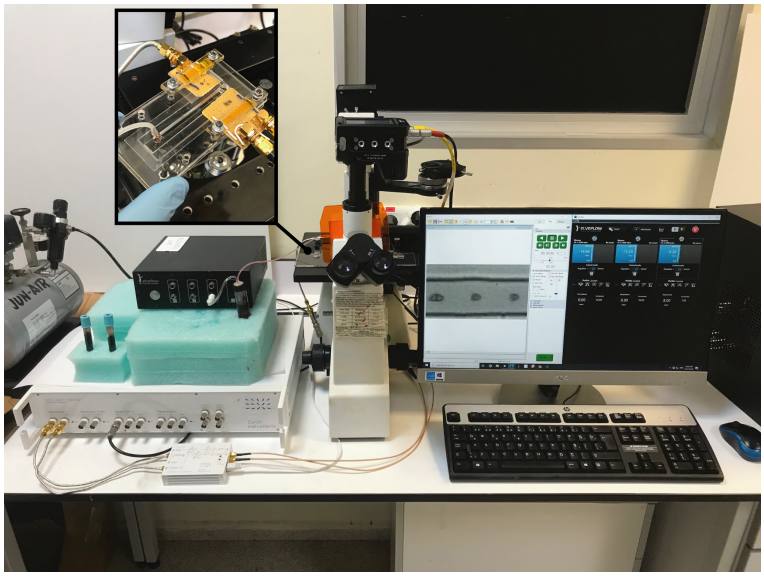


Figure 3.4: A photography of experimental setup and fabricated viscoelastic impedance cytometry device. Pogo pins are used to make connections between electrodes and lock-in amplifier units via SMA connectors on the FR2 circuit board.

3.3 Results and discussion

3.3.1 Solution characterization

The rheological properties of a viscoelastic fluid are essential for the performance of viscoelastic focusing and equilibrium position of particles in the fluidic channel [133]. We characterized the viscoelastic solutions for varying polymer length (M_w), polymer concentration, and ionic salt concentration to understand the rheological changes. The results of these rheology measurements are given in Fig. 3.5. We used a cone and plate (CP) measurement fixture CP50-1 (50 mm diameter, 1° cone angle) to provide homogeneous shear conditions thanks to the constant shear rate with the conical gap of the fixture.

Shear viscosity measurements of four different M_w, PEO solutions of the same concentration (0.1% w/v) are given in Fig. 3.5.a. High M_w viscoelastic solutions have higher elasticity since they exhibit longer relaxation time and higher viscosity. PEO_{5MDa} solution exhibits higher shear viscosity compared to low M_w solutions. The following characterizations were performed with PEO_{5MDa}.

Figure 3.5.b shows shear viscosity measurements of PEO_{5MDa} for five different concentrations. It is essential to keep the solution at constant shear viscosity range since particles in shear-thinning liquids show a tendency to migrate away from the center to the walls of the channel [82,99]. The low concentration solution, 0.05% of PEO_{5MDa}, shows almost shear constant viscosity that is desired for efficient particle focusing. On the other hand, the high concentration solutions ($\geq$ 0.1% w/v) yield a shear-thinning profile. Thus, 0.05% w/v PEO_{5MDa} is chosen for the flow focusing experiments.

Yu et al. performed a series of rheometer measurements to show the effect of NaCl added into a PEO solution and demonstrated that the rheological properties are insensitive to the addition of NaCl up to 2% w/w in 10% w/w concentration PEO_{2MDa} solution [134]. PBS includes various salts, and its behavior in PEO based viscoelastic solutions needs to be characterized before impedance cytometry measurements. PEO based viscoelastic solutions were prepared in three

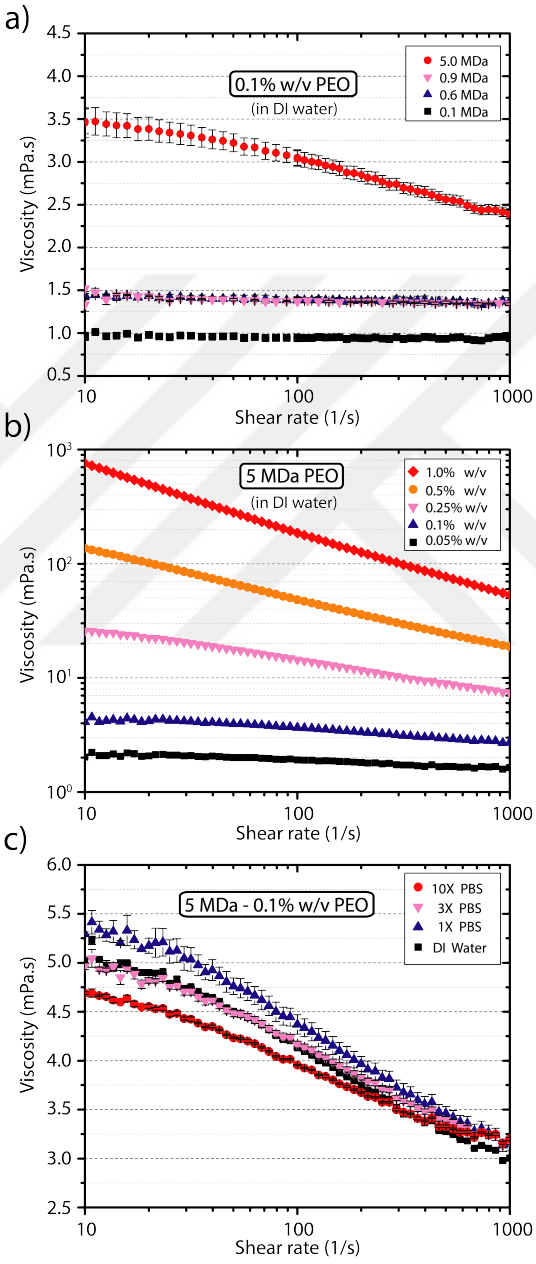


Figure 3.5: Shear rate dependence of viscosity of PEO solutions: (a) four different M_w PEO solutions at 0.1% w/v concentration, the error bars represent 2 S.D. of five multiple measurements, (b) five concentrations of PEO_{5MDa} solution (the error bars are smaller than the measurement markers), and (c) 0.1% w/v PEO5MDa solution at three ionic concentrations and DI Water

varying concentrations of PBS with constant polymeric concentration. We observed negligible change in viscosity for varying ionic buffer concentrations in Fig. 3.5.c.

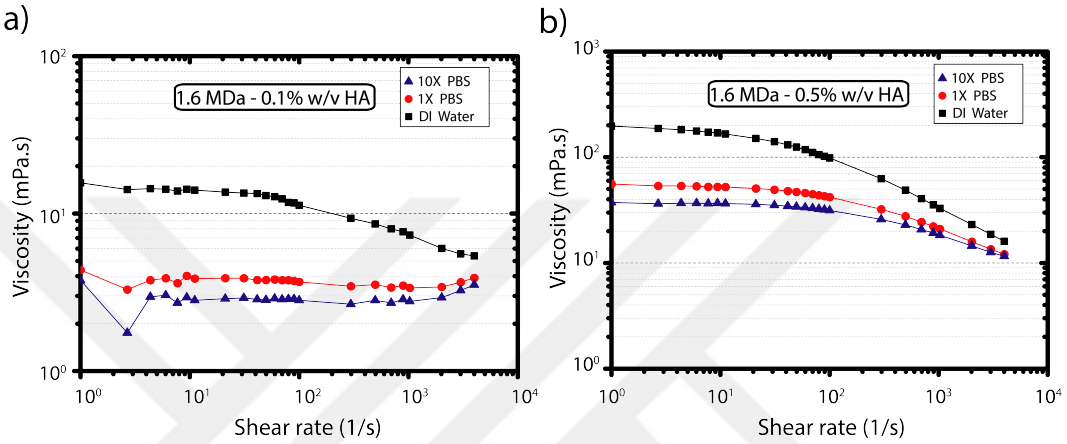


Figure 3.6: Shear rate and ionic concentration dependence of viscosity of HA solutions for different polymer concentrations: (a) 0.1% w/v and (b) 0.5% w/v.

Similar to the salt addition experiments with PEO solutions, the viscosity dependency on ionic concentration was also studied for HA-based viscoelastic solutions. Figure 3.6 shows how ionic concentration varies the shear viscosity of 0.1% and 0.5% w/v concentration 1.6 MDa HA viscoelastic solutions. 1X PBS-HA solution has almost four times lower viscosity compared to no salt addition HA. Increasing the concentration of PBS buffer to 10X has no marginal change to 1X PBS buffer in HA viscoelastic solution. These results clearly show the distinction between the behaviors of HA and PEO solutions and reveal that the ionic buffer concentration in PEO based viscoelastic solutions has a negligible effect on viscosity. Therefore the rheological and the impedimetric properties of the solution can be adjusted independently.

3.3.2 Flow focusing vs ionic buffer concentration for particles

Rheometer measurements in the previous section give an insight into the effect of PBS in the viscoelastic PEO solution. It is still required to observe particle migration and focusing dynamics (elastic or elasto-inertial) for different PBS

Table 3.1: Dimensionless numbers and experimental parameters for the bead experiment.

Q (µl/h)	$\dot{\gamma}_w$ (1/s)	Re	Wi	El
10	154.6	0.042	3.9	92.8
20	309	0.085	7.8	92.8
40	618	0.17	15.6	92.8
100	1546	0.42	39	92.8
200	3092	0.84	78	92.8
950	14690	4.0	371	92.8
1900	29370	8.0	742	92.8
7600	117500	32	2968	92.8

Table 3.2: Dimensionless numbers and experimental parameters for the RBC experiment.

P (mbar)	Q (µl/h)	Re	Wi	El
5	0.58	0.002	0.23	92.8
23	2.66	0.011	1.04	92.8
48	5.55	0.023	2.17	92.8
117	13.5	0.057	5.27	92.8
225	26	0.11	10.15	92.8
410	47.4	0.2	18.5	92.8
540	62.4	0.26	24.4	92.8
900	104	0.44	40.6	92.8

concentrations in microchannels. 500 ppm PEO_{5MDa} viscoelastic solutions were prepared in three different PBS concentrations (1X, 3X, and 10X). Then, 6 µm PS beads were pipetted (10^3 particles/ml) to the prepared solutions and were pumped through the microchannels using a syringe pump (KDS 100). Particle focusing at varying flow rates was observed and recorded at 5000 fps under an inverted optical microscope (Zeiss) equipped with a high-speed camera (Phantom Miro e2), as given in Fig. 3.7.a and 3.7.b. Recorded videos were split to single frames and image-stacked to form a single picture. The relaxation time for 500 ppm PEO_{5MDa} (λ=25.27 ms) and dimensionless numbers for PS bead and RBC focusing experiments (Table 3.1 and 3.2) are calculated using the equations given in Chapter 1 and 2.

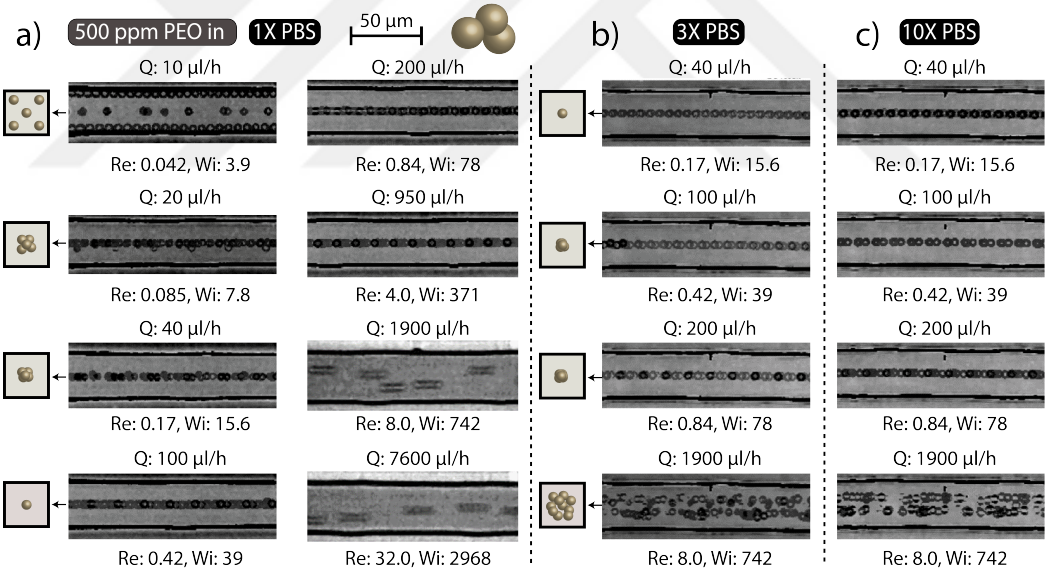


Figure 3.7: Image stacks of focusing of 6 µm diameter PS beads (a) PS beads suspended in 500 ppm, PEO_{5MDa} dissolved in 1X PBS solution and (b) PS beads suspended in 500 ppm, PEO_{5MDa} dissolved in 3X and 10X PBS solutions.

In Figure 3.7.a, at low flow rates (<20 µl/h), PS particles migrate both to the center and corners of the channel, which corresponds to low first normal stress difference regions [71], when inertial lift force is negligible (Re<0.1). When the flow rate is increased until 40 µl/h, corner-aligned particles migrate to the center of the channel due to the contribution of inertial lift forces. Particles closer to the walls are under the influence of wall-induced lift force and migrate to the center of the channel by increasing the flow rate. For flow rates between 40

µl/h (Re: 0.17) to 950 µl/h (Re: 4.0), the particles are aligned at the centerline thanks to the contribution of inertial lift force. Central particle trajectory starts to deteriorate at higher flow rates above 950 µl/h due to the conquering of the inertial lift forces over elastic forces. We observed a disturbed particle train at the flow rates above 1900 µl/h (Re: 8.0) to 7600 µl/h (Re: 32.0). At high flow rates, due to image blurriness, we present snapshot images (instead of image-stack). Recently, Kim et al. successfully achieved elasto-inertial focusing at higher flow rates (1300 µl/h) using a λ-DNA solution [115]. Lim et al. showed elasto-inertial focusing at extremely high flow rates (50 ml/min) using hyaluronic acid (HA) based solution [88]. However, these biological solutions use polymers that carry ionic side chains. In such a case addition of ionic buffer changes the rheological properties of solutions that lead to deterioration of particle focusing efficiency [33].

We observed almost identical focusing profiles for two other PBS-based (3X and 10X) viscoelastic solutions in Fig. 3.7.b that verifies the potential of PEO to be used in impedance-based viscoelastic flow cytometry. Particles are aligned at the center of the channel at 40 µl/h and maintained at their central trajectories at 200 µl/h. At the flow rate of 1900 µl/h, particles are dislocated from their central position due to the strong influence of inertial lift force similar to the 1X PBS experiment. Based on these results, we conclude that the amount of ionic concentration has no apparent influence on the rheological properties of the viscoelastic solution or the particle focusing performance. Thus, the synthetic polymer PEO is a good candidate for viscoelastic based particle focusing for impedance cytometry applications.

Next, we investigated the viscoelastic focusing behavior for human RBCs that will potentially pave the way to numerous applications for non-spherical particle alignment and impedance-based measurements. We suspended the RBCs in 1X-PBS/PEO solution and observed the particle focusing efficiency for increasing flow rates. The suspension was pumped through the channel with a pressure pump (Elveflow OB1). Snapshots from the recorded videos at specific flow rates are given in Fig. 3.8, which depicts the trajectory of RBCs along the microchannel. Elastic force is weak at meager flow rates (0.6 µl/h). When the flow rate is

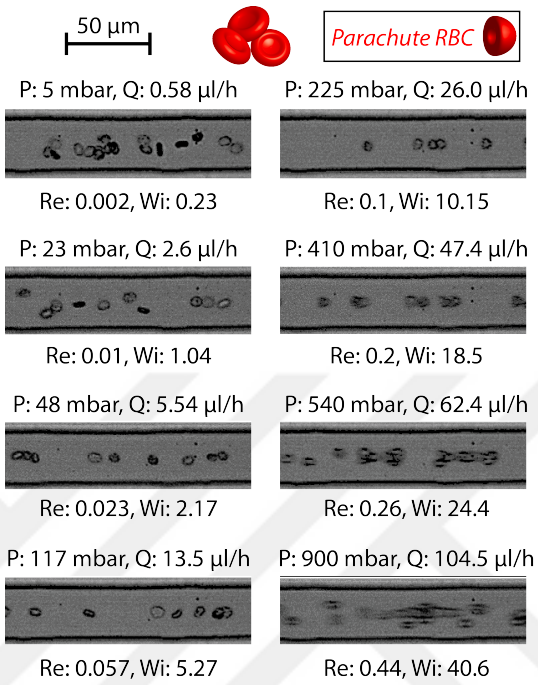


Figure 3.8: Image-stacking images of the focusing RBCs. RBCs suspended in 500 ppm, PEO_{5MDa} dissolved in 1X PBS solution.

increased to 2.6 µl/h, RBCs are partially aligned to a single trace. At 5.5 µl/h (Re: 0.02), a fully aligned single trace of RBCs is achieved at the centerline of the channel. The focused RBCs form a parachute shape when the flow rate is between 15 µl/h to 30 µl/h (0.07<Re<0.15). At higher flow rates, 40 µl/h (Re: 0.2), we observed deterioration of focusing trajectory. At such flow rates, the high elastic force causes excessive stretching on deformable RBCs, which corresponds to a decrease in the hydrodynamic diameter [21]. Since the lateral particle migration in viscoelastic flow depends on the ratio of particle size to the channel height, viscoelastic focusing is not achieved at such an extreme size reduction.

In summary, PS beads were aligned at the four corners together with the centerline at 10 µl/h (Re: 0.017). Centerline alignment was achieved in the range of 0.17<Re<4.0. However, RBCs are focused only at the centerline in the range of 0.02<Re<0.2. This difference originates from the highly deformable structure of RBCs, which are exposed to both elastic and deformation-induced wall lift force. The wall lift force is induced by the asymmetrical deformation of particles when they are very close to the channel wall. Eventually, deformable particles

are pushed away from the corners to the center of the channel [94].

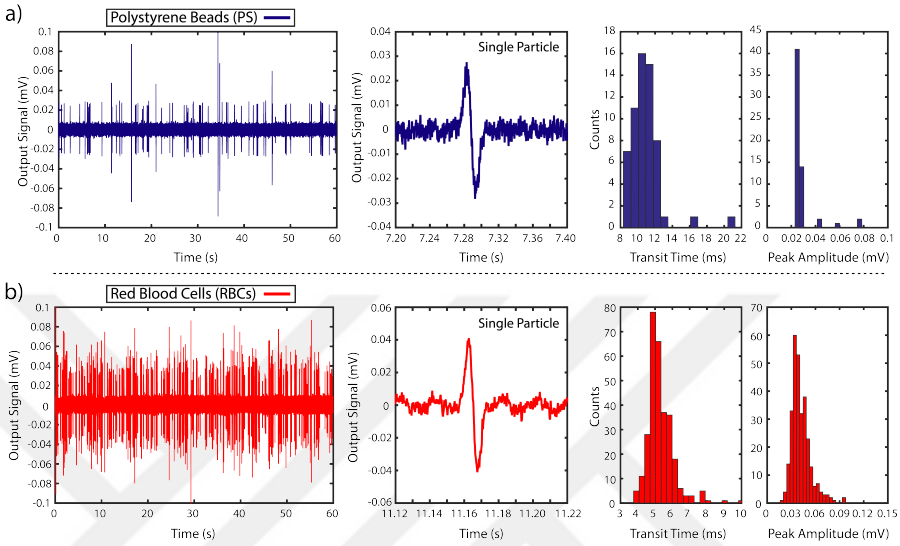


Figure 3.9: Impedance cytometry results for (a) PS beads and (b) RBCs at 50 mbar inlet pressure (left). Close-up images of single-particle events showing the characteristic differential impedance signal profile (middle). Histogram plots of transit time and peak amplitudes corresponding to all events (right).

3.3.3 Impedance-based cytometry measurements

The impedance measurements are based on sensing of the differential change on the electrical signal when particles pass over the electrodes and interact with the electric field. The particle transition time (Transit Time) was defined by the time difference between the signal maximum and minimum points. The voltage signal amplitude is related to the size of the particle since the cell membrane behaves as a barrier and current flows from the outer region of the cell at low excitation frequencies (< 2 MHz). Therefore, peak-to-peak amplitude of the signal (PP Amplitude) is a characteristic of cell size.

Differential impedance measurements have been performed using 6 µm diameter PS beads and human RBCs in 1X-PBS/PEO based viscoelastic solutions. The solutions were introduced to the channel using a pressure pump set at 50 mbar. Figure 3.9 gives read-out signals, close-up views for single-particle events, and histogram plots of transit time and peak amplitude. For PS beads, 60 events were collected in 1 min of measurement. The close-up of a single event shows

the differential measurement waveform. The transit time for the focused beads is accumulated around 10-12 ms; two events occurred at 16 and 22 ms. Unlike time measurements, voltage signal amplitude shows narrower distribution and is accumulated at 0.02 mV level. Higher amplitude events rarely occurred. Higher transit time variation is the evidence of insufficient particle focusing at the center of the channel. 50 mbar pressure corresponds to a 5-6 µl/h flow rate at which particles are under the influence of viscoelastic focusing (corners and center equilibrium positions for suspended rigid particles) far from the elasto-inertial regime. The more significant variation in the signal amplitude is a clue of particle clusters (doublets, triplets, and more). Obtaining integer multiples of signal levels, such as two (0.04 mV), three (0.06 mV), and four (0.08 mV) folds of the main signal (0.02 mV), confirms the aggregation of particles.

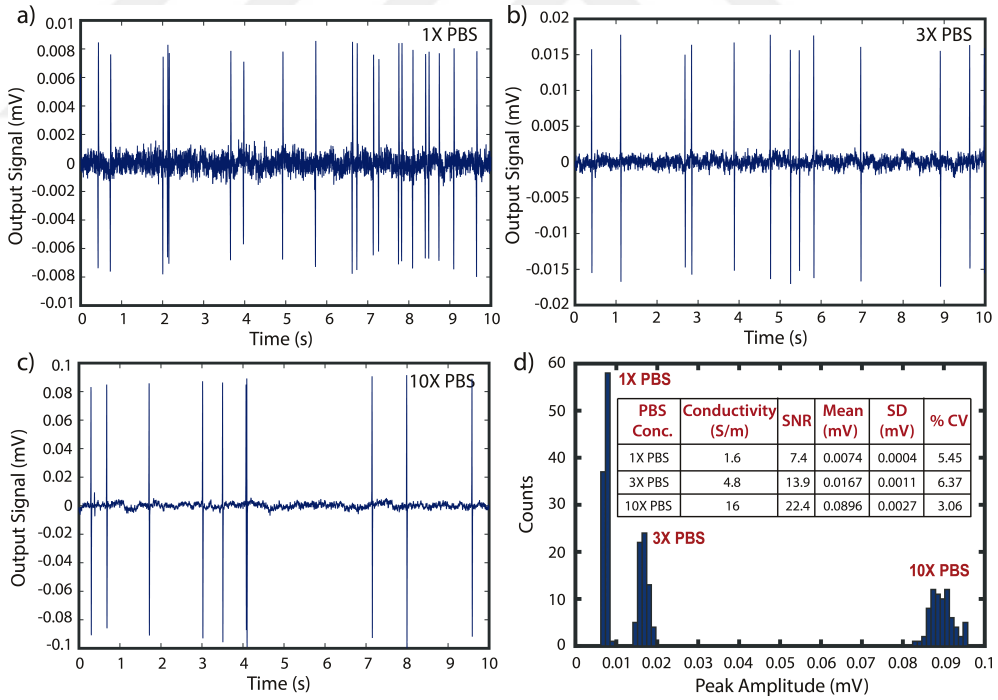


Figure 3.10: Viscoelastic impedance cytometry results for 6 µm diameter PS beads at 50 mbar inlet pressure. 10 s time window data using 500 ppm PEO_{5MDa} viscoelastic solutions with varying PBS concentrations: (a) 1X PBS, (b) 3X PBS, (c) 10X PBS, and (d) histogram plots and statistical results of peak amplitudes for 1 min.

It is well-known that the signal amplitude is a strong function of solution conductivity, which depends on PBS concentration in our case. We performed

viscoelastic particle focusing experiments with 6 µm PS beads suspended in PEO_{5MDa} 500 ppm viscoelastic solutions using 1X, 3X, and 10X PBS buffers. Figure 3.10.a-c shows the output signals for 10 s and Fig. 3.10.d gives the peak amplitude histograms for three different conductivity solutions for 1 min. Mean values of the peak amplitude increase with increasing solution conductivity, since stronger impedance contrast is obtained between the particle and the carrying medium. Thus, we obtained a higher signal to noise ratio with increasing PBS concentration. However, for the case of impedimetric detection of living cells (RBCs), high ionic concentration in the solution causes cell damage. In Fig. 3.11 RBCs only suspended in 1X-PBS, or 1X-PBS/PEO solution can preserve their shape. Therefore 1X-PBS/PEO solution is the optimum solution for impedance cytometry measurements.

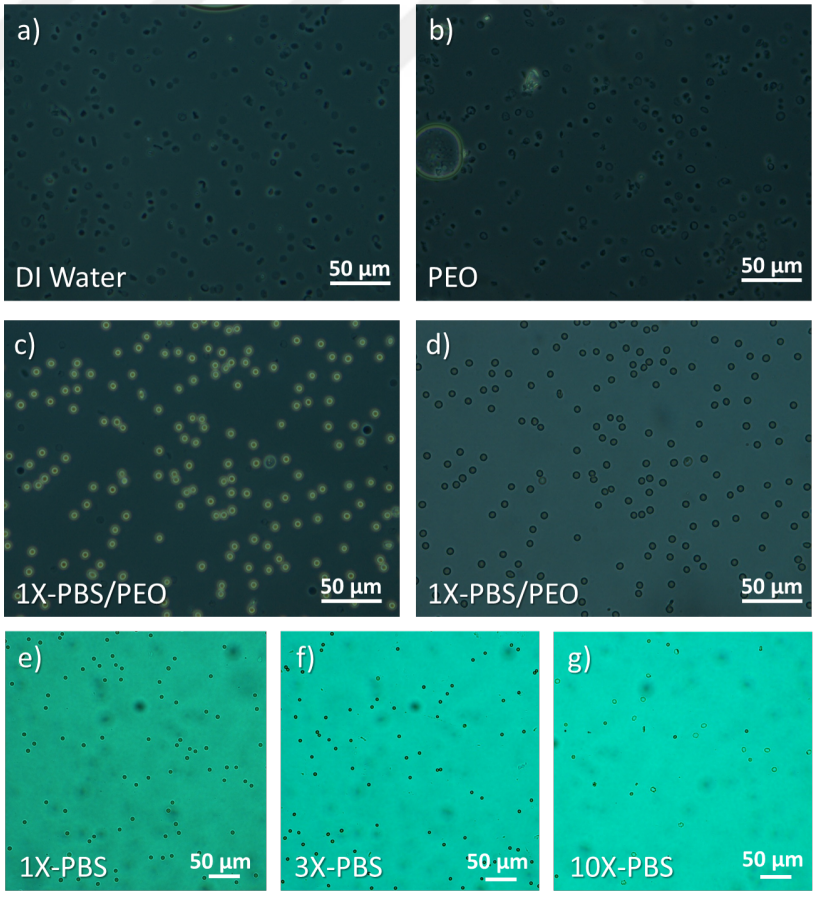


Figure 3.11: Optical microscope images for RBC suspension in (a) DI Water, (b) PEO_{5MDa}, (c-d) 1X-PBS/PEO, (e) 1X-PBS, (f) 3X-PBS, and (g) 10X-PBS.

Measurements at higher flow rates were performed to understand the behavior of viscoelastic focusing and the corresponding signal change. The inlet pressure was varied between 50, 100, 150, and 200 mbar for PS beads; and 50, 100, 150, 200, 250, 300, and 410 mbar for RBCs. The statistical comparison of transit time and signal amplitude for all pressure levels are summarized as mean value, standard deviation, and %CV in Fig. 3.12.a and 3.12.b. To isolate doublets, triplets, and clumps, a gated window was selected for %CV calculations, which removes the statistical outliers while including more than 90% of the events. The mean values of transit time for both PS beads and RBCs decrease with increasing pressure rates. Corresponding %CV values are approximately 10-15% for both particles. The signal amplitude for PS beads is similar for increasing flow rates showing that viscoelastic focusing is stably maintained. However, %CV for the peak amplitude of RBCs shows a more significant change at the two points: 20% increase from 100 to 150 mbar and 30% increase from 250 to 300 mbar.

We have previously shown in Fig. 3.8.c that RBCs start to deform into a parachute shape above 100 mbar. When the inlet pressure reaches 250 mbar, all the RBCs get to the same shape. The results are given in Fig. 3.12.b show that aligning RBCs into a single orientation leads to more position sensitive and precise measurements. Moreover, when the pressure is above 400 mbar, flow focusing is disturbed due to excessive size stretching of cells and corresponding hydraulic diameter reduction. This behavior leads to discontinuity of single-particle train viscoelastic focusing and gives higher measurement variation and %CV values.

Figure 3.13 shows transit time versus peak amplitude scatter plots for RBCs at selected pressure values. The throughput is 600, 1800, 3600, and 5700 RBCs/min for 100, 150, 250, and 410 mbar, respectively. At all pressure rates except 410 mbar, peak amplitudes are populated at 0.04 ± 0.01 mV; there is a side population at 0.06 mV with the same transition time range. At 410 mbar, 0.06 mV peak amplitude reaches to the highest number of population. These results are in line with our previous observations that beyond 410 mbar RBCs are unable to cope with elastic force and lose their trajectory at the center of the channel.

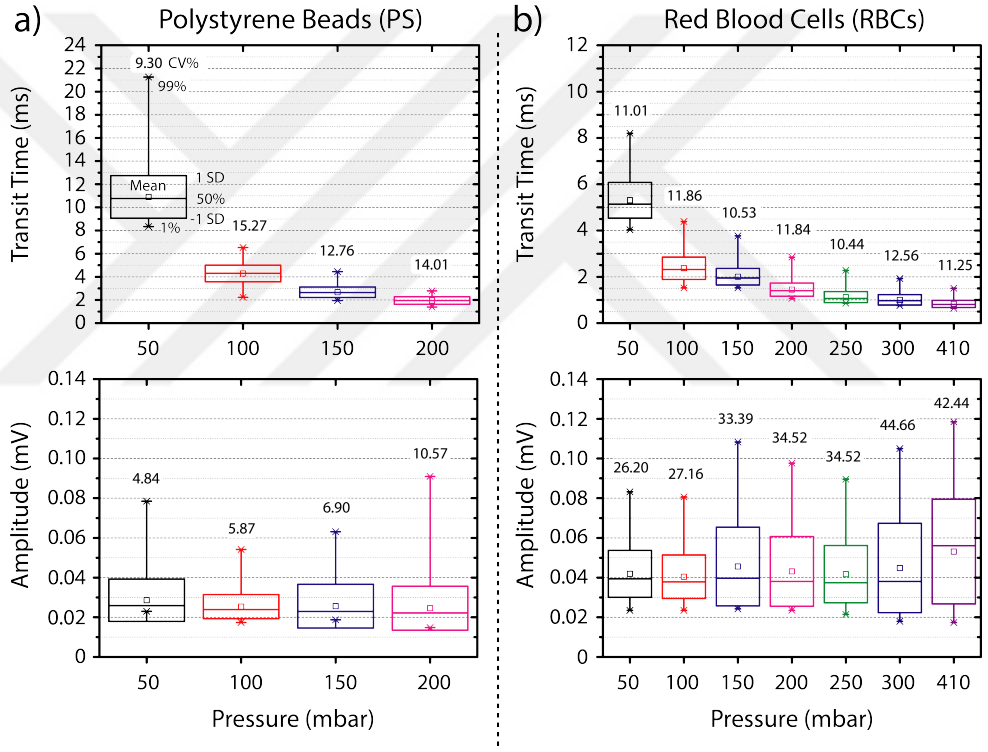


Figure 3.12: Bar chart representation of transit time, peak amplitude, and % CV of (a) PS beads and (b) RBCs detected at varying inlet pressures. For each bar graph, the square represents the mean value, the box represents the standard deviation, and the whisker lines represent the 99% and 1% population of the counted events.

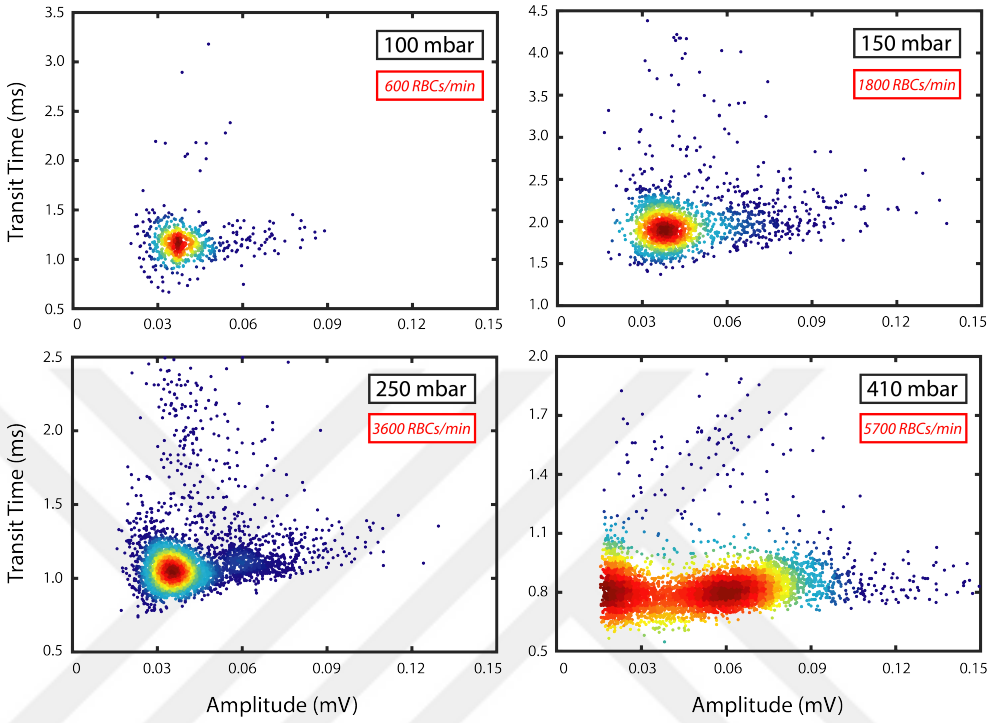


Figure 3.13: Scatter plots of transit times vs peak amplitudes at four inlet pressures for RBC impedance measurements.

3.4 Concluding remarks

Herein, we have assessed the effect of ionic buffer concentration in viscoelastic focusing using both rheometer measurements and focusing trajectories in square cross-sectional microfluidic channels at varying flow rates. Ionic concentration rate is critical for cell viability and impedance measurements. We concluded that shear viscosities and focused particle trajectories showed no observable dependency on the concentration of PBS from 1X to 10X. These results verify that PEO viscoelastic solutions are good candidates for impedance based measurement applications as opposed to polyelectrolyte viscoelastic solutions, such as HA, which have a high rheological dependency on ionic concentration of the solution. We optimized the PEO_{5MDa} viscoelastic solution at 500 ppm concentration for efficient particle focusing. Elasto-inertial particle focusing at high Reynolds number (Re: 4.0) was successfully achieved for PS beads. The focusing of RBCs was possible at a considerably low Reynolds number (Re<0.2). Additionally, parachute shape single RBC orientation is achieved at Re: 0.1. Achieving fixed

particle orientation for non-spherical objects is very critical in cytometry applications to get low signal variations. By tuning the properties of the viscoelastic solution, we were able to achieve this property for a range of flow rates. Finally, we performed impedance cytometry measurements for PS beads and RBCs. For the first time in the literature, we combined the viscoelastic particle focusing technique with an impedance-based microfluidic cytometry device. We achieved 3600 cells/min throughput for RBC characterization. Viscoelastic focusing addresses the need for a single train of particle trajectory required for planar electrode configuration impedance based cytometry systems. Obtaining a single stable orientation for non-spherical particles differentiates viscoelastic focusing from other focusing techniques. The simplicity of viscoelastic focusing with the combination of impedance measurement results in a powerful tool for cell counting and sizing applications. This method is specifically useful for the morphology-based characterization of disease-infected cells.

Chapter 4

A unifying study on electro-viscoelastic migration (EVM) under simultaneously applied pressure-driven flow and electric field

(Part of this study was published as "Electro-viscoelastic migration (EVM) under simultaneously applied microfluidic pressure-driven flow and electric field" Murat Serhatlioglu, Ziya Isiksacan, Melis Ozkan, Donus Tuncel, and Caglar Elbuken, *Analytical Chemistry*, April 16, 2020, Reproduced (or 'Reproduced in part') from Ref. [135] with permission from American Chemical Society. https://doi.org/10.1021/acs.analchem.9b05620)

4.1 Introduction

Microfluidic devices enable precise control on particle migration in Newtonian and viscoelastic media under pressure-driven flow, which leads to a rich spectrum of applications including counting [7, 88, 102, 115, 131], focusing [79, 136, 137], and sorting [99, 100, 132, 138, 139] of particles. Simultaneously applying DC electric field with pressure-driven flow brings a new modality to tune particle equilibrium positions. The electric field induces a lateral electrophoretic force on the charged particles, thereby generating particle motion relative to the direction of the flow. However, the observations of particle migration under simultaneous pressure-driven flow and DC electric field yielded anomalous cross-sectional particle migration [140]. DNA molecules migrated towards the capillary center when electrophoretic force is in the same direction as the pressure-flow (concurrent) and towards the capillary wall when the pressure-flow direction was reversed (countercurrent). Analytical and experimental studies have been conducted to understand the physics underlying the cross-sectional migration under simultaneous pressure-driven flow and DC electric field. We categorize these studies into four groups, as shown in Figure 4.1: (I) polyelectrolyte migration in Newtonian medium, (II) particle migration in Newtonian medium, (III) polyelectrolyte migration in viscoelastic medium, and (IV) particle migration in a viscoelastic medium.

The principles of particle migration behavior observed in the first four categories (I-IV) have been investigated in the literature. (I) Polyelectrolyte λ-DNA migrated towards the center (wall) in the concurrent (countercurrent) case in the Newtonian buffer solution. This migration was attributed to the weak electro-hydrodynamic interactions and dipolar flow fields between the DNA segments [141–144]. (II) Charged particles (polystyrene beads, human cells) migrated towards the wall (center) in the concurrent (countercurrent) case in the Newtonian buffer solution. This migration was attributed to slip velocity, which is the velocity difference between the particle and the fluid. Slip velocity interacts with the local shear field and causes a net cross-stream migration [145–149]. (III) Polyelectrolyte DNA samples migrated towards the center (wall) in the concurrent (countercurrent) in PVP-based viscoelastic solutions [150, 151]. The amplitude

and the direction of the electric field modulate the shear around the DNA, which consequently affects the elastic lift force. Thus, the direction of the lift force flips according to the modulated shear. (IV) Charged Polystyrene (PS) particles suspended in Polyethylene Oxide (PEO)-based viscoelastic solution migrated towards the center (wall) in the concurrent (countercurrent) case. The results were attributed to the electrophoretic motion-induced extra lift force, originated from the nonlinear coupling of an external force-driven particle and the local viscoelastic shear flow, in the viscoelastic fluid [147]. An in-depth theoretical discussion of particle migration in viscoelastic flow under the external electric field was recently given [152].

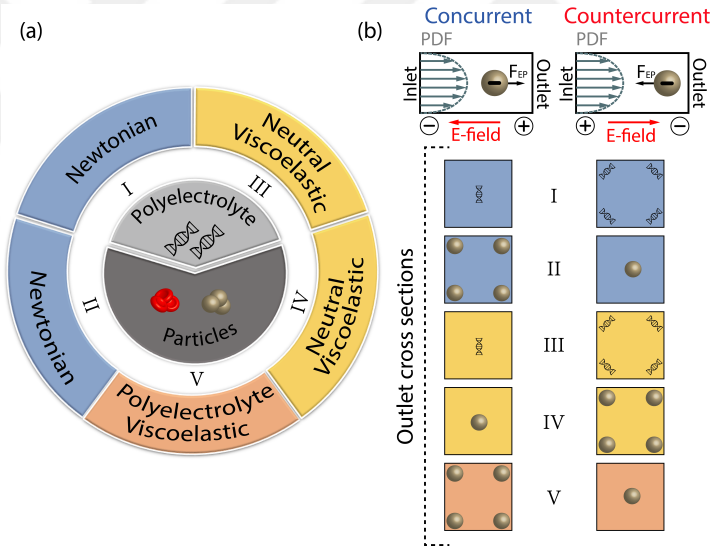


Figure 4.1: Schematic illustration of the reported studies in the literature for migration under simultaneously applied pressure-driven flow and electric field configuration. (a) Studies are categorized according to the medium (outer ring) and the particles of interest (the inner circle) as a pie chart. (b) Schematic of the particle equilibrium states at the outlet cross sections in a microfluidic channel according to the electric field direction, medium, and suspended particles. The first four groups (I-IV) are cited from the literature, and the fifth group (V) represents our study of particle migration in polyelectrolyte viscoelastic solution. F_{EP}: electrophoretic force, PDF: Pressure-driven flow.

Here, we introduce a new group, the fifth group (V), particle migration in a polyelectrolyte viscoelastic medium, and introduce Electro-Viscoelastic Migration (EVM) to explain the migration behaviors in groups III, IV, and V. Consequently,

we propose a unifying hypothesis to explain the underlying mechanism of cross-sectional particle migration in microchannels.

In our study, we performed particle migration experiments with PS particles suspended in (II) deionized (DI) water as well as (IV) PEO-based neutral and (V) Hyaluronic acid (HA-based polyelectrolyte viscoelastic solutions in a microfluidic channel under simultaneous use of pressure-driven flow and DC electric field as illustrated in Fig. 4.2. We observed particle equilibrium positions at the microchannel, 1 cm away from the outlet, under an optical microscope. In DI Water, particles migrated towards the channel wall in the concurrent case and the channel center in the countercurrent case. The same results were obtained for HA-based viscoelastic solutions, whereas particle equilibrium positions were reversed for PEO-based solutions. Although both PEO and HA have viscoelastic properties, the steady-state migration profile surprisingly exhibited opposite migration results.

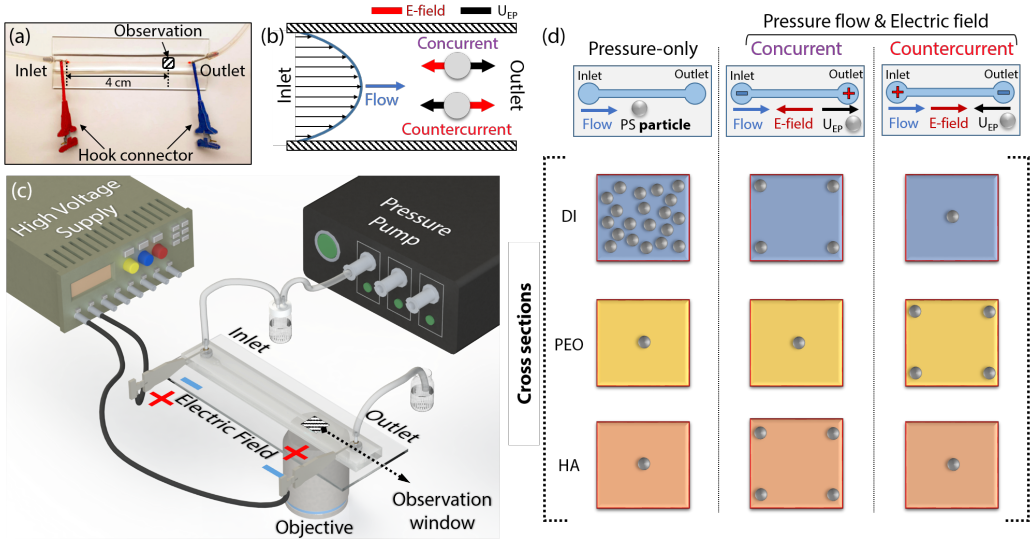


Figure 4.2: Illustration of the microfluidic test setup and summary of particle equilibrium states at the microchannel outlet cross sections. (a) Photo of the fabricated microfluidic chip. (b) Schematic representation of the experimental system. (c) Illustration of the electric field, electrophoretic force, and Poiseuille flow distribution in the microchannel. (d) Illustration of particle equilibrium positions at the outlet cross section.

We believe that the reason for the anomalous cross-stream migration difference between PEO- and HA-based solutions is due to the polyelectrolyte nature of HA [153]. We showed that electrophoretic force affects the HA polyelectrolyte, unlike PEO neutral polymers. This difference generates a net cross-stream migration for both HA polymers and PS particles that is the opposite of usual particle migration behavior in neutral viscoelastic solutions, as demonstrated by our confocal microscopy experiments. To explain this particle migration behavior in viscoelastic solutions, we propose the Electro-Viscoelastic Migration (EVM) theory.

4.2 Materials and methods

4.2.1 Sample preparation

Viscoelastic solutions were prepared by dissolving polymer (PEO, HA) powder in DI Water at the given concentration. Three different particle suspensions were prepared for the particle migration experiments: DI Water, 500 ppm PEO_{5MDa}-(Sigma Aldrich), and 1000 ppm $HA_{1.5MDa}$-based (NewDirections) viscoelastic solutions. Ten different particle suspensions were prepared: 2000 ppm, 1000 ppm, 500 ppm, 100 ppm, 50 ppm of PEO_{5MDa}- and 5000 ppm, 2000 ppm, 1000 ppm, 200 ppm, 100 ppm of $HA_{1.5MDa}$-based viscoelastic solutions. Shear-dependent viscosity of solutions was measured using a rotational rheometer (Anton Paar, MCR 301). 6 µm diameter spherical polystyrene particles (Polysciences, Inc.) were suspended with the same concentrations (10^3 particles/ml) in each solution. During the experiments, particles at the inlet vial were continuously mixed with a magnetic stirrer to keep the particle concentration uniform.

Figure 4.2 shows the shear-dependent viscosity of the sample solutions measured using a rotary rheometer with a 50 mm diameter CP-50 cone plate fixture.

Particle zeta potentials in suspensions were measured in Malvern Nano ZS ZEN3600 zeta sizer as -60 mV in DI Water, -80 mV in PEO, and -110 mV in HA.

Fluorescent solutions were prepared using two different dyes. Fluorescent dyes

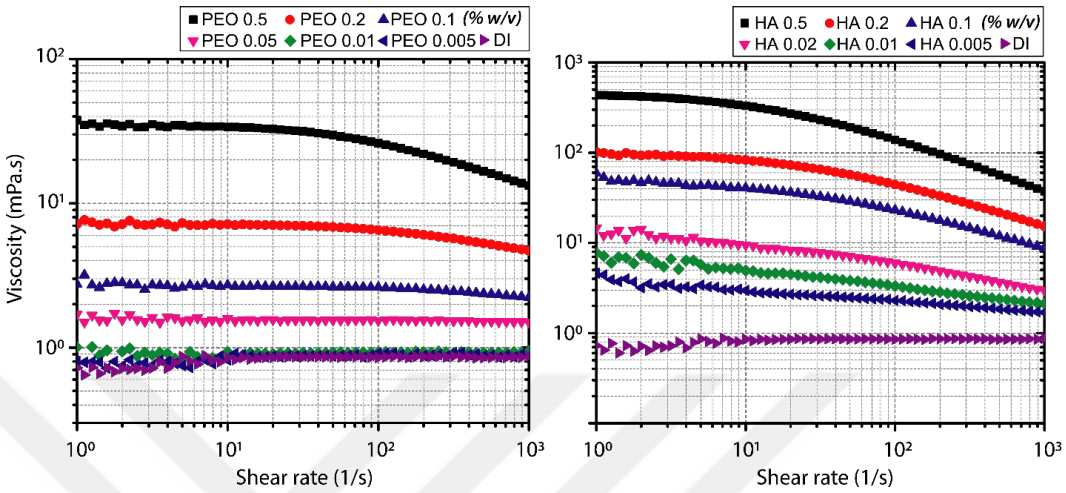


Figure 4.3: Shear viscosity measurement as a function of shear rate.

(green-Coumarin 343 and blue-DAPI), N-(3-Dimethylaminopropyl)-N'-ethyl carbodiimide hydrochloride (EDC) and 4-(Dimethylamino) Pyridine (DMAP) were purchased from Sigma Aldrich. PEO and HA were labeled with Coumarin 343 and DAPI, respectively, using a similar procedure through an EDC coupling reaction. For a typical labeling procedure: Polymer (PEO or HA) (50 mg) was dissolved in water (5 mL) in a round bottom flask (RBF). Subsequently EDC (3.0 mg, 0.016 mmol) and DMAP (3.0 mg, 0.025 mmol) were added, and the resulting solution was stirred at room temperature for 20 min. Finally, the aqueous solution of dye (Coumarin 343; 4.0 mg, 0.015 mmol or DAPI; 5.0 mg, 0.014 mmol) in 5 mL was added dropwise to the above RBF. The reaction mixture was stirred overnight at the room temperature, then dialyzed using a cellulose dialysis tube (with 14 kDa cut-off molecular weight) against distilled water (appx. 2 L) overnight to remove the unreacted dye molecules.

4.2.2 Device fabrication

Microchannel fabrication was carried out using conventional soft lithography techniques. Firstly, the silicon mold was fabricated. 50 µm thick SU-8 2050 photoresist (Microchem) was spin-coated onto a 4-inch silicon wafer with two steps of spinning: 55 s, 500 rpm, and 40 s, 3500 rpm followed by soft bake (2 min at 65 °C, 7 min at 95 °C, 1 min at 65 °C), UV exposure (180 mJ/cm^2), post bake (3

min at 65 °C, 7 min at 95 °C, 1 min at 65 °C), and development (5 min). Then, PDMS (Dow-corning Sylgard 184) was mixed with the curing agent at a 10:1 ratio. The mixture was degassed in a vacuum chamber, poured onto the mold, and cured on a hot plate for 5 h at 90 °C. Cured PDMS was peeled off from the mold, and 1 mm holes were punched for inlet and outlet connections. Finally, the PDMS layer (microchannel dimensions: 50 mm length, 60 µm width, 50 µm height) was plasma-bonded to a glass slide to form the microchannel.

4.2.3 Experimental Setup

Gauge 20 syringe tips (Jensen Global) were used for tubing connections. Polypropylene hubs were peeled-off from the metal tips, and the remaining stainless steel cannula was connected to 10-mm long Tygon tubing (ID: 0.796 mm), one for the inlet and another one for the outlet. High voltage DC power supply (LabSmith HVS4448-3000V) was connected to stainless steel metal tips using hook connectors. The sample flow was pumped from the inlet with a pressure pump (Elveflow OB1).

Particle migration in the microchannel was monitored with a high-speed camera (Phantom Miro e2) at 3000 fps under an inverted microscope (ZEISS Axio Vert.A1). Recorded videos were split to single frames and image-stacked to form a single photo with a MATLAB script to show the trajectory of the particles.

A Leica spectral inverted SP8 lightening confocal microscope with an automatic stage control was used for confocal microscopy imaging of the fluorescent dye-labeled PEO and HA viscoelastic solutions. For confocal imaging, 488 nm and 405 nm wavelength excitation laser was used for PEO and HA, respectively. Leica HCX PL FlLUOTAR L 20X/0.40 NA dry microscope objective was used for imaging. A galvo-resonant scanner was used for the imaging where the image scanning frequency was 200 Hz per frame, whereas the frame size or the imaging area was 512 pixels (129.0 µm; x) x 512 pixels (129.0 µm; y). The total number of 40 frames is z-stacked. The slice thickness along z was 1.56 µm, while the scanning pixel size in x and y was 0.253 µm each. The rest of the setup and experimental conditions were the same as the particle migration experiments.

4.3 Results and discussion

We studied particle migration in a microfluidic channel with the simultaneously applied pressure-driven flow and DC electric field. We suspended PS particles in three different solutions: DI water, 500 ppm PEO_{5MDa}-based viscoelastic solution, and 1000 ppm $HA_{1.5MDa}$-based viscoelastic solution. Solutions were pumped through the PDMS microchannel while DC electric field was applied simultaneously. The electric field generates electrophoretic motion due to the non-zero zeta potential of the suspended particles in each solution.

Initially, particle migration was studied for only pressure-driven flow without applying DC electric field. Then, the electric field was simultaneously applied with the pressure-driven flow; two different tests were performed by changing the direction of the electrophoretic motion of the PS particles: concurrent where the pressure-driven flow is in the same direction as the electrophoretic force and countercurrent where pressure-driven flow is in the opposite direction to the electrophoretic force. Volumetric flow rate (Q), Reynolds number (Re), and Weissenberg number (Wi) were analytically calculated from the equations given in Chapter 1. Relaxation time (λ) for dilute viscoelastic solutions was calculated using Zimm relaxation theory considering the molecular weight of the viscoelastic solutions. Molecular weight dependent Zimm relaxation time is predicted as [120],

$$\lambda_{zimm} = F\frac{[\eta]\, M_w \eta_s}{N_A k_B T} \tag{4.1}$$

where, F, η M_w, η_s, N_A, k_B, and T are front factor, intrinsic viscosity, molecular weight, solvent viscosity, Avogadro number, Boltzmann constant, and temperature, respectively.

Effective relaxation time is estimated as the following equation 4.2 [120],

$$\lambda_{eff} = 18\lambda_{zimm}\left(\frac{c}{c^*}\right)^{0.65} \tag{4.2}$$

where c and c^* are the polymer and polymer overlap concentration, respectively.

$$F = \sum_{i=1}^{\infty} \frac{1}{i^{3\nu}} \tag{4.3}$$

where $F = 0.463$ can be can be estimated from the Remann Zeta function for PEO using solvent quality exponent $\nu = 0.552$ and overlapping polymer concentration (c^*) and intrinsic viscosity ($[\eta]$) for PEO_{5MDa} are calculated using equations 2.3 and 2.5. The calculations are different for $HA_{1.5MDa}$ solutions where $F = 0.383$ using solvent quality exponent $\nu = 0.5$ [154]. Intrinsic viscosity ($[\eta]$) and overlapping polymer concentration (c^*) for are calculated using equations 4.4 and 4.5 [155],

$$[\eta]_{HA} = 0.029\, M_w^{0.80} \tag{4.4}$$

$$c^* = \frac{2.5}{[\eta]} \tag{4.5}$$

Relaxation time and shear-dependent properties of prepared solutions are tabulated in Table 4.1 and 4.2 for varying concentration of PEO and HA viscoelastic solutions.

Our experimental outputs are summarized in Fig. 4.2 to display the particle equilibrium positions at the cross section of the observation window. Under the pressure-only case, particles in DI Water show no cross-stream migration. However, particles in PEO- and HA-based viscoelastic solutions migrate to the channel center due to the elastic lift force, which pushes the particles to low shear rate regions [82, 94, 156]. In the concurrent test, particles in DI water and HA-based viscoelastic solution migrate towards the walls. However, particles in the PEO-based viscoelastic solution migrate towards the channel center. In the countercurrent test, the migration results are the opposite.

Table 4.1: Rheological properties for PEO_{5MDa} at different concentrations.

Fluid properties	50	100	500	1000	2000
η_0	0.88	0.92	1.55	2.7	7.2
c* (ppm)	0.473	0.473	0.473	0.473	0.473
$c/c*$	0.106	0.211	1.057	2.114	4.229
λ_{zimm} (ms)	1.354	1.354	1.354	1.354	1.354
λ_{eff} (ms)	5.654	8.872	25.255	39.629	62.185

Table 4.2: Rheological properties for $HA_{1.5MDa}$ at different concentrations.

Fluid properties	100	200	1000	2000	5000
η_0	4.5	7.9	48	96	430
c* (ppm)	0.988	0.988	0.988	0.988	0.988
$c/c*$	0.101	0.202	1.012	2.025	5.062
λ_{zimm} (ms)	0.522	0.522	0.522	0.522	0.522
λ_{eff} (ms)	2.122	3.33	9.478	14.873	26.982

It was reported earlier that particle migration in DI and viscoelastic solutions are opposite to each other under the same experimental conditions [147]. However, our results with HA-based viscoelastic solutions are controversial. Particle equilibrium positions in the HA-based viscoelastic solution are similar to DI. We are hypothesizing that the polyelectrolyte nature of HA is the main reason for the difference observed with PEO- and HA-based viscoelastic solutions in Electro-Viscoelastic Migration (EVM). Experimental evidence for our hypothesis is presented in the following sections.

4.3.1 Particle migration experiments

4.3.1.1 Viscoelastic flow focusing optimization in only pressure-driven flow

It is essential to observe the viscoelastic behavior of prepared viscoelastic solutions before Electro-Viscoelastic Migration (EVM) experiments to understand whether they exhibit enough elastic lift (EL) force for particle focusing under the pressure-driven flow without the electric field. Therefore pressure-only experiments are performed to find the optimal pressure for central viscoelastic focusing for both PEO and HA viscoelastic solutions in Fig. 4.4. At 50 mbar, a well-oriented single

train of particles is achieved at the center of the channel, and the viscoelastic focusing is achieved for both solutions. During our experiments in Fig. 4.4, we did not observe corner migration, and the particles only focused to the center of the channel. Dimensionless numbers and flow parameters defining the experiment are tabulated in Table 4.3 and 4.4.

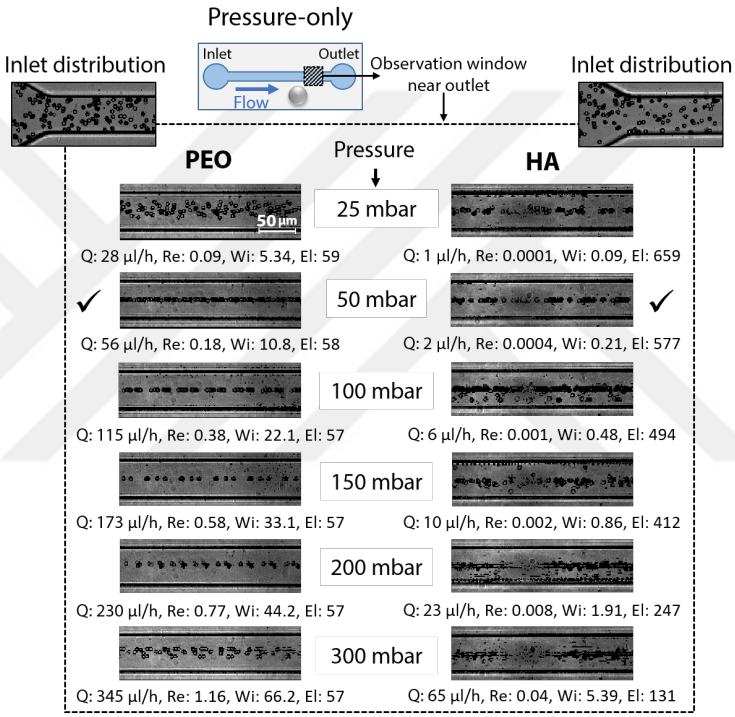


Figure 4.4: Top-view image stacked photos for viscoelastic focusing experiments with PEO- and HA-based viscoelastic solutions for varying inlet pressures. The single stream of particles in the middle of the channel indicates migration to the channel center.

4.3.1.2 Particle migration under only pressure-driven flow, concurrent, and countercurrent experiments

Figure 4.5 shows the image stacked photos from the top-view video recordings at the channel outlet for simultaneously applied pressure-driven flow and DC electric field for increasing the electric field magnitude (0-500 V/cm). In all cases, the particles are arbitrarily distributed at the channel inlet. The single stream of particles in the middle of the channel indicates migration to the channel center,

Table 4.3: Dimensionless numbers of 500 ppm PEO_{5MDa}

P (mbar)	Q (µl/h)	$\dot{\gamma}_w$	U_P (mm/s)	η (mPa.s)	Re	Wi	El
25	28	309	2.55	1.55	0.09	2.17	23.9
50	56	626	5.2	1.53	0.18	4.39	23.6
100	114	1270	10.6	1.51	0.38	8.9	23.3
150	173	1918	16	1.50	0.58	13.4	23.1
200	230	2557	21.3	1.50	0.77	17.9	23.1
300	345	3836	32	1.50	1.16	26.9	23.1

Table 4.4: Dimensionless numbers of 1000 ppm $HA_{1.5MDa}$

P (mbar)	Q (µl/h)	$\dot{\gamma}_w$	U_P (mm/s)	η (mPa.s)	Re	Wi	El
25	1	12	0.1	42	0.0001	0.03	243
50	2	27	0.25	35	0.0004	0.07	202
100	6	64	0.53	30	0.001	0.17	174
150	10	115	0.96	25	0.002	0.30	145
200	23	255	2.13	15	0.008	0.67	87
300	65	719	5.98	8	0.041	1.89	46

while the two streams at the channel edge indicate migration to the channel corners as schematically shown in Fig. 4.2. Pressure difference (P) is kept constant at 30 mbar for DI Water (Q: 58 µl/h, Re: 0.33, Wi: 0), 50 mbar for PEO (Q: 56 µl/h, Re: 0.18, Wi: 4.39, El: 23.6), and 50 mbar for HA (Q: 2 µl/h, Re: 0.0004, Wi: 0.07, El: 202) solutions. Pressure, flow rate, Re, and Wi are kept constant during these experiments.

Electrophoretic mobility is determined experimentally by tracking the motion of particles under the electric field without applying pressure-driven flow [31]. The magnitude of the electrophoretic velocity (U_{EP}) and electrophoretic mobility (μ_{EP}) for both the concurrent and countercurrent modes are 0.4 mm/s and 0.15 mm/s; $2.0 \cdot 10^{-8}$ $m^2/(V \cdot s)$ and $0.75 \cdot 10^{-8}$ $m^2/(V \cdot s)$ for PEO and HA solutions at 200 V/cm.

Three particle suspensions were prepared in DI Water, PEO-, and HA-based viscoelastic solutions. Particle migration was observed at the outlet during concurrent and countercurrent tests. The electric field magnitude was varied between 100-500 V/cm. The best focusing results are highlighted in Fig. 4.5. At 200 V/cm

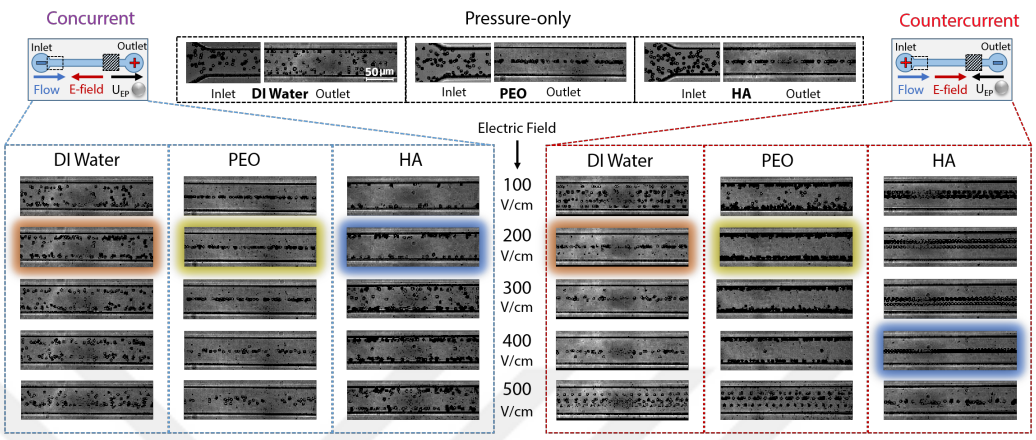


Figure 4.5: Top-view image-stacked photos of high-speed camera recordings for particle migration under pressure-driven flow and simultaneously applied pressure-driven flow and DC electric field.

concurrent experiments, particles are focused at the channel wall for DI solution, whereas they are focused at the center for the PEO solution. More interestingly, the second viscoelastic solution, HA, yielded the same results observed in the DI water medium. For each medium, the equilibrium particle positions are reversed for countercurrent experiment.

Although both viscoelastic solutions (PEO and HA) show very similar viscoelastic focusing behavior in the pressure-only regime (0 V/cm), they give opposite migration results when the electric field was applied together with the pressure-driven flow. To best of our knowledge, such an observation has not been reported so far. A comprehensive analysis of the governing forces is required to explain these intriguing results and the underlying mechanism of EVM.

4.3.2 Principle of EVM using dominant lift forces

It should be noted that PEO is a neutral polymer [157], and HA is a polyelectrolyte due to Na^+ backbones in the polymeric chain [153]. Therefore, we divided the explanation for viscoelastic solutions into two sections. In the first section, we explained the difference between the Newtonian and neutral viscoelastic solution (Fig. 4.6). In the second section, we focused on the polyelectrolyte viscoelastic solution and its similarity with Newtonian results (Fig. 4.7).

Figure 4.6 schematically explains the particle migration in Newtonian and neutral viscoelastic solutions under simultaneously applied pressure-driven flow and electric field.

4.3.2.1 Particle migration in a Newtonian medium

Pressure driven flow in a microchannel generates a quadratic velocity profile. Suspended particle in laminar flow is under the influence of this velocity profile. If an arbitrarily positioned particle is considered to be stationary relative to the fluid velocity, it experiences a different velocity magnitudes due to the shear gradient in the channel (Fig. 4.6.a) [158]. The velocity difference around the particle generates a shear gradient lift (SGL) force, which in turn pushes the particle to low velocity, high shear rate regions-channel walls. Particles are always under the effect of SGL; yet, to generate considerable migration with SGL force, high Re is required [65].

The use of the DC electric field and pressure-driven flow change the velocity of the particle relative to the fluid velocity due to the electrophoretic force acting on the particle. The additional DC electric field generates a slip velocity depending on the charge of the particle [66, 147]. The electroosmotic flow is neglected in comparison to the pressure-driven flow. In the concurrent experiment, the velocity of the particle increases relative to the fluid velocity due to the electrophoretic force. This increase is shown in Fig. 4.6.b as a slip velocity. When the slip velocity is superposed with the fluid velocity, the relative velocity difference on both sides of the particle becomes higher compared to the pressure-only case. A higher velocity difference generates higher SGL force, which pushes the particle towards the channel walls (Fig. 4.6.b). In the countercurrent experiment, the electric field, electrophoretic force, and slip velocity directions are reversed. After superposing the slip velocity and particle velocity streamlines, high and low shear rate regions flipped at the affinity of the particle; thus, the direction of SGL is also flipped, and particle migrates towards the channel center (Fig. 4.6.c).

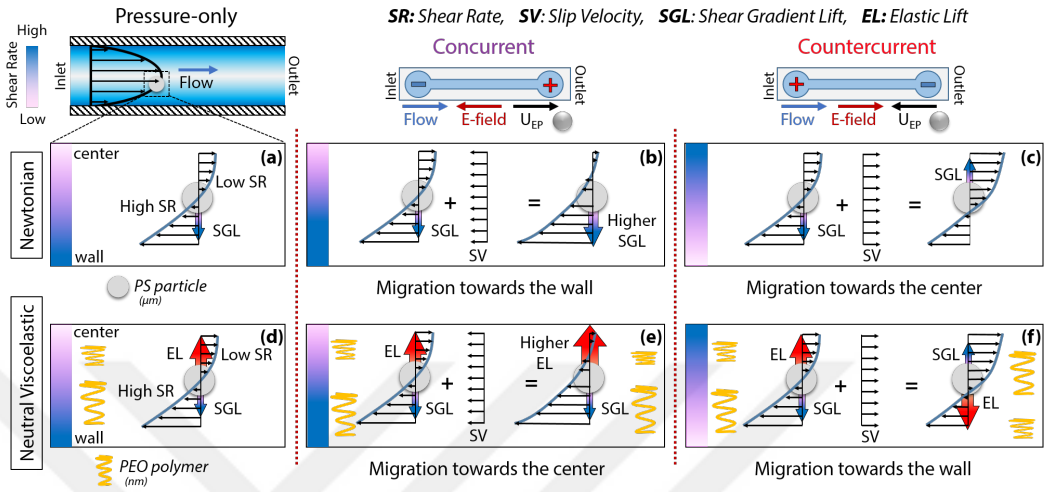


Figure 4.6: Illustrative explanation of particle migration in Newtonian and neutral viscoelastic solutions. Particle migration in Newtonian solution for (a) pressure-only, (b) concurrent, (c) countercurrent cases, in neutral viscoelastic solution for (d) pressure-only, (e) concurrent, and (f) countercurrent cases. Green spring, blue, and red arrows represent the PEO polymer stretching, shear gradient lift force, and elastic lift force, respectively. The color-chart on the left-hand side of the channel represents the shear gradient profile.

4.3.2.2 Particle migration in a neutral viscoelastic medium

In a pressure-driven flow, viscoelastic polymers are stretched along with the applied shear. The shear gradient in the channel causes a non-uniform stretching of polymers, which increases at the high shear rate as schematically shown in Fig. 4.6.d. This generates an elastic lift (EL) force on the suspended particles directing from high shear rate to low shear rate regions, from channel walls to center [82]. At low Re, SGL is negligible when compared to EL. Thus, the particle is attracted to the channel center under the pressure-only condition (Fig. 4.6.d). In the concurrent case (Fig. 4.6.e), the slip velocity enhances the shear stress around the particle and generates higher EL force directing towards the channel center [150]. In the countercurrent case, the high and low shear rate regions around the particle are reversed, which flips the polymer stretching region in the affinity of the particle. Consequently, the EL force direction is flipped, directing the particles towards the channel walls (Fig. 4.6.f).

4.3.2.3 Particle migration inside polyelectrolyte solution and non-uniform viscoelasticity generation

Under the pressure-only case, viscoelastic polymers are stretched due to local shear rate and are migrated away from the walls of the channel; yet, this migration is only observed at the proximity of the channel walls [143]. Neutral polymers are not affected (neither stretched nor migrated) by the electric field under the simultaneous use of pressure-driven flow and DC electric field. However, the cross-stream migration is observed for the polyelectrolytes such as λ-DNA (and HA in our experiment) due to the electrophoretic force-induced electro-hydrodynamic interactions (EHI) [141, 143].

We hypothesize that viscoelastic polymer concentration at the channel cross section stays uniform for neutral polymers. However, for the polyelectrolytes, the polymer concentration locally changes that generates a non-uniform viscoelastic solution distribution inside the microchannel.

Figure 4.7 schematically illustrates the development of particle migration and non-uniform viscoelasticity for the HA-based viscoelastic solution for concurrent and counter-current experiments. Initially, particles are centrally focused under the pressure-only regime where there is no electric field. In the concurrent case, HA molecules (under the influence of EHI) are progressively attracted to the channel center at the outlet. Consequently, HA polymer concentration gradually increases around the center. This starts to generate a polymer concentration gradient at the channel cross section, resulting in a more Newtonian solution at the channel walls. At the channel center, the increase in HA concentration leads to a high shear-thinning behavior. In high shear-thinning viscoelastic solutions, particles migrate towards the channel walls under pressure-driven flow [99]. High shear-thinning behavior starts to play a dominant role for the particle migration so that particles are progressively pushed away from the center. At the steady-state, particles migrate to the more Newtonian regions (walls). In the countercurrent case, the focusing trend is entirely reversed. HA polymers start to migrate toward the walls. Then, high shear-thinning behavior is developed at the corners due to the HA concentration increase. Thus, the channel center

becomes more Newtonian-like. At the steady-state, particles are focused to the channel center. This explanation clarifies the similarity of the focusing behavior in HA and Newtonian solutions as experimentally shown in Fig. 4.5.

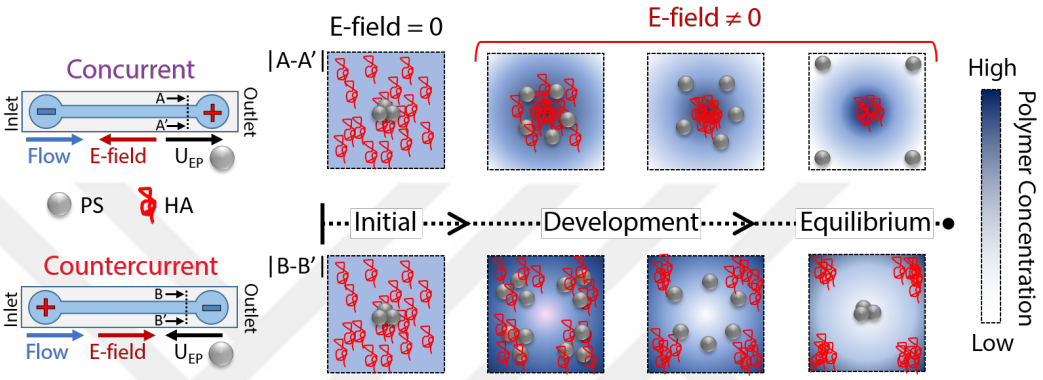


Figure 4.7: Development of particle migration in HA-based viscoelastic solutions at the outlet cross section of the channel under simultaneously applied pressure-driven flow and electric field. The blue color gradient bar represents the concentration gradient at the channel cross section. The color chart on the right represents the polymer concentration gradient.

4.4 Experimental attempts to prove the EVM hypothesis

In the previous section 4.3.1, the EVM experiments were performed in a straight square cross section microchannel. We applied a bidirectional electric field along the microchannel together with the pressure-driven flow. The anomalous migration observed for the particles in neutral and polyelectrolyte viscoelastic solutions. Even though the solutions have viscoelastic properties, they showed opposite migration behavior. We hypothesized that this difference is due to the charge of the polymer solution and provided a unifying EVM theory to explain the unusual particle migration in both viscoelastic solutions. According to EVM theory, for neutral viscoelastic solutions, polymer concentration is uniform along the microchannel. However, non-uniform polymer distribution is expected at the channel cross section for polyelectrolytes.

We have designed two different sets of experiments to prove our hypothesis.

In section 4.4.1, we fabricated 60 µm wide, 60 µm high trifurcated microchannel (one inlet, two outlets) and applied the same experimental conditions in section 4.3.1 without using suspended particles. We collected the sample solutions at the channel outlets and measured their conductivity. The polymer concentration is linearly-dependent to solution conductivity. In section 4.4.2, HA and PEO polymers are fluorescent-labeled and polymer migration investigated under the confocal microscope.

4.4.1 Measurement of polymeric concentration change via HA solution conductivity in the trifurcated channel

Figure 4.8 shows the photo of the experimental setup and illustrative drawings for concentration-dependent conductance measurements. A usual 2D hydrodynamic flow focusing chip design was used in a reverse configuration (outlet used as inlet and inlet used as outlet). Sample solution introduced from the inlet (V1) with a pressure pump and collected at the two other outlets center (V2) and walls (V3), as illustrated in 4.8.b. Volume of 50 µl sample solution is enough to measure the solution conductivity. We performed conductance measurements using an LCR meter (Keithley E4980A). Details of the measurement setup are given in Fig. 4.8.c-d. A 10 cm long Tygon tubing (ID: 0.8 mm OD: 1.5 mm) was punched with metalic sharp tips which are connected to LCR meter via BNC connectors. The distance between the tips adjusted as 2 cm (Fig. 4.8.c). The collected sample solution was put into an Eppendorf tube and introduced from one end of the tygon tubing up to the region between metal tips using negative pressure with a syringe connected to the other end of the tubing (Fig. 4.8.d). 1V bias voltage applied at 1 kHz, 10 kHz, 100 kHz, and 1 MHz. To validate if the conductance is dependent on polymer concentration, we performed conductance measurements at varying PEO $_{5\text{MDa}}$ concentrations in Figure 4.9.b. Measured polymer conductance is linearly dependent on polymer concentration. We performed the following experiments at 10 kHz.

Following this, we performed four different experiments in Fig. 4.9.d for each test modes (only-pressure-driven flow, concurrent and countercurrent) with 0.1% w/v HA-based viscoelastic solution at 300 mbar inlet pressure. 1 V bias voltage

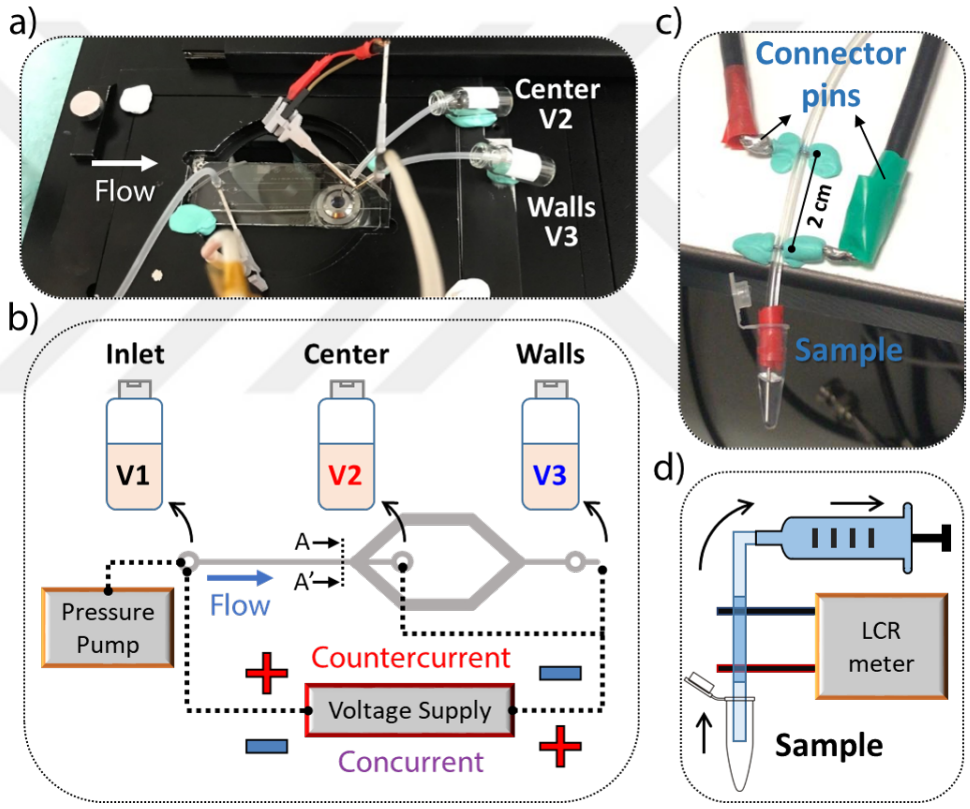


Figure 4.8: Concentration vs conductance measurements to validate polymer migration in HA viscoelastic solution with EVM theory. (a) a photo, and (b) illustrative drawing of sample collection trifurcated chip, (c) a photo, and (d) illustrative drawing of the measurement setup.

applied at 10 kHz frequency. According to EVM theory, it is expected to observe equal polymer concentration for the samples of V1, V2, and V3 at only pressure-driven-flow mode. In the concurrent mode (countercurrent), we expect to observe higher polymeric concentration at the channel center-V2 (walls-V3). Figure 4.9.c shows the earlier predictions for non-uniform polymer gradient at the channel cross section A-A. Our experimental results in Fig. 4.9.d are in a good correlation with our theory, yet further experimental observations required due to high SD values.

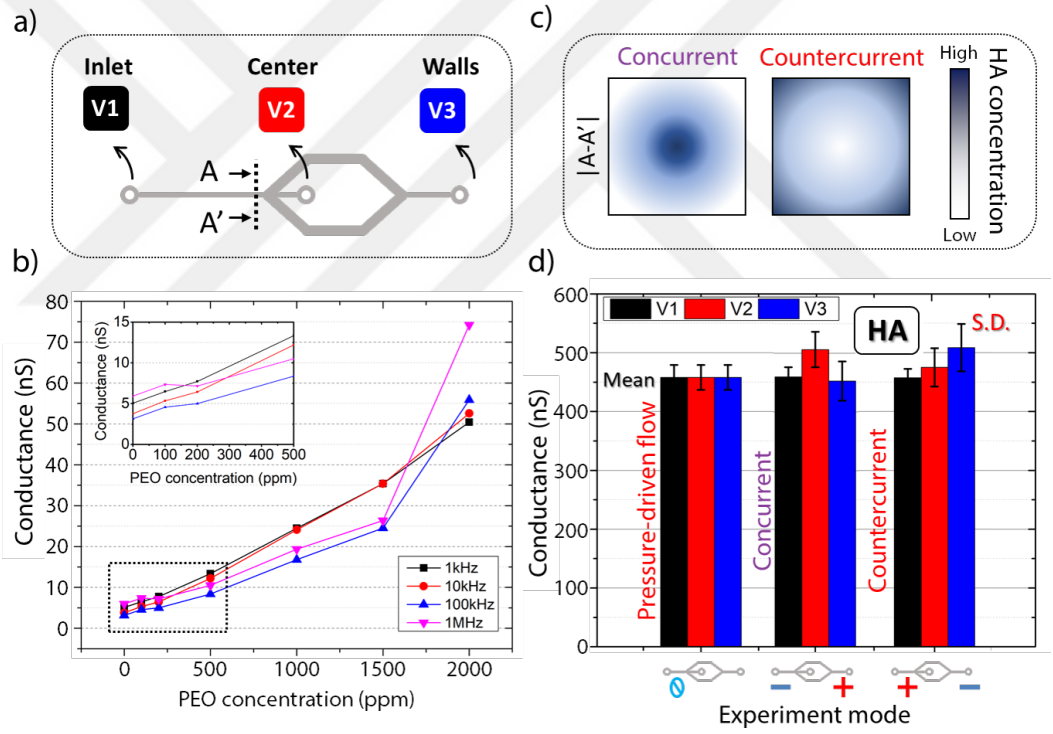


Figure 4.9: Illustrative drawing explaining the polymer migration experiments. (a) Trifurcated chip, (b) Characterization of conductance-based concentration measurement system for varying concentration of PEO samples, (c) An illustrative drawing as a reminder of how polymer migration occurs at the channel cross section for each test modes, and (d) Average of 4 different concentration vs conductance measurement results for HA viscoelastic solutions at only pressure-driven-flow, concurrent, and countercurrent test modes.

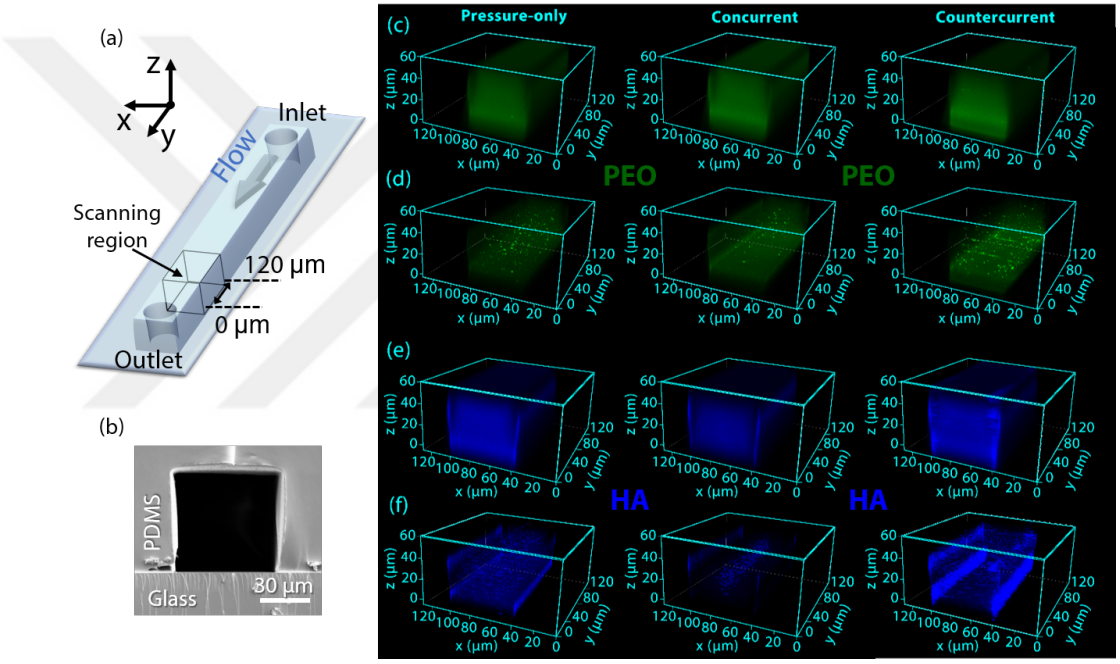


Figure 4.10: Confocal imaging results for uniform and non-uniform concentration distribution of fluorescently tagged viscoelastic solutions at the channel cross section near the outlet. Polymers are observed in three different modes: pressure-only, concurrent, and countercurrent. The applied electric field is 200 V/cm for the concurrent and countercurrent modes. (a) Schematic drawing of the channel and scanning volume. Confocal scanning region is 60 x 120 x 120 μm^3.(b) Scanning electron microscope (SEM) of the channel cross section (c-d) Coumarin 343 tagged-PEO, and (e-f) DAPI tagged-HA.

4.4.2 Confocal imaging experiments of the fluorescent dye-labeled polymer viscoelastic solutions

To evidentially prove and experimentally confirm our hypothesis, we labeled PEO and HA with fluorescent dyes, Coumarin 343 and DAPI, respectively.

The fluorescently-labeled PEO and HA viscoelastic solutions were used to show polymer distribution change for EVM along the flow axis (Fig. 4.10.a). Confocal microscope images are given in Fig. 4.10.c-f. We mapped the fluorescent intensity change in Fig. 4.10.c and 4.10.e. Even if we can observe the intensity change for each experimental mode, the concentration gradient at the channel cross section is not well pronounced in these plots. Thus, in Fig. 4.10.d and 4.10.f, we performed gamma correction correction and maximum intensity threshold on the corresponding fluorescent images to show the concentration gradient more clear. In this way, low intensity regions are automatically filtered out, and overall contrast is enhanced in Fig. 4.10.e and 4.10.f.

Additionally, a maximum intensity projection method was used for visualization of z-stacked (40 frames in total) 3D confocal images as single 2D images ((Fig. 4.11.a and 4.11.b). Then fluorescent intensity profile across the channel cross section was calculated (Fig. 4.11.c and 4.11.d). 100 µm long straight line was drawn to define the region of interest (ROI) for intensity plots. Polymer migration is clearly observed from the projection images and intensity plots for HA experiment; however, no polymer migration was observed in PEO.

The uniformity of Coumarin tagged-PEO polymer concentration is uniform at the channel cross section near the outlet regardless of the presence or the direction of the electric field in Fig. 4.10.c and 4.10.d due to the electrically neutral nature of PEO. Figure 4.10.e-f demonstrate migration behavior for DAPI tagged-HA solution at the channel cross section near the outlet. In contrast to the PEO case, HA molecules respond to the changes in the electric field. When no electric field is applied (pressure-only mode), the polymer distribution is uniform at the cross section. In the concurrent mode, HA polymers migrate from walls to the channel center, showing higher fluorescence intensity at the center. In the

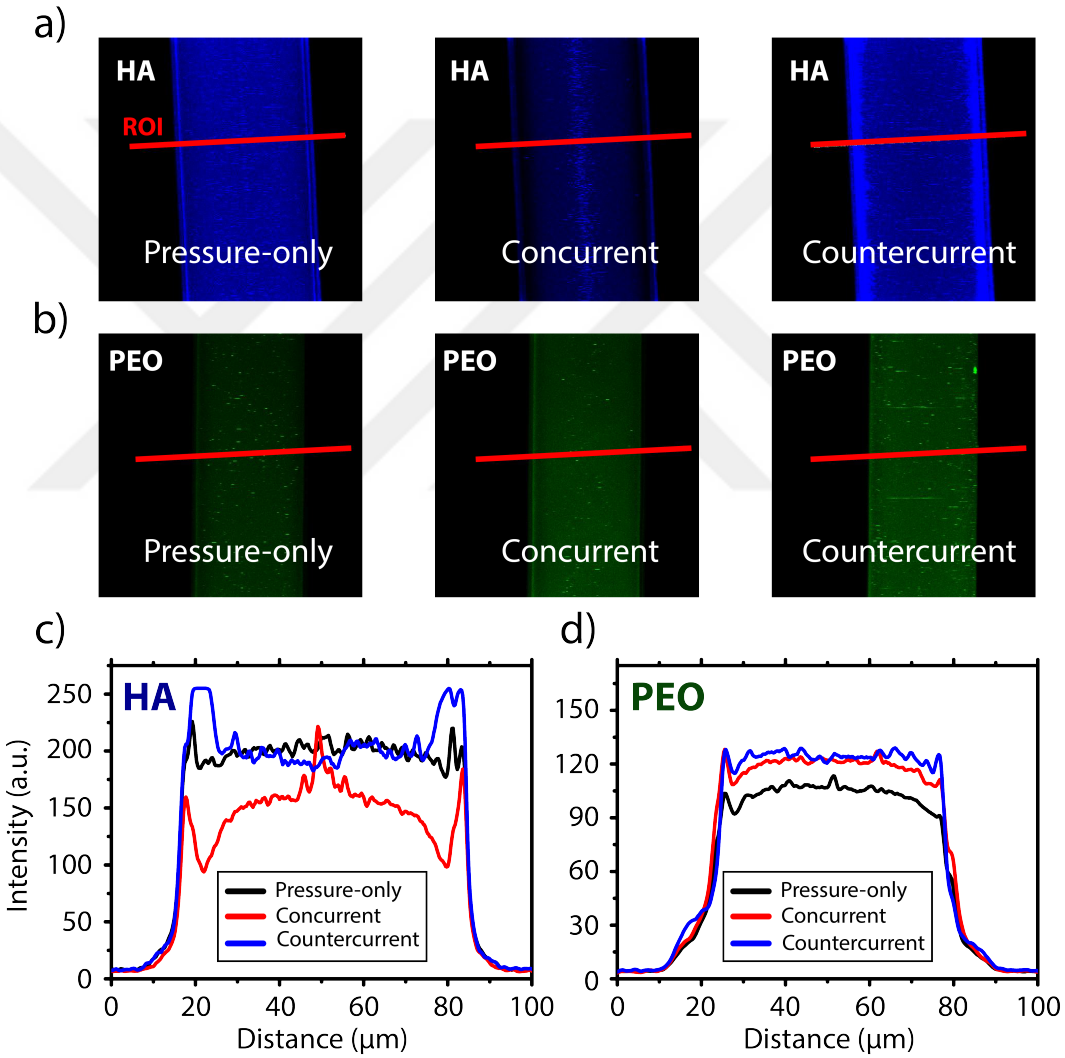


Figure 4.11: 2D maximum intensity projection images for (a) HA, (b) PEO and intensity plots for (c) HA, and (d) PEO.

counter-current mode, polymers are highly populated near the channel corners (walls). Non-uniform polymer distributions in different modes at the channel cross section are due to the polyelectrolyte nature of HA molecules. The confocal observations on the behavior of molecules are in parallel with the experimental results in Fig. 4.5, and our hypothesis is schematically shown in Fig. 4.7.

4.4.3 EVM for varying viscoelastic polymer concentrations

The experimental observations and EVM explained in the previous sections are performed at a specific polymer concentration ratio $c/c^* = 1$, where c is the polymeric concentration in solution, and c^* is the overlap concentration. The viscoelastic solution is considered to be semi-dilute if $c \geq c^*$, where polymer coils start to overlap, and entanglement fluctuations occur [53, 54].

Elastic lift force, which is a function of polymer concentration, plays a crucial role in viscoelastic particle focusing. Hence, it is critical to investigate the viscoelastic polymer concentration dependence of EVM. To support the underlying mechanism for neutral PEO and polyelectrolyte HA viscoelastic solutions, we define two types of EVM, based on the charge of the viscoelastic solution: Neutral-EVM (Neu-EVM) and Polyelectrolyte-EVM (Ply-EVM).

We demonstrate the effect of polymeric concentration on the equilibrium particle positions at the channel outlet under simultaneously applied pressure-driven flow and DC electric field in Fig. 4.12. Three regimes, $c/c^* > 1$; $c/c^* = 1$; $c/c^* < 1$, are considered by changing the polymer concentration of PEO and HA viscoelastic solutions. Dimensionless numbers and flow parameters defining the experiment are tabulated in Table 4.5 and 4.6.

Neu-EVM in PEO experiments yielded an exciting transition depending on the polymer concentration ratio. When $c/c^* < 1$, the equilibrium particle positions were reversed, which are similar to the Newtonian solution (as shown in Fig. 4.5). However, Ply-EVM in HA experiments showed that particle equilibrium positions did not change at varying polymer concentration ratios.

Table 4.5: Dimensionless numbers of varying concentration PEO_{5MDa}

c (ppm)	P (mbar)	Q (µl/h)	$\dot{\gamma}_w$	U_P (mm/s)	η (mPa.s)	Re	Wi	El
50	25	47	527	4.39	0.91	0.26	0.83	3.14
100	25	45	504	4.2	0.95	0.24	1.24	5.15
500	50	56	626	5.2	1.53	0.18	4.39	23.6
1000	100	75	833	6.9	2.3	0.16	9.18	55.7
2000	200	69	767	6.4	5	0.07	13.2	190

Table 4.6: Dimensionless numbers of varying concentration $HA_{1.5MDa}$

c (ppm)	P (mbar)	Q (µl/h)	$\dot{\gamma}_w$	U_P (mm/s)	η (mPa.s)	Re	Wi	El
100	50	32	355	2.96	2.7	0.06	0.21	3.5
200	100	43	480	4	4	0.054	0.44	8.1
1000	250	27	300	2.5	16	0.01	0.79	92
2000	600	47	523	4.36	22	0.011	2.16	200
5000	1200	23	255	2.13	90	0.001	1.92	1484

These experiments show the significant difference between the mechanisms of Neu-EVM and Ply-EVM. In Neu-EVM migration profile is dictated by the forces effective on the suspended particles. The uniform neutral polymer concentration profile is preserved throughout the microchannel. Hence lowering the polymeric concentration below c*, $c/c^* < 1$, dramatically decreases the elastic lift force leading to opposite migration results in Fig. 4.12. On the other hand, Ply-EVM is based on polyelectrolyte migration creating a Newtonian medium profile in the channel cross section. This profile is equivalent to the co-flow of Newtonian and viscoelastic mediums. In the equilibrium state, suspended particles migrate to Newtonian regions. Thus the Ply-EVM results shown in Fig. 4.12 are independent of polymer concentration for the range studied in this work.

4.4.4 Enhanced viscoelastic migration in Neu-EVM for central 3D particle focusing cytometry applications

Precise control of particle position and central alignment are crucial for cytometry applications. We have demonstrated passive manipulation of particles via

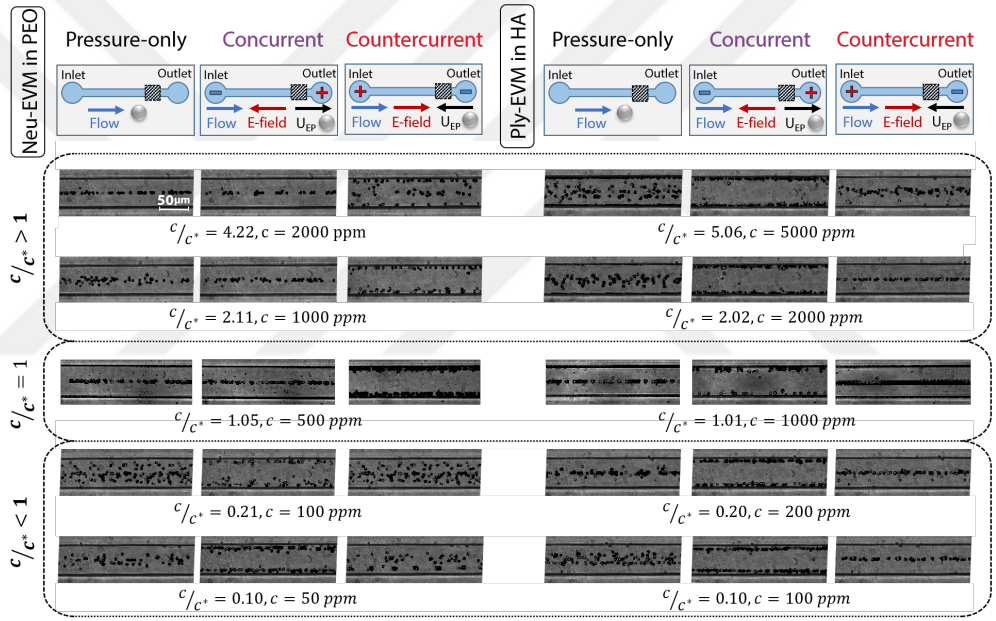


Figure 4.12: Top-view image-stacked photos of high-speed camera recordings to show the effect of polymeric concentration on particle equilibrium positions at the channel outlet for Neu-EVM and Ply-EVM in pressure-only, concurrent and countercurrent tests. The electric field is applied at 200 V/cm. c^*_{PEO} =473 ppm and c^*_{HA}=988 ppm.

viscoelastic focusing technique and showed two proof-of-concept cytometry applications in Chapter 2 and 3. The suspended particles must travel at least 3-4 cm distance along the channel to develop enough elastic lift force and generate a single-file of particle trajectory at the channel center. Here we introduced EVM theory and showed that the slip velocity enhances the shear stress around the particle. In the concurrent Neu-EVM (Fig. 4.6.e) mode, higher EL force directing the particles towards the channel center and provides faster focusing in a shorter travel distance.

Figure 4.13 shows the effect of electric field magnitude on the EVM and particle stream width in concurrent Neu-EVM of PEO-based viscoelastic solution at 1 cm, 2 cm, and 4 cm distances from the inlet. Rectangular bars in the figure represent the particle stream width at 1 cm (black), 2 cm (red), and 4 cm (blue). Top view high-speed camera video recordings are image stacked to a single frame at each electric field value; then, the particle stream width is approximated from the images. Graph y-axis represents the channel width of 60 µm. Pressure difference was kept constant at 50 mbar for the particle suspension in PEO viscoelastic solution. When electric field was increased up to 200 V/cm, we observed viscoelastic migration enhancement. The central particle stream width decreased down to a single particle trajectory. At 0 V/cm, 4 cm distance was required to reach the narrowest particle trajectory of 12 µm with viscoelastic focusing. However, at 200 V/cm, it was possible to reach 7 µm single-particle stream width at 1 cm distance from the inlet.

Figure 4.14 shows the effect of electric field magnitude on the particle distribution at the cross section of microchannel for concurrent Neu-EVM of PEO-based viscoelastic solution. Y-position indicates the location of the particle at the y-axis. Standard deviation at each electric field magnitude is given above the whiskers. Only in viscoelastic focusing (at 0 V/cm), the lowest possible SD was 1.00 at 4 cm. Applying the electric field under the concurrent case of Neu-EVM mode improved the central particle focusing and decreased the SD values. Particles were able to focus to the channel center at 2 cm with the lowest SD value (0.57) at 200 V/cm electric field.

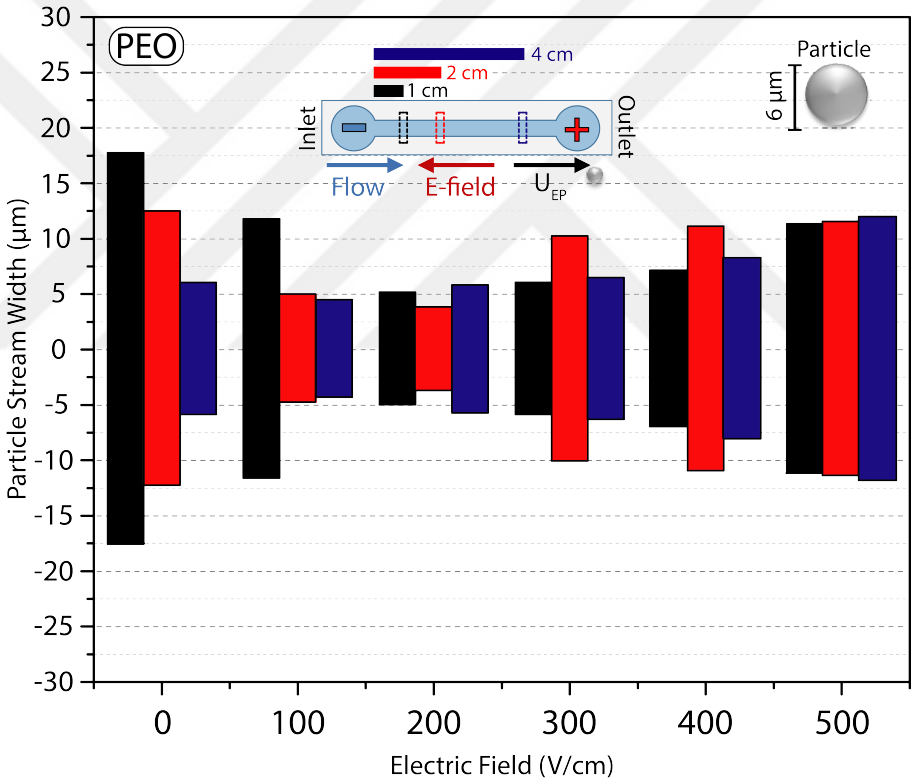


Figure 4.13: Particle stream width versus electric field at different particle travel distances in the concurrent case of Neu-EVM mode.

These outcomes prove that Neu-EVM has dramatic improvements in central particle focusing and beneficial for cytometry applications.

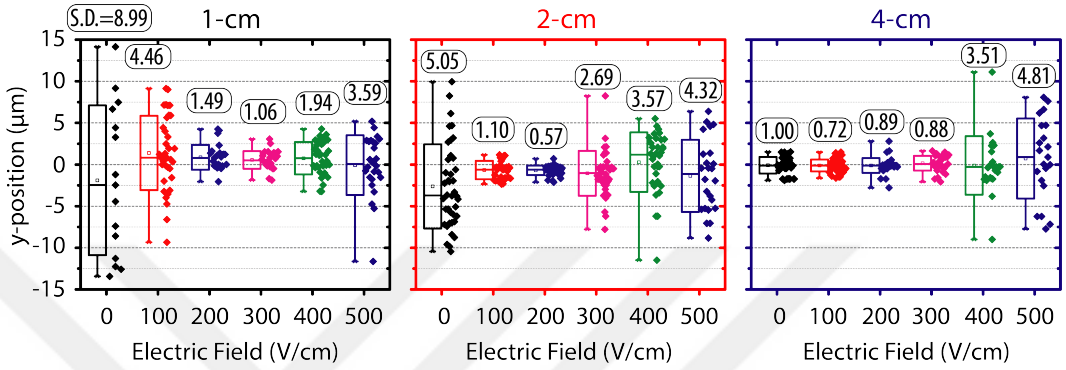


Figure 4.14: Particle distribution at the channel cross section versus electric field at different particle travel distances in concurrent case of Neu-EVM mode. For each bar graph, the square represents the mean value, the box represents the standard deviation (S.D.), and the whisker lines represent the 99% to 1% population of the counted events.

4.5 Conclusion

This study demonstrates bi-directional particle migration under simultaneously applied pressure-driven flow and electric field in Newtonian, PEO neutral viscoelastic and HA polyelectrolyte viscoelastic solutions. When the direction of pressure-flow and electrophoretic force are concurrent, particles migrate towards the channel walls in Newtonian and HA solutions and towards the channel center in PEO solution. Surprisingly, particles in HA polyelectrolyte viscoelastic solution exhibit a similar migration profile to the ones in the Newtonian solution. Even though HA and PEO polymers have similar viscoelastic properties, they show opposite migration profiles as a response to applied electric fields. To explain such behavior we introduce the Electro-Viscoelastic Migration (EVM) theory, which takes viscoelastic polymer charges into account.

Confocal imaging of fluorescent stained PEO and HA-based viscoelastic solutions demonstrates that in neutral viscoelastic solutions (Neu-EVM), the electric field does not induce polymer migration and modulates the elastic lift force. In

contrast, in polyelectrolyte viscoelastic solutions (Ply-EVM), the electric field induces migration for polyelectrolytes, the direction of which depends on the polarity of the electric field. As a result of polyelectrolyte migration, a cross-sectional polymer concentration gradient is generated at the microchannel.

To further investigate the difference between Neu-EVM and Ply-EVM, we performed migration experiments at varying polymeric concentrations. Particle equilibrium positions show a concentration-dependent results for Neu-EVM when $c/c^* < 1$. However, in Ply-EVM, particle equilibrium positions are similar to the results in the Newtonian solution, and a polymer concentration-independent migration profile is obtained. These results lead to a unifying EVM theory, explaining the particle migration results in simultaneously applied pressure-driven flow and electric field. We present the fundamental understanding and explain the particle migration behavior in most commonly used carrier fluids, Newtonian, neutral viscoelastic, and polyelectrolyte viscoelastic solutions.

Implementation of EVM theory in microfluidics presents an opportunity in developments of various fields:

- EVM can provide a good environment to study the elastic instabilities in complex fluids for different viscoelastic solutions at varying Re and Wi numbers [133, 159].

- Dilute to semi-dilute crossover regime, c^*, of polymer solutions can be detected in Neu-EVM by monitoring the particle equilibrium positions.

- EVM enhances the center viscoelastic focusing at a smaller distance in the microchannel.

- Ply-EVM gives a focusing profile independent of polymer concentration. Its implementation in microfluidic flow cytometry can provide a better 3D particle focusing [7, 102].

- Cells, polyelectrolytes, DNA, biopolymers, and proteins in a complex medium such as whole blood or biological serums can be precisely focused

and separated according to their charge and polymeric size for electrophoresis or chromatography applications [151].

Chapter 5

Summary and Future outlook

5.1 Summary

Living beings are made of cells. Human body has around two hundred different types of cells and twenty different types of subcellular components within these cells. The number, type, or role of a specific cell and cell components give the information related to natural or abnormal changes and diseases in the body. Thus the enumeration and detection of cellular and subcellular components have vital importance for human life. Flow cytometry is one of the dominant technology used for today's need on the diagnostics [160–163], biotechnology [164], and material science [165–167] with multi-parametric analysis at a single particle precision and high accuracy.

The global market of flow cytometry is mainly driven by research institutes, hospitals, clinical laboratories, pharmaceutical industry, and biotechnology companies. The demand for the use of clinical flow cytometry is intensively growing and estimated to reach $6.4 billion by the end of 2025 [42]. The evolution of tandem-flow cytometry technologies is one of the critical features for the future of flow cytometry. Integrated flow cytometry systems using multiple detection units, and the adoption of novel features will make it possible to reduce the production cost for future flow cytometers for emerging economics and research

facilities.

This thesis provides two primary outcomes.

(I) Critical improvements for flow cytometry devices using microfluidics technology and their integration with recently trending, viscoelastic passive particle focusing technique for three types (optical, impedance, and imaging) of flow cytometry methods.

Microfluidic systems provide accurate and high throughput characterization of cell with small sample footprints [11]. Viscoelastic focusing addresses the need for a single train particle trajectory for optical- and impedance-based cytometry systems. Obtaining a single stable orientation for spherical and non-spherical particles provide remarkable differences from other particle focusing techniques. Also, viscoelastic particle focusing is a passive method and can easily be adapted to any flow cytometry method. Thus, it is a powerful tool for integration with tandem-flow cytometry technologies.

We devised a palm-sized, optical flow cytometry system composed of optical fibers and a straight glass capillary using viscoelastic focusing method. Laser source and detectors are fiber-coupled, and the entire system is portable. Thanks to its simplicity and promising performance compared to commercial flow cytometry systems, the presented system can have a wide range of uses in microfluidic cytometry applications. We have assessed the effect of ionic buffer concentration in different viscoelastic solutions and provided an optimized solution suitable for the impedance flow cytometry system. We showed that it is possible to reach parachute shape single RBC orientation, which is very critical in cytometry applications to get low signal variations for a range of flow rates.

(II) A unifying Electro-Viscoelastic Migration (EVM) theory, explaining the anomalous particle migration induced by electrophoretic slip velocity results in simultaneously applied pressure-driven flow and electric field in microfluidic flows. We present the fundamental understanding and explain the particle migration behavior for most commonly used carrier fluids, Newtonian, neutral viscoelastic,

and polyelectrolyte viscoelastic solutions. We provided our unifying explanation considering the direction, and magnitude of the electric field, polymeric concentration, and charge of the carrier viscoelastic solution.

We have demonstrated that in neutral viscoelastic solutions (Neu-EVM), the electric field only modulates the elastic lift force and does not induce polymer migration. In contrast, in polyelectrolyte viscoelastic solutions (Ply-EVM), the electric field induces migration of polyelectrolytes, the direction of which depends on the polarity of the electric field. As a result of polyelectrolyte migration, a cross-sectional polymer concentration gradient is generated at the microchannel.

5.2 Future outlook

The future is not far from the checking the status of disease and generating diagnostic information with globally accessible, low-cost, and personal point of care blood counting devices like blood sugar tests.

In this thesis, we achieved successful demonstrations of flow cytometry applications using viscoelastic focusing technique. However, each cytometry methods implemented individually without using their mutual benefits in tandem configuration. Viscoelastic focusing technique provides common denominator to all cytometry methods in terms of reaching a single particle trajectory. Thus, it would be beneficial to implement the technique in a tandem configuration, for instance, combination of impedance and optical flow cytometry with PEO-based viscoelastic focusing technique.

Viscoelastic solutions are advantageous to use in microfluidic flow cytometry applications since they can support multiple benefits, such as particle focusing, separation, isolation, and enrichment in the same microfluidic environment by only changing rheological properties of fluid or flow conditions. Nevertheless, the requirement of long channel distance to develop enough elastic lift force and being obliged to use a viscoelastic suspension solution may be considered as the drawbacks of the technique. The solution for the latter case is using buffer exchange or bifurcated inlets [100]. As a solution for the former case, the EVM method can

provide central viscoelastic focusing at four times shorter distance. Therefore, EVM technique can be implemented in shorter microchannels compared to pure viscoelastic focusing flow cytometers.

Implementation of EVM in polyelectrolyte solutions can generate a non-uniform polymer concentration gradient across the channel. This will open the way for novel numerical and experimental applications to study the elastic instabilities in complex fluids at varying flow conditions.

Neu-EVM gives polymer concentration-dependent particle migration. Therefore this technique provides a new dimension to control the equilibrium position of particles by only changing the concentration of neutral viscoelastic solutions. It is also possible to understand whether the polymeric solution is dilute or semi-dilute by only monitoring the particle equilibrium positions.

In 2019, globally spread coronavirus pandemic, COVID-19 showed that our technological developments are far from providing globally available time- and cost-efficient accurate measurement tools. Therefore, development of novel technologies are also required for focusing, isolation, separation, and enrichment of genomic length species, such as DNA, without sacrificing the accuracy. Technological developments are required for cost- and time-effective genetic sequencing techniques. Microfluidic applications demonstrated DNA sequencing and enrichment applications, yet they have a long way to go for reaching the level of resolution of gel electrophoresis techniques [142]. With implementing EVM technique in a single microfluidic cartridge, it is possible to precisely focus and separate cells, polyelectrolytes, DNA fractions, and proteins according to their charge and size with a comparable resolution and measurement speed, as a replacement for electrophoresis or chromatography applications.

Bibliography

[1] J. P. Golden, J. S. Kim, J. S. Erickson, L. R. Hilliard, P. B. Howell, G. P. Anderson, M. Nasir, and F. S. Ligler, "Multi-wavelength microflow cytometer using groove-generated sheath flow," *Lab on a Chip*, vol. 9, no. 13, pp. 1942–1950, 2009.

[2] A. A. Nawaz, R. H. Nissly, P. Li, Y. Chen, F. Guo, S. Li, Y. M. Shariff, A. N. Qureshi, L. Wang, and T. J. Huang, "Immunological analyses of whole blood via "microfluidic drifting" based flow cytometric chip," *Annals of biomedical engineering*, vol. 42, no. 11, pp. 2303–2313, 2014.

[3] A. Bayram, M. Serhatlioglu, B. Ortac, S. Demic, C. Elbuken, M. Sen, and M. E. Solmaz, "Integration of glass micropipettes with a 3d printed aligner for microfluidic flow cytometer," *Sensors and Actuators A: Physical*, vol. 269, pp. 382–387, 2018.

[4] M. Frankowski, N. Bock, A. Kummrow, S. Schädel-Ebner, M. Schmidt, A. Tuchscheerer, and J. Neukammer, "A microflow cytometer exploited for the immunological differentiation of leukocytes," *Cytometry Part A*, vol. 79, no. 8, pp. 613–624, 2011.

[5] J. Guo, X. Liu, K. Kang, Y. Ai, Z. Wang, and Y. Kang, "A compact optofluidic cytometer for detection and enumeration of tumor cells," *Journal of Lightwave Technology*, vol. 33, no. 16, pp. 3433–3438, 2015.

[6] X. Mao, A. A. Nawaz, S.-C. S. Lin, M. I. Lapsley, Y. Zhao, J. P. McCoy, W. S. El-Deiry, and T. J. Huang, "An integrated, multiparametric flow cytometry chip using "microfluidic drifting" based three-dimensional hydrodynamic focusing," *Biomicrofluidics*, vol. 6, no. 2, p. 024113, 2012.

[7] M. Serhatlioglu, M. Asghari, M. Tahsin Guler, and C. Elbuken, "Impedance-based viscoelastic flow cytometry," *Electrophoresis*, vol. 40, no. 6, pp. 906–913, 2019.

[8] M. Serhatlioglu, C. Elbuken, B. Ortac, and M. E. Solmaz, "Femtosecond laser fabrication of fiber based optofluidic platform for flow cytometry applications," in *Optical Fibers and Sensors for Medical Diagnostics and Treatment Applications XVII*, vol. 10058, p. 100580I, International Society for Optics and Photonics, 2017.

[9] I. Schmid, *Flow Cytometry: Recent Perspectives*. BoD–Books on Demand, 2012.

[10] BDBiosciences, "Research cell analyzers." `https://www.bdbiosciences.com/en-sg/instruments/research-instruments/research-cell-analyzers`, 2020. Accessed: 20020-04-01.

[11] A. Vembadi, A. Menachery, and M. A. Qasaimeh, "Cell cytometry: review and perspective on biotechnological advances," *Frontiers in bioengineering and biotechnology*, vol. 7, 2019.

[12] D. V. Voronin, A. A. Kozlova, R. A. Verkhovskii, A. V. Ermakov, M. A. Makarkin, O. A. Inozemtseva, and D. N. Bratashov, "Detection of rare objects by flow cytometry: Imaging, cell sorting, and deep learning approaches," *International Journal of Molecular Sciences*, vol. 21, no. 7, p. 2323, 2020.

[13] J. Chen, C. Xue, Y. Zhao, D. Chen, M.-H. Wu, and J. Wang, "Microfluidic impedance flow cytometry enabling high-throughput single-cell electrical property characterization," *International journal of molecular sciences*,

vol. 16, no. 5, pp. 9804–9830, 2015.

[14] X. Cheng, D. Irimia, M. Dixon, K. Sekine, U. Demirci, L. Zamir, R. G. Tompkins, W. Rodriguez, and M. Toner, "A microfluidic device for practical label-free cd4+ t cell counting of hiv-infected subjects," *Lab on a Chip*, vol. 7, no. 2, pp. 170–178, 2007.

[15] M. J. Crow, S. M. Marinakos, J. M. Cook, A. Chilkoti, and A. Wax, "Plasmonic flow cytometry by immunolabeled nanorods," *Cytometry Part A*, vol. 79, no. 1, pp. 57–65, 2011.

[16] T. Sun and H. Morgan, "Single-cell microfluidic impedance cytometry: a review," *Microfluidics and Nanofluidics*, vol. 8, no. 4, pp. 423–443, 2010.

[17] W. H. Coulter, "Means for counting particles suspended in a fluid," Oct. 20 1953. US Patent 2,656,508.

[18] O. Saleh and L. Sohn, "Quantitative sensing of nanoscale colloids using a microchip coulter counter," *Review of Scientific Instruments*, vol. 72, no. 12, pp. 4449–4451, 2001.

[19] J. Guo, T. S. Pui, A. R. A. Rahman, and Y. Kang, "Numerical investigation of the performance of coultercounter with novel structure," *International Journal of Information and Electronics Engineering*, vol. 2, no. 6, p. 885, 2012.

[20] S. K. Kulp, Y.-T. Yang, C.-C. Hung, K.-F. Chen, J.-P. Lai, P.-H. Tseng, J. W. Fowble, P. J. Ward, and C.-S. Chen, "3-phosphoinositide-dependent protein kinase-1/akt signaling represents a major cyclooxygenase-2-independent target for celecoxib in prostate cancer cells," *Cancer research*, vol. 64, no. 4, pp. 1444–1451, 2004.

[21] E. Van der Pol, F. Coumans, Z. Varga, M. Krumrey, and R. Nieuwland, "Innovation in detection of microparticles and exosomes," *Journal of Thrombosis and Haemostasis*, vol. 11, pp. 36–45, 2013.

[22] D. Holmes and H. Morgan, "Single cell impedance cytometry for identification and counting of cd4 t-cells in human blood using impedance labels," *Analytical chemistry*, vol. 82, no. 4, pp. 1455–1461, 2010.

[23] U. Hassan and R. Bashir, "Electrical cell counting process characterization in a microfluidic impedance cytometer," *Biomedical microdevices*, vol. 16, no. 5, pp. 697–704, 2014.

[24] Y. Wu, J. D. Benson, and M. Almasri, "Micromachined coulter counter for dynamic impedance study of time sensitive cells," *Biomedical microdevices*, vol. 14, no. 4, pp. 739–750, 2012.

[25] J. Zhe, A. Jagtiani, P. Dutta, J. Hu, and J. Carletta, "A micromachined high throughput coulter counter for bioparticle detection and counting," *Journal of Micromechanics and Microengineering*, vol. 17, no. 2, p. 304, 2007.

[26] S. Zheng, M. Liu, and Y.-C. Tai, "Micro coulter counters with platinum black electroplated electrodes for human blood cell sensing," *Biomedical microdevices*, vol. 10, no. 2, pp. 221–231, 2008.

[27] K. C. Cheung, M. Di Berardino, G. Schade-Kampmann, M. Hebeisen, A. Pierzchalski, J. Bocsi, A. Mittag, and A. Tárnok, "Microfluidic impedance-based flow cytometry," *Cytometry Part A*, vol. 77, no. 7, pp. 648–666, 2010.

[28] S. Gawad, L. Schild, and P. Renaud, "Micromachined impedance spectroscopy flow cytometer for cell analysis and particle sizing," *Lab on a Chip*, vol. 1, no. 1, pp. 76–82, 2001.

[29] D. Holmes, D. Pettigrew, C. H. Reccius, J. D. Gwyer, C. van Berkel, J. Holloway, D. E. Davies, and H. Morgan, "Leukocyte analysis and differentiation using high speed microfluidic single cell impedance cytometry," *Lab on a Chip*, vol. 9, no. 20, pp. 2881–2889, 2009.

[30] B. J. Bain, *Blood cells: a practical guide*. John Wiley & Sons, 2014.

[31] H. E. Ayliffe, A. B. Frazier, and R. Rabbitt, "Electric impedance spectroscopy using microchannels with integrated metal electrodes," *Journal of Microelectromechanical systems*, vol. 8, no. 1, pp. 50–57, 1999.

[32] K. Cheung, S. Gawad, and P. Renaud, "Impedance spectroscopy flow cytometry: On-chip label-free cell differentiation," *Cytometry Part A*, vol. 65, no. 2, pp. 124–132, 2005.

[33] A. C. Lohman, I. Van Rijn, C. L. Lindhardt, R. Vonthein, D. Rades, and N. H. Holländer, "Preliminary results from a prospective study comparing white blood cell and neutrophil counts from a laboratory to those measured with a new device in patients with breast cancer," *in vivo*, vol. 32, no. 5, pp. 1283–1288, 2018.

[34] B. K. McKenna, J. G. Evans, M. C. Cheung, and D. J. Ehrlich, "A parallel microfluidic flow cytometer for high-content screening," *Nature methods*, vol. 8, no. 5, p. 401, 2011.

[35] Y. Song, D. Cheng, and L. Zhao, *Microfluidics: Fundamentals, Devices, and Applications*. John Wiley & Sons, 2018.

[36] G. M. Whitesides, "The origins and the future of microfluidics," *Nature*, vol. 442, no. 7101, pp. 368–373, 2006.

[37] A. Manz, N. Graber, and H. á. Widmer, "Miniaturized total chemical analysis systems: a novel concept for chemical sensing," *Sensors and actuators B: Chemical*, vol. 1, no. 1-6, pp. 244–248, 1990.

[38] D. J. Harrison, A. Manz, Z. Fan, H. Luedi, and H. M. Widmer, "Capillary electrophoresis and sample injection systems integrated on a planar glass chip," *Analytical chemistry*, vol. 64, no. 17, pp. 1926–1932, 1992.

[39] D. R. Reyes, D. Iossifidis, P.-A. Auroux, and A. Manz, "Micro total analysis systems. 1. introduction, theory, and technology," *Analytical chemistry*, vol. 74, no. 12, pp. 2623–2636, 2002.

[40] GrandViewResearch, "Microfluidics market size, share, global industry report, 2020-2027." `https://www.grandviewresearch.com/industry-analysis/microfluidics-market`, 2019. Accessed: 20020-03-20.

[41] Abbott, "Products and innovation." `https://www.abbott.com/corpnewsroom/product-and-innovation/detect-covid-19-in-as-little-as-5-minutes.html`, 2020. Accessed: 20020-04-01.

[42] Markets and Markets, "Flow cytometry market global forecasts to 2025." `https://www.marketsandmarkets.com/Market-Reports/flow-cytometry-market-65374584`, 2019. Accessed: 20020-03-20.

[43] S. H. Cho, J. M. Godin, C.-H. Chen, W. Qiao, H. Lee, and Y.-H. Lo, "Recent advancements in optofluidic flow cytometer," *Biomicrofluidics*, vol. 4, no. 4, p. 043001, 2010.

[44] N. Verellen, D. Vercruysse, V. Rochus, B. Du Bois, A. Dusa, S. Kerman, M. Mahmud-Ul-Hasan, P. Van Dorpe, X. Rottenberg, and L. Lagae, "Integrated metasurface photonics for miniature flow cytometry (conference presentation)," in *Nanoscale Imaging, Sensing, and Actuation for Biomedical Applications XV*, vol. 10506, p. 105060X, International Society for Optics and Photonics, 2018.

[45] G. Dubeau-Laramée, C. Riviere, I. Jean, O. Mermut, and L. Y. Cohen, "Microflow1, a sheathless fiber-optic flow cytometry biomedical platform: Demonstration onboard the international space station," *Cytometry Part A*, vol. 85, no. 4, pp. 322–331, 2014.

[46] V. K. Jagannadh, M. D. Mackenzie, P. Pal, A. K. Kar, and S. S. Gorthi, "Imaging flow cytometry with femtosecond laser-micromachined glass

microfluidic channels," *IEEE Journal of Selected Topics in Quantum Electronics*, vol. 21, no. 4, pp. 370–375, 2014.

[47] P. Paiè, F. Bragheri, R. M. Vazquez, and R. Osellame, "Straightforward 3d hydrodynamic focusing in femtosecond laser fabricated microfluidic channels," *Lab on a Chip*, vol. 14, no. 11, pp. 1826–1833, 2014.

[48] S. He, F. Chen, Q. Yang, K. Liu, C. Shan, H. Bian, H. Liu, X. Meng, J. Si, Y. Zhao, *et al.*, "Facile fabrication of true three-dimensional microcoils inside fused silica by a femtosecond laser," *Journal of Micromechanics and Microengineering*, vol. 22, no. 10, p. 105017, 2012.

[49] N. Bellini, K. Vishnubhatla, F. Bragheri, L. Ferrara, P. Minzioni, R. Ramponi, I. Cristiani, and R. Osellame, "Femtosecond laser fabricated monolithic chip for optical trapping and stretching of single cells," *Optics Express*, vol. 18, no. 5, pp. 4679–4688, 2010.

[50] T. Yang and Y. Bellouard, "Monolithic transparent 3d dielectrophoretic micro-actuator fabricated by femtosecond laser," *Journal of Micromechanics and Microengineering*, vol. 25, no. 10, p. 105009, 2015.

[51] C.-E. Athanasiou and Y. Bellouard, "A monolithic micro-tensile tester for investigating silicon dioxide polymorph micromechanics, fabricated and operated using a femtosecond laser," *Micromachines*, vol. 6, no. 9, pp. 1365–1386, 2015.

[52] D. J. Beebe, G. A. Mensing, and G. M. Walker, "Physics and applications of microfluidics in biology," *Annual review of biomedical engineering*, vol. 4, no. 1, pp. 261–286, 2002.

[53] T. G. Mezger, *The rheology handbook: for users of rotational and oscillatory rheometers*. Vincentz Network GmbH & Co KG, 2006.

[54] E. Litmanovich, G. Syaduk, E. Lysenko, A. Zezin, A. Kabanov, and V. Kabanov, "Effect of concentration regime on rheological properties of

sodium polymethacrylate and its complexes with polystyrene-poly (n-ethyl-4-vinylpyridinium bromide) block copolymer in aqueous salt solution," *Polymer Science Series A*, vol. 48, no. 9, pp. 997–1003, 2006.

[55] D. I. Verrelli and A. R. Kilcullen, "Normal stress differences and yield stresses in attractive particle networks," *Advances in Condensed Matter Physics*, vol. 2016, 2016.

[56] M. Rosenauer, W. Buchegger, I. Finoulst, P. Verhaert, and M. Vellekoop, "Miniaturized flow cytometer with 3d hydrodynamic particle focusing and integrated optical elements applying silicon photodiodes," *Microfluidics and Nanofluidics*, vol. 10, no. 4, pp. 761–771, 2011.

[57] A. Kummrow, J. Theisen, M. Frankowski, A. Tuchscheerer, H. Yildirim, K. Brattke, M. Schmidt, and J. Neukammer, "Microfluidic structures for flow cytometric analysis of hydrodynamically focussed blood cells fabricated by ultraprecision micromachining," *Lab on a Chip*, vol. 9, no. 7, pp. 972–981, 2009.

[58] M. J. Kennedy, S. J. Stelick, L. G. Sayam, A. Yen, D. Erickson, and C. A. Batt, "Hydrodynamic optical alignment for microflow cytometry," *Lab on a Chip*, vol. 11, no. 6, pp. 1138–1143, 2011.

[59] D. Holmes, H. Morgan, and N. G. Green, "High throughput particle analysis: Combining dielectrophoretic particle focussing with confocal optical detection," *Biosensors and Bioelectronics*, vol. 21, no. 8, pp. 1621–1630, 2006.

[60] S. Yan, J. Zhang, M. Li, G. Alici, H. Du, R. Sluyter, and W. Li, "On-chip high-throughput manipulation of particles in a dielectrophoresis-active hydrophoretic focuser," *Scientific reports*, vol. 4, p. 5060, 2014.

[61] L. Liang and X. Xuan, "Diamagnetic particle focusing using ferromicrofluidics with a single magnet," *Microfluidics and nanofluidics*, vol. 13, no. 4, pp. 637–643, 2012.

[62] J. Shi, X. Mao, D. Ahmed, A. Colletti, and T. J. Huang, "Focusing microparticles in a microfluidic channel with standing surface acoustic waves (ssaw)," *Lab on a Chip*, vol. 8, no. 2, pp. 221–223, 2008.

[63] J. Shi, S. Yazdi, S.-C. S. Lin, X. Ding, I.-K. Chiang, K. Sharp, and T. J. Huang, "Three-dimensional continuous particle focusing in a microfluidic channel via standing surface acoustic waves (ssaw)," *Lab on a Chip*, vol. 11, no. 14, pp. 2319–2324, 2011.

[64] Y. Chen, A. A. Nawaz, Y. Zhao, P.-H. Huang, J. P. McCoy, S. J. Levine, L. Wang, and T. J. Huang, "Standing surface acoustic wave (ssaw)-based microfluidic cytometer," *Lab on a Chip*, vol. 14, no. 5, pp. 916–923, 2014.

[65] H. Amini, W. Lee, and D. Di Carlo, "Inertial microfluidic physics," *Lab on a Chip*, vol. 14, no. 15, pp. 2739–2761, 2014.

[66] P. Saffman, "The lift on a small sphere in a slow shear flow," *Journal of fluid mechanics*, vol. 22, no. 2, pp. 385–400, 1965.

[67] S. I. Rubinow and J. B. Keller, "The transverse force on a spinning sphere moving in a viscous fluid," *Journal of Fluid Mechanics*, vol. 11, no. 3, pp. 447–459, 1961.

[68] B. Ho and L. Leal, "Migration of rigid spheres in a two-dimensional unidirectional shear flow of a second-order fluid," *Journal of Fluid Mechanics*, vol. 76, no. 4, pp. 783–799, 1976.

[69] W. Tang, D. Tang, Z. Ni, N. Xiang, and H. Yi, "Microfluidic impedance cytometer with inertial focusing and liquid electrodes for high-throughput cell counting and discrimination," *Analytical chemistry*, vol. 89, no. 5, pp. 3154–3161, 2017.

[70] S. C. Hur, H. T. K. Tse, and D. Di Carlo, "Sheathless inertial cell ordering for extreme throughput flow cytometry," *Lab on a Chip*, vol. 10, no. 3, pp. 274–280, 2010.

[71] S. Yang, J. Y. Kim, S. J. Lee, S. S. Lee, and J. M. Kim, "Sheathless elasto-inertial particle focusing and continuous separation in a straight rectangular microchannel," *Lab on a Chip*, vol. 11, no. 2, pp. 266–273, 2011.

[72] Y.-S. Choi, K.-W. Seo, and S.-J. Lee, "Lateral and cross-lateral focusing of spherical particles in a square microchannel," *Lab on a Chip*, vol. 11, no. 3, pp. 460–465, 2011.

[73] J.-P. Matas, J. F. Morris, and É. Guazzelli, "Inertial migration of rigid spherical particles in poiseuille flow," *Journal of Fluid Mechanics*, vol. 515, pp. 171–195, 2004.

[74] J.-A. Kim, J. Lee, C. Wu, S. Nam, D. Di Carlo, and W. Lee, "Inertial focusing in non-rectangular cross-section microchannels and manipulation of accessible focusing positions," *Lab on a Chip*, vol. 16, no. 6, pp. 992–1001, 2016.

[75] A. A. S. Bhagat, S. S. Kuntaegowdanahalli, N. Kaval, C. J. Seliskar, and I. Papautsky, "Inertial microfluidics for sheath-less high-throughput flow cytometry," *Biomedical microdevices*, vol. 12, no. 2, pp. 187–195, 2010.

[76] P. Paiè, F. Bragheri, D. Di Carlo, and R. Osellame, "Particle focusing by 3d inertial microfluidics," *Microsystems & Nanoengineering*, vol. 3, no. 1, pp. 1–8, 2017.

[77] X. Wang, H. Gao, N. Dindic, N. Kaval, and I. Papautsky, "A low-cost, plug-and-play inertial microfluidic helical capillary device for high-throughput flow cytometry," *Biomicrofluidics*, vol. 11, no. 1, p. 014107, 2017.

[78] M. Asghari, M. Serhatlioglu, R. Saritas, M. T. Guler, and C. Elbuken, "Tape'n roll inertial microfluidics," *Sensors and Actuators A: Physical*, vol. 299, p. 111630, 2019.

[79] G. Holzner, S. Stavrakis, and A. DeMello, "Elasto-inertial focusing of mammalian cells and bacteria using low molecular, low viscosity peo solutions,"

Analytical chemistry, vol. 89, no. 21, pp. 11653–11663, 2017.

[80] X. Lu, C. Liu, G. Hu, and X. Xuan, "Particle manipulations in non-newtonian microfluidics: A review," *Journal of colloid and interface science*, vol. 500, pp. 182–201, 2017.

[81] D. Yuan, Q. Zhao, S. Yan, S.-Y. Tang, G. Alici, J. Zhang, and W. Li, "Recent progress of particle migration in viscoelastic fluids," *Lab on a Chip*, vol. 18, no. 4, pp. 551–567, 2018.

[82] G. D'Avino, G. Romeo, M. M. Villone, F. Greco, P. A. Netti, and P. L. Maffettone, "Single line particle focusing induced by viscoelasticity of the suspending liquid: theory, experiments and simulations to design a micropipe flow-focuser," *Lab on a Chip*, vol. 12, no. 9, pp. 1638–1645, 2012.

[83] D. Li, X. Lu, and X. Xuan, "Viscoelastic separation of particles by size in straight rectangular microchannels: a parametric study for a refined understanding," *Analytical chemistry*, vol. 88, no. 24, pp. 12303–12309, 2016.

[84] N. Xiang, X. Zhang, Q. Dai, J. Cheng, K. Chen, and Z. Ni, "Fundamentals of elasto-inertial particle focusing in curved microfluidic channels," *Lab on a Chip*, vol. 16, no. 14, pp. 2626–2635, 2016.

[85] B. Steinhaus, A. Q. Shen, and R. Sureshkumar, "Dynamics of viscoelastic fluid filaments in microfluidic devices," *Physics of Fluids*, vol. 19, no. 7, p. 073103, 2007.

[86] G. Li, G. H. McKinley, and A. M. Ardekani, "Dynamics of particle migration in channel flow of viscoelastic fluids," *Journal of Fluid Mechanics*, vol. 785, pp. 486–505, 2015.

[87] S. H. Yang, D. J. Lee, J. R. Youn, and Y. S. Song, "Multiple-line particle focusing under viscoelastic flow in a microfluidic device," *Analytical chemistry*, vol. 89, no. 6, pp. 3639–3647, 2017.

[88] E. J. Lim, T. J. Ober, J. F. Edd, S. P. Desai, D. Neal, K. W. Bong, P. S. Doyle, G. H. McKinley, and M. Toner, "Inertio-elastic focusing of bioparticles in microchannels at high throughput," *Nature communications*, vol. 5, no. 1, pp. 1–9, 2014.

[89] S. W. Ahn, S. S. Lee, S. J. Lee, and J. M. Kim, "Microfluidic particle separator utilizing sheathless elasto-inertial focusing," *Chemical Engineering Science*, vol. 126, pp. 237–243, 2015.

[90] X. Lu and X. Xuan, "Continuous microfluidic particle separation via elasto-inertial pinched flow fractionation," *Analytical chemistry*, vol. 87, no. 12, pp. 6389–6396, 2015.

[91] N. Xiang, Z. Ni, and H. Yi, "Concentration-controlled particle focusing in spiral elasto-inertial microfluidic devices," *Electrophoresis*, vol. 39, no. 2, pp. 417–424, 2018.

[92] K. Won Seo, Y. Ran Ha, and S. Joon Lee, "Vertical focusing and cell ordering in a microchannel via viscoelasticity: Applications for cell monitoring using a digital holographic microscopy," *Applied Physics Letters*, vol. 104, no. 21, p. 213702, 2014.

[93] J. Nam, H. Lim, D. Kim, H. Jung, and S. Shin, "Continuous separation of microparticles in a microfluidic channel via the elasto-inertial effect of non-newtonian fluid," *Lab on a Chip*, vol. 12, no. 7, pp. 1347–1354, 2012.

[94] S. Yang, S. S. Lee, S. W. Ahn, K. Kang, W. Shim, G. Lee, K. Hyun, and J. M. Kim, "Deformability-selective particle entrainment and separation in a rectangular microchannel using medium viscoelasticity," *Soft Matter*, vol. 8, no. 18, pp. 5011–5019, 2012.

[95] C. Liu, B. Ding, C. Xue, Y. Tian, G. Hu, and J. Sun, "Sheathless focusing and separation of diverse nanoparticles in viscoelastic solutions with minimized shear thinning," *Analytical chemistry*, vol. 88, no. 24, pp. 12547–12553, 2016.

[96] T. Go, H. Byeon, and S. J. Lee, "Focusing and alignment of erythrocytes in a viscoelastic medium," *Scientific reports*, vol. 7, no. 1, pp. 1–10, 2017.

[97] C. Liu, C. Xue, and G. Hu, "Sheathless separation of particles and cells by viscoelastic effects in straight rectangular microchannels," *Procedia Engineering*, vol. 126, pp. 721–724, 2015.

[98] C.-k. Tung, C. Lin, B. Harvey, A. G. Fiore, F. Ardon, M. Wu, and S. S. Suarez, "Fluid viscoelasticity promotes collective swimming of sperm," *Scientific reports*, vol. 7, no. 1, pp. 1–9, 2017.

[99] F. Del Giudice, S. Sathish, G. D'Avino, and A. Q. Shen, ""from the edge to the center": viscoelastic migration of particles and cells in a strongly shear-thinning liquid flowing in a microchannel," *Analytical chemistry*, vol. 89, no. 24, pp. 13146–13159, 2017.

[100] M. A. Faridi, H. Ramachandraiah, I. Banerjee, S. Ardabili, S. Zelenin, and A. Russom, "Elasto-inertial microfluidics for bacteria separation from whole blood for sepsis diagnostics," *Journal of nanobiotechnology*, vol. 15, no. 1, p. 3, 2017.

[101] J. S. Kim, G. P. Anderson, J. S. Erickson, J. P. Golden, M. Nasir, and F. S. Ligler, "Multiplexed detection of bacteria and toxins using a microflow cytometer," *Analytical chemistry*, vol. 81, no. 13, pp. 5426–5432, 2009.

[102] M. Asghari, M. Serhatlioglu, B. Ortaç, M. E. Solmaz, and C. Elbuken, "Sheathless microflow cytometry using viscoelastic fluids," *Scientific reports*, vol. 7, no. 1, pp. 1–14, 2017.

[103] M. J. Fulwyler, "Electronic separation of biological cells by volume," *Science*, vol. 150, no. 3698, pp. 910–911, 1965.

[104] J. Guo, X. Ma, N. V. Menon, C. M. Li, Y. Zhao, and Y. Kang, "Dual fluorescence-activated study of tumor cell apoptosis by an optofluidic system," *IEEE Journal of Selected Topics in Quantum Electronics*, vol. 21,

no. 4, pp. 392–398, 2014.

[105] X. Mao, S.-C. S. Lin, C. Dong, and T. J. Huang, "Single-layer planar on-chip flow cytometer using microfluidic drifting based three-dimensional (3d) hydrodynamic focusing," *Lab on a Chip*, vol. 9, no. 11, pp. 1583–1589, 2009.

[106] D. Huh, W. Gu, Y. Kamotani, J. B. Grotberg, and S. Takayama, "Microfluidics for flow cytometric analysis of cells and particles," *Physiological measurement*, vol. 26, no. 3, p. R73, 2005.

[107] G.-B. Lee, C.-H. Lin, and G.-L. Chang, "Micro flow cytometers with buried su-8/sog optical waveguides," *Sensors and Actuators A: Physical*, vol. 103, no. 1-2, pp. 165–170, 2003.

[108] M. Kim, D. J. Hwang, H. Jeon, K. Hiromatsu, and C. P. Grigoropoulos, "Single cell detection using a glass-based optofluidic device fabricated by femtosecond laser pulses," *Lab on a Chip*, vol. 9, no. 2, pp. 311–318, 2009.

[109] J. Godin, V. Lien, and Y.-H. Lo, "Demonstration of two-dimensional fluidic lens for integration into microfluidic flow cytometers," *Applied Physics Letters*, vol. 89, no. 6, p. 061106, 2006.

[110] Y. Zhao, Q. Li, X. Hu, and Y. Lo, "Microfluidic cytometers with integrated on-chip optical systems for red blood cell and platelet counting," *Biomicrofluidics*, vol. 10, no. 6, p. 064119, 2016.

[111] B. R. Watts, Z. Zhang, C. Q. Xu, X. Cao, and M. Lin, "A photonic-microfluidic integrated device for reliable fluorescence detection and counting," *Electrophoresis*, vol. 33, no. 21, pp. 3236–3244, 2012.

[112] S.-K. Hsiung, S.-R. Lin, and C.-H. Lin, "Micro flow cytometry chip device integrated with tunable microlens for circulating tumor cells detection and counting applications," *Japanese Journal of Applied Physics*, vol. 49, no. 6R, p. 060218, 2010.

[113] X. Mao, J. R. Waldeisen, B. K. Juluri, and T. J. Huang, "Hydrodynamically tunable optofluidic cylindrical microlens," *Lab on a Chip*, vol. 7, no. 10, pp. 1303–1308, 2007.

[114] M. Tehrani, "An experimental study of particle migration in pipe flow of viscoelastic fluids," *Journal of Rheology*, vol. 40, no. 6, pp. 1057–1077, 1996.

[115] K. Kang, S. S. Lee, K. Hyun, S. J. Lee, and J. M. Kim, "Dna-based highly tunable particle focuser," *Nature communications*, vol. 4, p. 2567, 2013.

[116] V. Can and O. Okay, "Shake gels based on laponite–peo mixtures: effect of polymer molecular weight," *Designed monomers and polymers*, vol. 8, no. 5, pp. 453–462, 2005.

[117] R. Mendichi, L. Šoltés, and A. Giacometti Schieroni, "Evaluation of radius of gyration and intrinsic viscosity molar mass dependence and stiffness of hyaluronan," *Biomacromolecules*, vol. 4, no. 6, pp. 1805–1810, 2003.

[118] J. Claverie, C. Pichot, *et al.*, *Polymers in Dispersed Media I: International Conference on Polymers in Dispersed Media*, vol. 1. John Wiley & Sons, 2000.

[119] W. W. Graessley, "Polymer chain dimensions and the dependence of viscoelastic properties on concentration, molecular weight and solvent power," *Polymer*, vol. 21, no. 3, pp. 258–262, 1980.

[120] V. Tirtaatmadja, G. MecKinley, and J. Cooper, "White, drop formation and breakup of low viscosity elastic fluids: effects of molecular weight and concentration. hml report, department of mechanical engineering," 2006.

[121] S. Shimabayashi, T. Sannoh, and M. Nakagaki, "Decrease in intrinsic viscosity of polyvinylpyrrolidone in the presence of sodium chondroitin sulfate or sodium carboxymethylcellulose in an aqueous solution," *Chemical and pharmaceutical bulletin*, vol. 37, no. 10, pp. 2811–2813, 1989.

[122] R. A. Erickson and R. Jimenez, "Microfluidic cytometer for high-throughput measurement of photosynthetic characteristics and lipid accumulation in individual algal cells," *Lab on a Chip*, vol. 13, no. 15, pp. 2893–2901, 2013.

[123] Z. Cheng, X. Wu, J. Cheng, and P. Liu, "Microfluidic fluorescence-activated cell sorting (μfacs) chip with integrated piezoelectric actuators for low-cost mammalian cell enrichment," *Microfluidics and Nanofluidics*, vol. 21, no. 1, p. 9, 2017.

[124] G. Testa, G. Persichetti, and R. Bernini, "Micro flow cytometer with self-aligned 3d hydrodynamic focusing," *Biomedical optics express*, vol. 6, no. 1, pp. 54–62, 2015.

[125] C. Simonnet and A. Groisman, "High-throughput and high-resolution flow cytometry in molded microfluidic devices," *Analytical chemistry*, vol. 78, no. 16, pp. 5653–5663, 2006.

[126] H. Bang, H. Yun, W. G. Lee, J. Park, J. Lee, S. Chung, K. Cho, C. Chung, D.-C. Han, and J. K. Chang, "Expansion channel for microchip flow cytometers," *Lab on a Chip*, vol. 6, no. 10, pp. 1381–1383, 2006.

[127] G. Goddard, J. C. Martin, S. W. Graves, and G. Kaduchak, "Ultrasonic particle-concentration for sheathless focusing of particles for analysis in a flow cytometer," *Cytometry Part A: The Journal of the International Society for Analytical Cytology*, vol. 69, no. 2, pp. 66–74, 2006.

[128] J. Oakey, R. W. Applegate Jr, E. Arellano, D. D. Carlo, S. W. Graves, and M. Toner, "Particle focusing in staged inertial microfluidic devices for flow cytometry," *Analytical chemistry*, vol. 82, no. 9, pp. 3862–3867, 2010.

[129] M. T. Guler and I. Bilican, "Capacitive detection of single bacterium from drinking water with a detailed investigation of electrical flow cytometry," *Sensors and Actuators A: Physical*, vol. 269, pp. 454–463, 2018.

[130] M. T. Guler, I. Bilican, S. Agan, and C. Elbuken, "A simple approach for the fabrication of 3d microelectrodes for impedimetric sensing," *Journal of Micromechanics and Microengineering*, vol. 25, no. 9, p. 095019, 2015.

[131] S. Etcheverry, A. Faridi, H. Ramachandraiah, T. Kumar, W. Margulis, F. Laurell, and A. Russom, "High performance micro-flow cytometer based on optical fibres," *Scientific reports*, vol. 7, no. 1, pp. 1–8, 2017.

[132] J. Nam, B. Namgung, C. T. Lim, J.-E. Bae, H. L. Leo, K. S. Cho, and S. Kim, "Microfluidic device for sheathless particle focusing and separation using a viscoelastic fluid," *Journal of Chromatography A*, vol. 1406, pp. 244–250, 2015.

[133] D. Li and X. Xuan, "Fluid rheological effects on particle migration in a straight rectangular microchannel," *Microfluidics and Nanofluidics*, vol. 22, no. 4, p. 49, 2018.

[134] M. Y. Danny, G. L. Amidon, N. D. Weiner, and A. H. Goldberg, "Viscoelastic properties of poly (ethylene oxide) solution," *Journal of pharmaceutical sciences*, vol. 83, no. 10, pp. 1443–1449, 1994.

[135] M. Serhatlioglu, Z. Isiksacan, M. Özkan, D. Tuncel, and C. Elbuken, "Electro-viscoelastic migration under simultaneously applied microfluidic pressure-driven flow and electric field," *Analytical Chemistry*, 2020.

[136] J. Y. Kim, S. W. Ahn, S. S. Lee, and J. M. Kim, "Lateral migration and focusing of colloidal particles and dna molecules under viscoelastic flow," *Lab on a Chip*, vol. 12, no. 16, pp. 2807–2814, 2012.

[137] M. Asghari, X. Cao, B. Mateescu, D. Van Leeuwen, M. K. Aslan, S. Stavrakis, and A. J. deMello, "Oscillatory viscoelastic microfluidics for efficient focusing and separation of nanoscale species," *ACS nano*, 2019.

[138] X. Lu and X. Xuan, "Elasto-inertial pinched flow fractionation for continuous shape-based particle separation," *Analytical chemistry*, vol. 87, no. 22,

pp. 11523–11530, 2015.

[139] C. Liu, C. Xue, X. Chen, L. Shan, Y. Tian, and G. Hu, "Size-based separation of particles and cells utilizing viscoelastic effects in straight microchannels," *Analytical chemistry*, vol. 87, no. 12, pp. 6041–6048, 2015.

[140] J. Zheng and E. S. Yeung, "Anomalous radial migration of single dna molecules in capillary electrophoresis," *Analytical chemistry*, vol. 74, no. 17, pp. 4536–4547, 2002.

[141] M. Arca, J. E. Butler, and A. J. Ladd, "Transverse migration of polyelectrolytes in microfluidic channels induced by combined shear and electric fields," *Soft Matter*, vol. 11, no. 22, pp. 4375–4382, 2015.

[142] M. Arca, A. J. Ladd, and J. E. Butler, "Electro-hydrodynamic concentration of genomic length dna," *Soft matter*, vol. 12, no. 33, pp. 6975–6984, 2016.

[143] R. Kekre, J. E. Butler, and A. J. Ladd, "Role of hydrodynamic interactions in the migration of polyelectrolytes driven by a pressure gradient and an electric field," *Physical Review E*, vol. 82, no. 5, p. 050803, 2010.

[144] R. J. Montes, J. E. Butler, and A. J. Ladd, "Trapping dna with a high throughput microfluidic device," *Electrophoresis*, vol. 40, no. 3, pp. 437–446, 2019.

[145] Y. W. Kim and J. Y. Yoo, "Axisymmetric flow focusing of particles in a single microchannel," *Lab on a Chip*, vol. 9, no. 8, pp. 1043–1045, 2009.

[146] Y. W. Kim and J. Y. Yoo, "Bidirectional inward migration of particles lagging behind a poiseuille flow in a rectangular microchannel for 3d particle focusing," *Journal of Micromechanics and Microengineering*, vol. 25, no. 2, p. 027002, 2015.

[147] D. Li and X. Xuan, "Electrophoretic slip-tuned particle migration in microchannel viscoelastic fluid flows," *Physical Review Fluids*, vol. 3, no. 7, p. 074202, 2018.

[148] N. Cevheri and M. Yoda, "Lift forces on colloidal particles in combined electroosmotic and poiseuille flow," *Langmuir*, vol. 30, no. 46, pp. 13771–13780, 2014.

[149] N. Cevheri and M. Yoda, "Electrokinetically driven reversible banding of colloidal particles near the wall," *Lab on a Chip*, vol. 14, no. 8, pp. 1391–1394, 2014.

[150] H. Ranchon, R. Malbec, V. Picot, A. Boutonnet, P. Terrapanich, P. Joseph, T. Leichle, and A. Bancaud, "Dna separation and enrichment using electrohydrodynamic bidirectional flows in viscoelastic liquids," *Lab on a Chip*, vol. 16, no. 7, pp. 1243–1253, 2016.

[151] C.-L. Andriamanampisoa, A. Bancaud, A. Boutonnet-Rodat, A. Didelot, J. Fabre, F. Fina, F. Garlan, S. Garrigou, C. Gaudy, F. Ginot, *et al.*, "Biabooster: online dna concentration and size profiling with a limit of detection of 10 fg/μl and application to high-sensitivity characterization of circulating cell-free dna," *Analytical chemistry*, vol. 90, no. 6, pp. 3766–3774, 2018.

[152] A. Choudhary, D. Li, T. Renganathan, X. Xuan, and S. Pushpavanam, "Electrokinetics enhances cross-stream particle migration in viscoelastic flows," *arXiv preprint arXiv:1907.03701*, 2019.

[153] S. Dubrovskii, A. Zelenetskii, S. Uspenskii, and V. Khabarov, "Effect of borax additives on the rheological properties of sodium hyaluronate aqueous solutions," *Polymer Science Series A*, vol. 56, no. 2, pp. 205–210, 2014.

[154] A. V. Dobrynin, M. Rubinstein, and S. P. Obukhov, "Cascade of transitions of polyelectrolytes in poor solvents," *Macromolecules*, vol. 29, no. 8, pp. 2974–2979, 1996.

[155] M. K. Cowman, T. A. Schmidt, P. Raghavan, and A. Stecco, "Viscoelastic properties of hyaluronan in physiological conditions," *F1000Research*, vol. 4, 2015.

[156] F. Del Giudice, G. Romeo, G. D'Avino, F. Greco, P. A. Netti, and P. L. Maffettone, "Particle alignment in a viscoelastic liquid flowing in a square-shaped microchannel," *Lab on a Chip*, vol. 13, no. 21, pp. 4263–4271, 2013.

[157] K. Shirahama, A. Himuro, and N. Takisawa, "Binding of hexadecylammonium surfactants to water-soluble neutral polymers," *Colloid and Polymer Science*, vol. 265, no. 2, pp. 96–100, 1987.

[158] J. M. Martel and M. Toner, "Inertial focusing in microfluidics," *Annual review of biomedical engineering*, vol. 16, pp. 371–396, 2014.

[159] F. J. Galindo-Rosales, L. Campo-Deaño, P. C. Sousa, V. M. Ribeiro, M. S. Oliveira, M. A. Alves, and F. T. Pinho, "Viscoelastic instabilities in micro-scale flows," *Experimental Thermal and Fluid Science*, vol. 59, pp. 128–139, 2014.

[160] M. T. Glynn, D. J. Kinahan, and J. Ducrée, "Cd4 counting technologies for hiv therapy monitoring in resource-poor settings–state-of-the-art and emerging microtechnologies," *Lab on a Chip*, vol. 13, no. 14, pp. 2731–2748, 2013.

[161] B. T. Grimberg, "Methodology and application of flow cytometry for investigation of human malaria parasites," *Journal of immunological methods*, vol. 367, no. 1-2, pp. 1–16, 2011.

[162] O. D. Laerum and T. Farsund, "Clinical application of flow cytometry: a review," *Cytometry: The Journal of the International Society for Analytical Cytology*, vol. 2, no. 1, pp. 1–13, 1981.

[163] A. Álvarez-Barrientos, J. Arroyo, R. Cantón, C. Nombela, and M. Sánchez-Pérez, "Applications of flow cytometry to clinical microbiology," *Clinical*

microbiology reviews, vol. 13, no. 2, pp. 167–195, 2000.

[164] M. Rieseberg, C. Kasper, K. F. Reardon, and T. Scheper, "Flow cytometry in biotechnology," *Applied microbiology and biotechnology*, vol. 56, no. 3-4, pp. 350–360, 2001.

[165] J. Lebedová, Y. S. Hedberg, I. Odnevall Wallinder, and H. L. Karlsson, "Size-dependent genotoxicity of silver, gold and platinum nanoparticles studied using the mini-gel comet assay and micronucleus scoring with flow cytometry," *Mutagenesis*, vol. 33, no. 1, pp. 77–85, 2018.

[166] D. A. Watson, D. F. Gaskill, L. O. Brown, S. K. Doorn, and J. P. Nolan, "Spectral measurements of large particles by flow cytometry," *Cytometry Part A: The Journal of the International Society for Advancement of Cytometry*, vol. 75, no. 5, pp. 460–464, 2009.

[167] I. Heidmann, G. Schade-Kampmann, J. Lambalk, M. Ottiger, and M. Di Berardino, "Impedance flow cytometry: a novel technique in pollen analysis," *PloS one*, vol. 11, no. 11, 2016.

Appendix A

Publication List

All license agreements between Murat Serhatlioglu and the License Suppliers are made by means of Copyright Clearance Center.

1. M. Serhatlioglu, Z. Isiksacan, M. Ozkan, D. Tuncel, and C. Elbuken, Electro-viscoelastic migration under simultaneously applied microfluidic pressure-driven flow and electric field, Analytical Chemistry, 2020.

2. I. Bilican, M. T. Guler, M. Serhatlioglu, T. Kirindi, and C. Elbuken, Focusing-free impedimetric differentiation of red blood cells and leukemia cells: A system optimization, Sensors and Actuators B: Chemical, p. 127531. 2020.

3. M. Asghari, M. Serhatlioglu, R. Saritas, M. T. Guler, and C. Elbuken, Tape'n roll inertial microfluidics, Sensors and Actuators A: Physical, vol. 299, p. 111630, 2019.

4. G. Bakan, S. Ayas, M. Serhatlioglu, A. Dana, and C. Elbuken, Reversible decryption of covert nanometer-thick patterns in modular metamaterials, Optics letters, vol. 44, no. 18, p. 4507-4510, 2019.

5. M. Serhatlioglu, M. Asghari, M. T. Guler, and C. Elbuken, Impedance-based viscoelastic flow cytometry, Electrophoresis, vol. 40, no. 6, p. 906-913, 2019.

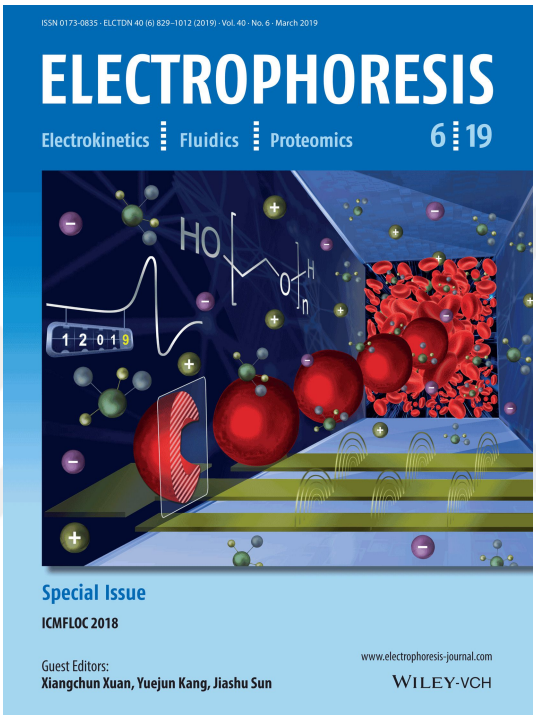


Figure A.1: Electrophoresis front cover [7]

6. S. O. Karabel, S. Pekdemir, M. Serhatlioglu, H. H. Ipekci, E. Sahmetlioglu, I. Narin, F. Duman, C. Elbuken, G. Demirel, and M. S. Onses, Eco-friendly fabrication of plasmonically active substrates based on end-grafted poly (ethylene glycol) layers, ACS Sustainable Chemistry and Engineering, vol. 7, no. 4, p. 4315-4324, 2019.

7. A. Saateh, A. Kalantarifard, O. T. Celik, M. Asghari, M. Serhatlioglu, and Caglar Elbuken, Real-time impedimetric droplet measurement (iDM), Lab on a Chip, vol. 19, no. 22, p. 3815-3824, 2019.

8. M. T. Guler, Z. Isiksacan, M. Serhatlioglu, and C. Elbuken, Self-powered disposable prothrombin time measurement device with an integrated effervescent pump, Sensors and Actuators B: Chemical, vol. 273, p. 350-357, 2018.

9. G. Bakan, S. Ayas, M. Serhatlioglu, C. Elbuken, and A. Dana, Invisible Thin-Film Patterns with Strong Infrared Emission as an Optical Security Feature, Advanced Optical Materials, vol. 6, no. 21, p. 1800613, 2018.

10. A. Bayram, M. Serhatlioglu, B. Ortac, Se. Demic, C. Elbuken, M. Sen, and M. E. Solmaz, Integration of glass micropipettes with a 3D printed aligner for microfluidic flow cytometer, Sensors and Actuators A: Physical, vol. 269 p. 382-387, 2018.

11. M. Asghari, M. Serhatlioglu, B. Ortac, M. E. Solmaz, and C. Elbuken, Sheathless microflow cytometry using viscoelastic fluids, Scientific reports, vol. 7, no. 1, p. 1-14, 2017.

12. M. Serhatlioglu, C. Elbuken, B. Ortac, and M. E. Solmaz, Femtosecond laser fabrication of fiber based optofluidic platform for flow cytometry applications, In Optical Fibers and Sensors for Medical Diagnostics and Treatment Applications XVII, vol. 10058, p. 100580I, 2017.

13. M. Serhatlioglu, B. Ortac, C. Elbuken, N. Biyikli, and M. E. Solmaz, CO2 laser polishing of microfluidic channels fabricated by femtosecond laser assisted carving, Journal of Micromechanics and Microengineering, vol. 26, no. 11 p. 115011, 2016.

14. M. Serhatlioglu, S. Ayas, N. Biyikli, A. Dana, and M. E. Solmaz, Perfectly absorbing ultra thin interference coatings for hydrogen sensing, Optics letters, vol. 41, no. 8, p. 1724-1727, 2016.

15. M. E. Solmaz, B. Cetin, B. Baranoglu, M. Serhatlioglu, and Necmi Biyikli, Boundary element method for optical force calibration in microfluidic dual-beam optical trap, In Optical Trapping and Optical Micromanipulation XII, vol. 9548, p. 95481D, 2015.

16. Z. Isiksacan, M. Serhatlioglu, and C. Elbuken, Hemorheometry-on-a-chip: Simultaneous analysis of blood biophysical properties using erythrocyte dynamics *(submitted)*